KNOWLEDGE DISCOVERY OF NANOTUBE MECHANICAL PROPERTIES WITH AN INFORMATICS-MOLECULAR DYNAMICS APPROACH

Tammie L. Borders

Dissertation Prepared for the Degree of

DOCTOR OF PHILOSOPHY

UNIVERSITY OF NORTH TEXAS

May 2012

APPROVED:

Martin Schwartz, Major Professor
Andrew Rusinko, Co-Advisor and Committee Member
Angela K. Wilson, Committee Member
Thomas R. Cundari, Committee Member
Srinivasan Srivilliputhur, Committee Member
William E. Acree, Jr, Chair of the Department of Chemistry
James D. Meernik, Acting Dean of the Toulouse Graduate School

Borders, Tammie L. Knowledge Discovery of Nanotube Mechanical Properties with an Informatics-Molecular Dynamics Approach. Doctor of Philosophy (Chemistry-Physical Chemistry), May 2012, 164 pp., 42 tables, 36 illustrations, references, 243 titles.

Carbon nanotubes (CNT) have unparalleled mechanical properties, spanning several orders of magnitude over both length and time scales. Computational and experimental results vary greatly, partly due to the multitude of variables. Coupling physics-based molecular dynamics (MD) with informatics methodologies is proposed to navigate the large problem space. The adaptive intermolecular reactive empirical bond order (AIREBO) is used to model short range, long range and torsional interactions. A powerful approach that has not been used to study CNT mechanical properties is the derivation of descriptors and quantitative structure property relationships (QSPRs). For the study of defected single-walled CNTs (SWCNT), two descriptors were identified as critical: the density of non-sp^2 hybridized carbons and the density of methyl groups functionalizing the surface. It is believed that both of these descriptors can be experimentally measured, paving the way for closed-loop computational-experimental development. Informatics can facilitate discovery of hidden knowledge. Further evaluation of the critical descriptors selected for Poisson's ratio lead to the discovery that Poisson's ratio has strain-varying nonlinear elastic behavior. CNT effectiveness in composites is based both on intrinsic mechanical properties and interfacial load transfer. In double-walled CNTs, inter-wall bonds are surface defects that decrease the intrinsic properties but also improve load transfer. QSPRs can be used to model these inverse effects and pinpoint the optimal amount of inter-wall bonds.

ACKNOWLEDGEMENTS

This dissertation would not have been possible without the support and encouragement from a number of my friends and family. First, I would like to thank Dr. Andrew Rusinko for agreeing to be my unofficial advisor. He selflessly volunteered hours upon hours of his time sharing knowledge gleaned through an outstanding industrial career. Second, I would like to thank Dr. KJ Cho, Hengji Zhang and Dr. Alexandre Fonseca through collaborations at the University of Texas – Dallas. They always made time for me, treating me as a direct member of their group and we shared many exciting discoveries together. Third, I would like to thank Dr. Martin Schwartz, my official advisor. He gave me the latitude, trust and encouragement to explore exactly what I wanted to explore. My co-workers at Lockheed Martin provided invaluable support and guidance, especially Dr. Rick Barto, Jason Poleski, Dr. Mike DiMario, Barry Ives and Dr. Michael Krein (Rensselaer). I would like to voice my sincerest appreciate to Dr. Michael Libertazzo, Myriam Qureshi, Lester Brooks and Susan Brockington, who always encouraged me and helped me see that things are not that hard. I would like to thank all of my family and friends – small words of encouragement go a long way. Specifically, I want to thank my wife Anna Paulson. Her love, support and shared excitement for the magic of science is intoxicating and I look forward to lifetime of new discoveries.

TABLE OF CONTENTS

LIST OF TABLES

LIST OF ILLUSTRATIONS

CHAPTER 1

INTRODUCTION

It is exciting to speculate the impact of a material system that is estimated to be 30-70 times stronger and approximately 5 times stiffer than carbon fiber at comparable or less density.[1] Carbon nanotubes (CNT) have a plethora of largely unparalleled mechanical, electrical, optical and thermal properties compared to most known materials.[2] In the aerospace industry, CNT reinforced composites could present large weight savings for an airframe, enabling ultra-light unmanned aerial vehicles (UAV) for long-loiter missions. High use temperatures and thermal conductivity on par with diamond adds capability for thermal management.[3] However, nano-materials are immensely complex with properties spanning several orders of magnitude over both length and time scales.[4] Further, the materials development process is not integrated into the product design engineering lifecycle, leading to 20 years or longer from the time a new material is conceived to the time it is used in components.[5] A new approach put forth in by the National Research Council (NRC) titled integrated computational materials engineering (ICME), has a goal of "integrating materials information, captured in computational tools, with engineering product performance analysis and manufacturing-process simulation."[4] Materials informatics is believed to be instrumental in bringing ICME to fruition. Materials informatics is the extraction of knowledge from information via the design, representation and organization of data sets and the application of data mining and analysis tools to reveal new physical relationships between the chemistry, structure and materials properties. It is not limited to materials development but can be applied to all aspects of this integrated process as the "hub."[6]

Informatics is not new; cheminformatics is a well-established discipline in the drug design process in the pharmaceutical industry. Bioinformatics research, the application of informatics to molecular biology, has exploded since the mid-1990s.[7] The application of informatics methodologies to materials is still in its infancy, with the first reference to the field being a conference in 1999.[8]

The objective of this research is to combine physics and informatics-based methodologies in the treatment of CNTs to facilitate a more thorough and accurate understanding of the structure-property relationships. Within the introduction, two topics will be addressed.

- Technology challenges and needs for materials development
- Discussion of CNT and CNT-reinforced materials

1.1 Materials Development Needs and Technical Challenges

With many technologies, materials development is the long straw in furthering significant improvements.[9] Two critical issues have been identified: 1) materials engineering tools development has lagged behind development in other fields and 2) materials engineering is not integrated into the product design process.[4] The ICME report states that the reasons for the lag are due to "the complexity and sheer variety of materials and physical phenomena that must be captured" and lack of user-friendly modeling and simulation programs. In the commercial and military markets, technology development and adoption continues to accelerate, exacerbating the need for both improved materials engineering tools and integration into the product design lifecycle.

1.1.1 Technical Challenges

Materials science is an interdisciplinary subject with four major focuses: 1) manufacturing and characterization processes, 2) structure, 3) properties and 4) application-specific performance.[10] Structure is the internal arrangement of its subcomponents and could be the organization of electrons, atoms, molecules, agglomerates of molecules or structural elements (e.g., beams) depending upon the scale of interest. Materials properties fall into five categories: mechanical, electrical, thermal, magnetic and optical. Mechanical properties are the elastic or inelastic response to an applied force (load). Axial tension and torsion are examples of loads. Moduli, strength and hardness are types of mechanical properties. Computational materials research has largely been directed toward developing structure-property relationships.[4, 11] ICME seeks to bridge all four areas of materials science by enabling concurrent analysis and design of materials manufacturing processes, material structure-property relationships and component performance.[12] DARPA's accelerated insertion of materials (AIM) program applied this approach to process, microstructure-property and uncertainty models for nickel-based alloy engine disks and reduced the materials development cycle by 50%.[9, 13] Designing for cost will be integral to affordable products, adding an S for 'systems' in ICMSE. Today's design engineer works independently of the cost engineer, unknowingly putting forth costly options (e.g., multi-rolled complex surface versus single-rolled surface) because the design engineer's only goal is to meet the performance requirements. ICME /ICMSE is critical to reduce cost and time to market while meeting or exceeding performance requirements.[9] Early studies comparing single-walled to multi-walled CNT reinforced

composites concluded single-walled CNT composites were optimal because stiffness and strength of single-walled pristine CNTs (SWCNTs) are superior to multi-walled CNTs (MWCNTs).[14] However, by including load transfer performance (linking structure, properties and performance), it was shown that chemical vapor deposition (CVD) grown MWCNTs improve load transfer in composites, outperforming defect-free single or multi-walled CNTs of similar length and diameter.[15]

To achieve ICME, many technical barriers must be overcome. These include 1) improved, user-friendly physics-based simulation tools, 2) rapid experimentation and 3D characterization, 3) integration tools, and 4) databases and informatics analysis tools.[4] Materials research questions cover a broad scope of issues and properties are controlled by disparate and frequently competing mechanisms. A diverse computational tool set is requisite to successfully explore material system properties and performance. Veedu explored the properties of CNT-reinforced fiber composites finding 348% improvement in fracture toughness and 240% improvement in flexural strength compared to the fiber only reinforced composite.[16] A potential problem space for this system is shown in Figure 1-1, spanning atomic to continuum length scales. CNT growth and interphase formation mechanisms (region of altered polymer properties in vicinity of CNT) need to be fully understood.[17] Uncertainties and biases at each scale must be quantified and propagated.

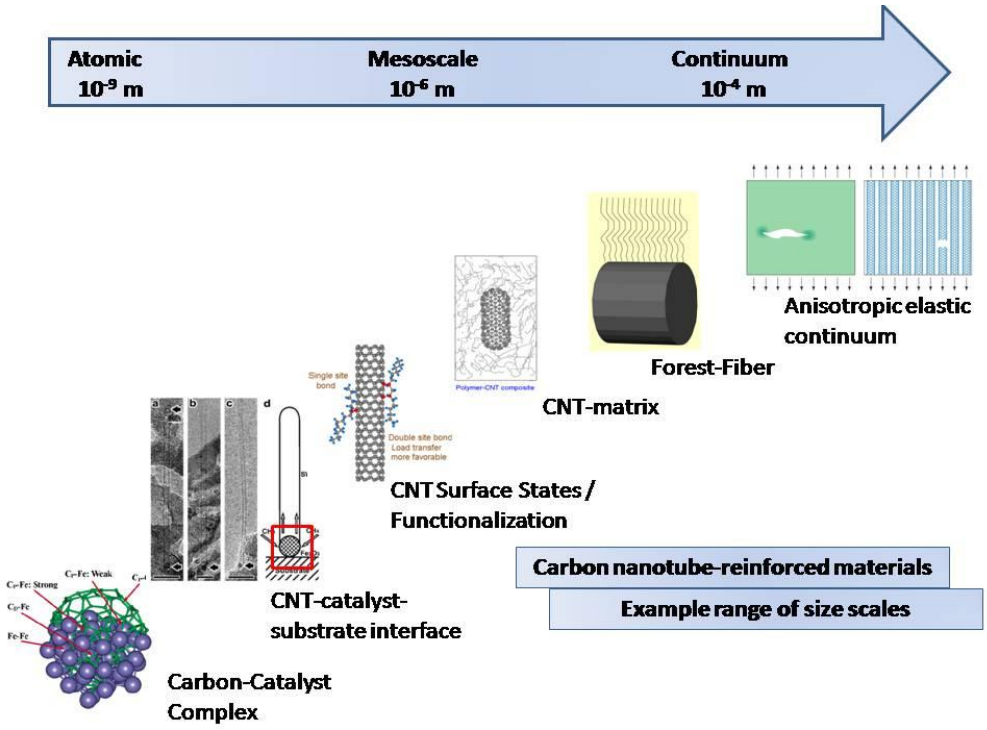

Figure 1-1: Interfaces and size scales for CNT-reinforced fiber composite span many orders of magnitudes.

At the atomic end, methods include electronic structure and molecular mechanics / dynamics (MM/MD). Within MM/MD, both classical and reactive potentials are utilized. Reactive potentials permit bond breaking and formation during the simulation.[18] Specialized knowledge and the ability to modify the tools are required. Investigating CNT tensile strength with the adaptive intermolecular reactive empirical bond order (AIREBO) requires a source code modification to the cut-off to improve bond breaking.[15, 19, 20] Dislocation dynamics, Brownian dynamics and microstructural evolution methods are used at the intermediate mesoscale.[21] The mesoscopic dynamical behavior of the polymer (matrix) is critical to exploring the CNT-matrix interactions. At the continuum scale, finite difference and finite element methods are

used to derive the composite properties, such as the distribution of stresses and temperatures.

Experimental results are necessary to parameterize, calibrate and validate computational models. Characterization methods from well-established to novel 3D imaging to high throughput techniques are needed to populate databases. The databases themselves will store both computational and experimental results. A well-defined taxonomy (ontology) needs to be comprehensive, scalable, mutable, and put foundations in place to anticipate future questions. Integration tools will bring together physics-based tools, databases and analysis tools in a cohesive environment. NanoHub.org is an example of a cyber infrastructure that provides for collaboration, access to physics-based simulation tools, and educational resources in nanoelectronics and nanoelectromechanical systems.[22] Materials informatics analysis tools will extract knowledge from large, complex data sets. These tools will facilitate data classification and clustering, critical feature identification and quantitative structure property relationships (QSPRs).

1.1.2 Military Aircraft Trends

ICME is applicable to industries (aerospace, automotive, electronics) where synergy of manufacturing, product design and materials yields a high quality solution. A closer look at trends in military aircraft underscores specific technical needs for materials development. The market for nano- and micro-unmanned aerial vehicles (UAVs) is growing rapidly.[23] Composites are the material of choice for UAV airframes. A composite material is made from two or more constituents with different physical and chemical properties, with a goal of improving overall composite properties. Fighter

aircraft have progressed to today's 5th generation fighters with advanced technologies such as very low-observable stealth and fully integrated weapons-sensors systems.[24] As technology requirements have increased payload, range, and signature requirements, fighter aircraft have incorporated more composites and other advanced materials for weight reduction, improved strength and stiffness, radar absorbance and heat resistance.[24]

1.1.2.1 Unmanned Aerial Vehicles (UAV)

Growth of the UAV market has exploded and that trend is expected to continue. From 2002 to 2008, the number of military UAVs increased from 167 to 6,000 within the military.[25] Advantages of using UAVs are cited as 1) reduced acquisition costs and 2) wider range of missions not limited by human physiology (longer loiter, contaminated environments).[25] Material performance drivers include high strength to weight ratio, high stiffness to weight ratio, reduced radar signatures and multifunctional properties. UAVs range in size from very small (~ 10 g) to large "tanker size" vehicles.[23] As UAVs move toward miniaturization as well as autonomous missions, the importance of optimizing materials properties will escalate. Power and weight are critical, especially as more computational resources must be included onboard to enable autonomous behavior and increase mission scope. The Air Force's view of UAV development is one of "plug-and-play" having a common airframe but a modular configuration to provide adaptability, sustainability and reduced cost, which intensifies the need for integrated materials development within product design.

1.1.2.2 Manned Aircraft

There is a wide variety of manned military aircraft from highly maneuverable fighters to low-observable long range bombers to high altitude reconnaissance vehicles. Fighter aircraft are loosely categorized by generation from 1st to 5th with materials playing an increasingly critical role with each new generation.[24] High performance composite materials were first introduced to 4th generation aircraft for secondary structure (e.g., airframe skin) to reduce weight (~1970-1990).[26] In the 4.5th generation (1990s-present), the focus was on new materials, primarily composite, to improve range, reduce weight and improve stealth.[24] For 5th generation, F-22 and F-35, use advanced materials for both very low observable (VLO) stealth performance and further weight reduction.[24] Advanced composites are used for secondary and primary structure while special coatings are applied for heat resistance and radar-absorbance.[27] From the 1970s, composite usage in military aircraft steadily increased but leveled off at approximately 30% by volume.[26] Inability to climb much above 30% composite usage is attributed to a “lack of confidence” (well proven design rules, hidden damage) and cost.[26] Composites have phenomenal advantages as well as several disadvantages

Titanium and steel have temperature-dependent properties yet to be achieved by composites. [28] Composite properties are still evolving, modes of failures are not well understood, and environment-based (solvent, moisture, temperature) interactions are problematic.[29]

Table 1-1: There are many advantages and disadvantages of composite materials.

Advantages	Disadvantages
• Lightweight • Stiffness • Strength • Directional control of properties • Formation of complex shapes • Fatigue resistance • Damping • Low thermal expansion • Low electric • Low radar visibility	• Cost of materials • Lack of well-proven design rules (e.g. "black aluminum") • Long development times • Low ductility • Solvent or moisture attack • Temperature limits • Sensitive to impact damage • Hidden damage • Cost of manufacturing

1.2 Carbon Nanotubes and Composites

Carbon nanotubes (CNT), discovered in 1991 by Iijima[30], can be described as a sheet of graphene rolled into a cylinder. There are single-walled CNTs, diameters on the order of 1 nanometer, and multi-walled CNTs, diameters on the order of tens of nanometers.[31] The ends can be open or capped, with a hemisphere of fullerene.[31] Lengths of single-walled nanotubes (SWCNT) range into the millimeters with the longest produced to date over 18.5 cm.[32] Their large aspect ratios (length to width) render CNTs quasi one-dimensional structures with great promise for a variety of applications.[33] Ballistic conduction, lack of sensitivity to electromigration and large current densities (theoretically 1,000 times that of copper) enable electronic applications such as field effect transistors and interconnects.[33-36] Multi-walled carbon nanotube (MWCNT) arrays have been successfully evaluated for on-chip thermal management for high performance processors.[37] Mechanically, CNTs are viewed as the ideal form of fiber and the ultimate filler for reinforcement of polymer composites.[33] Theoretically,

strength and stiffness of carbon CNTs are on the order of 100 and 1000 GPa, respectively.[1]

1.2.1 Structure

A SWCNT is described as a graphene sheet that has been rolled to form a cylinder. Graphene is a single sheet of sp^2 hybridized carbon with a hexagon repeating structure. A MWCNT is a rolled-up stack of graphene sheets to form concentric SWCNTs, with spacing between the shells equal to the inter-layer spacing of graphite (3.35 Å), consistent with experimental[38] and computational results[39]. SWCNTs are designated by the chiral vector (*n,m*), where *n* and *m* are integer indices of two graphene unit lattice vectors (Figure 1-2).

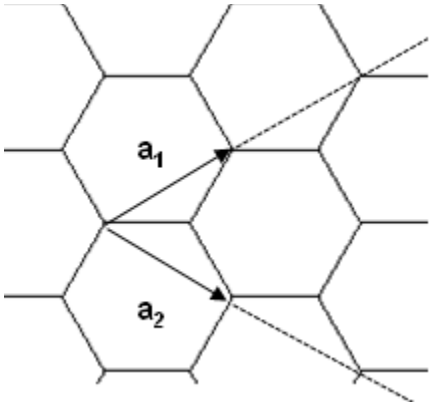

Figure 1-2: Graphene unit vectors for designating the (n,m) chiral vector have a dot product of 60 degrees.

There are three types of SWCNTs, zig-zag, armchair and chiral. Zig-zag have a chiral vector of (*n,0*) with a chiral angle of 0° (angle is shown in Figure 1-4). Armchair CNTs have a chiral vector of (*n,n*) and an angle of 30°. Chiral SWCNTs have a chiral vector of (*n,m*) with $m < n$ and chiral angle $0° \leq \theta \leq 30°$. Armchair, zig-zag and chiral SWCNTs are shown in Figure 1-3.

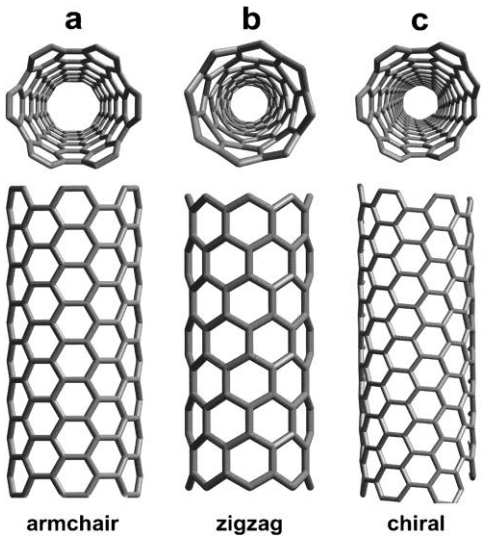

Figure 1-3: Nanotubes can be classified in three categories: armchair, zig-zag and chiral.

The chiral vector C_h is the vector sum of the graphene unit lattice vectors a_1 and a_2 and is the circumference of the CNT.

$$C_h = na_1 + ma_2 \quad (1)$$

Figure 1-4 illustrates the chiral vector (C_h), chiral angle (θ), and translational vector (T). The graphene sheet is rolled such that points B and B' overlap as do points O and A to create a (4,2) CNT.

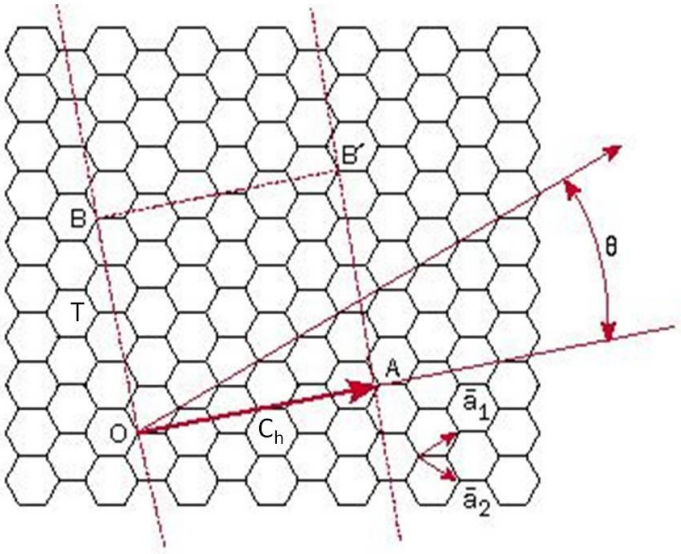

Figure 1-4: An unrolled CNT lattice shows the chiral vector, translational vector and chiral angle.[31]

The chiral angle is the angle between the direction of the chiral vector C_h and the a_1 lattice vector and is calculated from the following trigonometric relationships.

$$sin\theta = \frac{\sqrt{3}m}{2\sqrt{n^2+nm+m^2}}; cos\theta = \frac{2n+m}{2\sqrt{n^2+nm+m^2}}; tan\theta = \frac{\sqrt{3}m}{2n+m} \quad (2)$$

The translational vector is the length of the repeating unit cell defined in (3). GCD is the greatest common denominator.

$$T = \frac{\sqrt{3}|C_h|}{GCD(2n+m, 2m+n)} \quad (3)$$

Diameter can be calculated directly from the chiral vector C_h. a_{c-c} is the length of a carbon-carbon bond (1.44 Å) and $a_1 = \sqrt{3}a_{c-c}$. The dot product $a_1.a_1 = a_2.a_2 = (\sqrt{3}a_{c-c})^2$. Since the angle between a_1 and a_2 is 60 degrees, the dot product of $a_1.a_2 = \left(\frac{\sqrt{3}}{2}a_{c-c}\right)^2$.

$$d_t = \frac{|\boldsymbol{C_h}|}{\pi} = \frac{\sqrt{\boldsymbol{C_h}.\boldsymbol{C_h}}}{\pi} = \frac{\sqrt{3}a_{c-c}}{\pi}\sqrt{n^2 + nm + m^2} \quad (4)$$

MWCNTs are symbolized with repeating (n,m) parentheses. A triple-wall CNT is designated as (n-inner, m-inner)@(*n-middle, m-middle*)@(*n-outer, m-outer*).[40] Combination of (*n,m*) vectors that have graphite inter-layer spacing (3.35 Å) are energetically favorable. The most stable inner-outer combination for an armchair pair is (*m,m*)@(*m+5,m+5*) and for a zig-zag pairs is (*m*,0)@(*m*+9,0).[40]

1.2.2 Mechanical Properties

Nanotubes have exceptional mechanical properties. Table 1-2 lists average properties of CNTs and other reinforcement materials. Values for CNTs are theoretically calculated for pristine structures. Experimental measurements as well as other theoretical calculations vary greatly based on the number and type of defects.

Table 1-2: Pristine CNT structural properties outperform known materials.

Material	Young's Modulus (GPa)	Tensile Strength (GPa)	Density (g/cm^3)
Nanotube (theoretical)	1,000[41]	100-200[1]	0.7 – 1.7[1]
Carbon fibers (PAN-based)	230 - 595[42]	1.93 – 6.2[42]	1.8 – 2.0[42]
Glass fiber	72 - 85[42]	3.5 – 4.6[42]	2.5[42]
Steel	210[42]	0.34 – 2.1[42]	7.8[42]
Kevlar	130[42]	2.8[42]	1.5[42]

Two mechanical properties of interest are stiffness and strength. Young's modulus (elastic modulus) is a measure of stiffness defined as the ratio of axial stress (σ) to axial strain (ε) for ranges of stress in which Hooke's law holds true.[43] The earliest

theoretical study of Young's modulus calculated values between 1.5 and 5.0 terapascals (TPa) or 1,500 to 5,000 GPa.[44] More theoretical work has calculated Young's modulus for both SWCNTs and MWCNTs on the order of 1 TPa.[41, 45, 46] A discrepancy between theoretical calculations stems from the value of the wall thickness (proportional to cross-sectional area).[47, 48] Stress is force per area and stiffness is stress per strain. Wall thickness varies from 0.6 Å[44, 47] to 6.9 Å[49] with most using graphite interlayer spacing (3.35 Å) as the accepted value.[40, 50-52] Early experimental measurements for SWCNT and MWCNT are 1.25 -0.35/+0.45 TPa[53] and 1.8 +/- 0.9 TPa[54], respectively. More recent measurements found MWCNTs without inner wall linkages to have a Young's modulus of approximately 1 TPa.[55] A key point of interest is properties of CNTs vary based on their percentage defects (vacancies, surface functional groups, non-hexagonal linkages, impurities). Young's modulus for SWCNTs can decrease to 600 GPa (~40%) with 3% surface vacancies.[56] Experimental[55] and computational[57] studies of MWCNTs with cross-linked shells find that Young's modulus decreases. However, it has also been observed that multi-shell failure leads to increases in sustainable loads.[15, 55, 57]

Three types of strengths will be described – yield, ultimate and failure strengths. Yield strength is elastic-plastic deformation transition point noted as '1' in Figure 1-5. Beyond the yield point, a material will no longer return to its original shape once the applied stress is removed. Yield strain is the strain corresponding to the yield strength. Ultimate strength (tensile strength) is the maximum strength of the material, labeled '2'. Failure strength is the strength at which the material breaks, denoted as '3'. Experimental measurements near room temperature infer CNTs behave as brittle

materials[58]; thus, yield strength, ultimate strength and failure strength have approximately the same value.

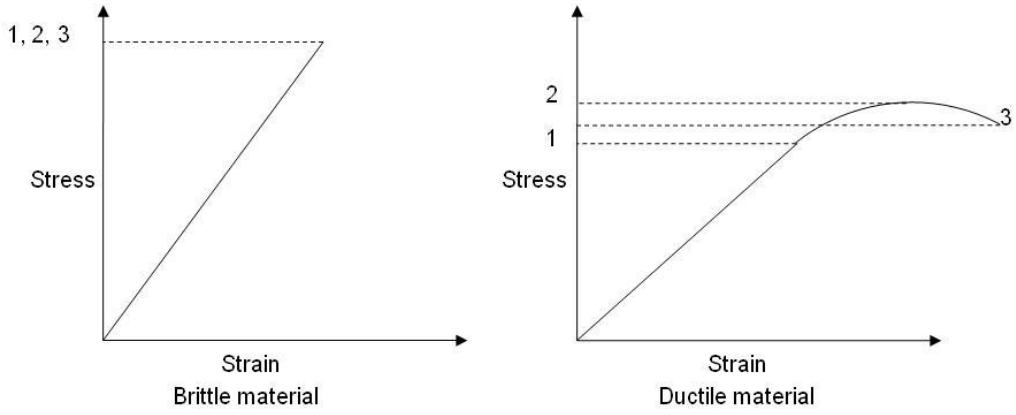

Figure 1-5: The stress-strain curves for brittle and ductile materials illustrating yield strength (label '1'), ultimate strength (label '2') and failure strength (label '3') for each.

Early calculations found yield strains to be 30-40%.[59] But, large time steps produced very high strain rates leading to anomalous results.[60] Theoretical studies with acceptable strain rates predict SWCNTs fail about 9+/-1%[60] and MWCNTs fail at 12+/-1%.[61] Tensile strength calculations (pristine CNTs) fall between 100 and 200 GPa.[62] Samsonidze calculated 150 – 180 GPa strength with a 17% strain[63], Zhang computed values between 100 and 170 GPa[64] and Belytschko generated strengths between 93.5 and 112 GPa at 15.8% to 18.7% strains.[62] With low levels of defects, Zhang calculated strength values of 88 – 105 GPa.[65] Experimentally, values have been much lower. Yu measured maximum failure strains of 5.3% and tensile strengths from 13 to 52 GPa[66] for SWCNTs and 11 to 63 GPa with maximum failure strains of 12% for MWCNTs.[51] Peng measured MWCNT fracture strengths between 97 and 110 GPa with failure strains of 10-12%.[55]

While CNTs have far superior properties to most materials, there is a large variation in mechanical values because of variation in size, chiral angle, waviness, vacancies, impurities, surface functionalization, etc. Quantifying the effect of these variables could lead to tailored optimization of CNTs reinforced composites realizing the full potential of this phenomenal material. One approach to navigate the large number of variables is coupling physics and informatics based methodologies. Growth and post-growth processing have an effect on the pristine structure of CNTs, leading to variation in structure and mechanical properties. Chemical vapor deposition (CVD) growth processes induce more defects than arc discharge growth.[2] Computational study of a Stone-Wales (combination of two heptagons and two pentagons) defect, single and double vacancies predicted reductions in SWCNT strength. Failure strain in a zig-zag SWCNT was reduced by 44% for a single Stone-Wales defect and 52% for a single one-atom vacancy.[19] For an armchair SWCNT, failure strain reduction was 45% and 61% for the Stone-Wales and single vacancy, respectively.[19] An experimental study of arc discharge grown MWCNTs measured a failure strength mean value of 102 GPa.[55] Electron irradiation of varying intensities reduced the failure strength from 10% to 40% while load transfer was increased by 240% to 1,160%.[55] Understanding the effect of inter-wall cross-linking will provide insight into the amount of irradiation required to tailor CNTs as desired. A computational investigation of the fracture strength for SWCNT and MWCNT with surface vacancies and inter-wall cross-linking concluded MWCNT-reinforced composites can indeed outperform SWCNT-reinforced composites, a paradigm shift in composite design methodologies.[14, 15] Defect-free SWCNTs do outperform defect-free MWCNTs but fracture strengths of SWCNTs are very sensitive to

surface defect size.[15] Fracture strengths for MWCNTs with 0.5 – 2.5% inter-wall linkages are relatively independent of surface defect size (for sizes greater than 2 nm).[15] Fonseca quantified the effect of inter-wall cross-linking on load transfer and Young's modulus as a function of linkage type.[57] For direct inter-wall cross-linking, stress gain transfer was 80% improvement at 5% defect density.[57] In general, mechanical properties of CNT-reinforced composites have fallen well short of expectations.[2, 67] The main reason is not being able to optimally engineer the polymer-CNT interface, partly due to the large number of potential variables.[2, 68, 69] Aggregate behavior (MWCNT concentric CNTs or entangled SWCNTs) responds differently than individual CNTs increasing the difficulty of polymer-CNT interfacial tailoring.[2, 69]

Understanding the variation of CNT structural properties caused by defects could lead to tailored CNT-reinforced composites. However, there are many computational challenges. First, molecular systems are large and throughput-intensive. Second, these material systems span multiple length and time scales. Third, MD potentials are optimized for specific atom types and combining results from more than one potential is not straightforward. Fourth, representation of appropriate statistical distribution for defects and aggregate behavior is needed. Informatics is the application of computational methodologies to process and interpret data to facilitate knowledge discovery (process-structure-property relationships, accelerated multi-scale design, optimization of material properties). Using informatics tools in parallel with physics-based techniques make the above challenges tenable.

1.2.3 Polymer Matrix Composites

Composites are engineered materials consisting of two or more constituent materials that have different chemical and physical properties. A two-phase composite has a matrix phase and a dispersed or reinforcing phase. A composite material benefits from the key features of both the constituents (improved flexibility from the polymer phase, strength from the fiber reinforcement). The rule of mixtures predicts the upper and lower bounds for the elastic modulus as a function of the constituent volume fractions of the matrix phase and reinforcement phase.[43] For composite axial elastic modulus, the upper and lower bounds are expressed in (5) and (6). E_m is the elastic modulus of the polymer matrix and E_f is the elastic modulus of the reinforcing fiber. V_m and V_f are volumes of the polymer matrix and fiber, respectively.

$$E_c^{upper} = E_m V_m + E_f V_f \tag{5}$$

$$E_c^{lower} = \frac{E_m E_f}{V_m E_f + V_f E_m} \tag{6}$$

A polymer is a macromolecule comprised of covalently bonded repeating units. There are two types of polymers, thermosets and thermoplastics.[70] Thermosetting polymers are cured (hardening agent, heat, irradiation) to form a 3-dimensional cross-linked network. Cross-linking is an irreversible, chemical change. Thermosets have high moduli and low strain to failure ratios (brittle material). Mechanical properties vary with length and density of cross-links and repeating units. Thermoplastics do not undergo cross-linking and retain their chemical structure with heating and cooling. They have low moduli and high strain to failure ratios (ductile material). Nylon has a failure strain of 40-80% while thermosetting epoxies range between 1-6%.[70] Mechanical properties vary with temperature, strain rate, monomer unit and molecular weight.

Higher molecular weights facilitate entanglement in amorphous polymers and a high degree of order in semi-crystalline systems.

1.2.4 Carbon Nanotube Reinforced Composites

Both SWCNT and MWCNT are used as fiber reinforcements in polymer composites. Qian dispersed 1% MWCNTs by weight in a polystyrene matrix to achieve 36-42% increase in Young's modulus and 25% increase in tensile strength.[71] Eitan dispersed 5% epoxide surface modified MWCNTs in a polycarbonate matrix and measured 25% improvement in Young's modulus compared to as-received MWCNTs.[72] Strength and strain to failure ratios improved by 13% and 15%, respectively, for the surface modified MWCNTs.[72] CNT-reinforced composites moduli varies with respect to growth process, composite -processing and surface functionalization.[2] On average, functionalized CNTs show the largest improvements, regardless of multi-walled or single-walled.[2] Moduli of 1% SWCNT reinforced nylon 6,10 composites improved by 38% (non-functionalized) and 132-162% (functionalized).[73] SWCNT nylon composite strength values improved by 17% (non-functionalized) and 149-163% (functionalized).[73]

Tailored optimization of CNT reinforced composite properties requires a complete understanding of four critical issues: 1) CNT dispersion, 2) CNT alignment, 3) CNT-matrix interfacial bonding, and 4) CNT aspect ratio.[74, 75] CNTs have a tendency to form agglomerates because of van der Waals interactions. This reduces surface area and interfacial slippage can occur, adversely affecting load carrying capacity. Maximizing CNT surface area with a uniform dispersion is essential.[76, 77] Alignment of CNTs is important for directional control of properties. Composite performance is directly affected by interfacial bonding. If it is too strong, there will be locations of

decreased toughness and failure along the interface.[78, 79] When the interfacial bonding is too weak, matrix fiber load transfer is not effective.[78, 79] Critical aspect ratio (AR_c) is the fiber length to diameter ratio at which the fiber and matrix fracture along the same plane (optimizing composite strength).[70] Fibers that have an aspect ratio less than AR_c will pull out of the matrix. Critical aspect ratios for MWCNTs and surface modified MWCNTs were measured at 300 and 100, respectively.[80]

CHAPTER 2

METHODOLOGY

Growth in nanotechnology research has seen advancements in synthesis, characterization and simulation methods. However, the number of questions to be addressed for a single material system is formidable. Coupling physics-based simulation tools with informatics methodologies is a proposed approach to navigate the large problem space. Materials informatics and molecular dynamics will be discussed.

2.1 Materials Informatics

Informatics is the creation, management and analysis of large, complex data sets drawing on physics, chemistry, mathematics and computer science. The key attributes of informatics are shown in Figure 2-1. *Data* (experimental and computational) is transformed into *information* by correlating it to other data. *Knowledge discovery* is facilitated by further analysis of many pieces of information. Informatics makes possible discovery of new process-structure-property relationships, accelerated multi-scale design, optimization of materials properties, and new theories for materials behavior.

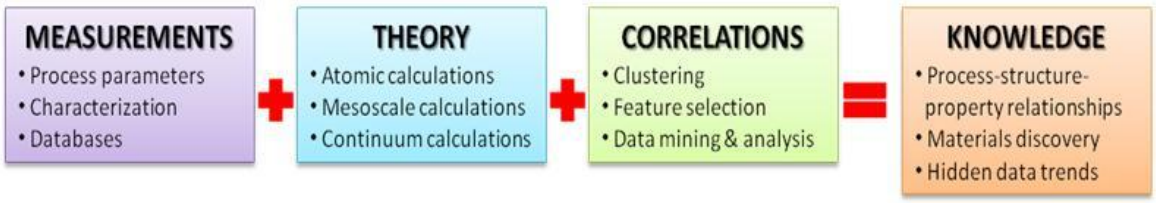

Figure 2-1: Materials informatics facilitates knowledge discovery by transforming computational and experimental data into information and analyzing the results.

Successful implementation of materials informatics needs to overcome two obstacles, 1) lack of organized data and 1) lack of data-mining and analysis methods.[81] The following informatics methods will be discussed.

- Representation of structural data
- Calculation of descriptors
- Quantitative-Structure-Property-Relationship (QSPR) model development

2.1.1 Representation of Structural Data

Representation and manipulation of 2D and 3D molecular structural data is a key task for cheminformatics. The "natural language" of chemists is the 2D graphical representation.[82] However 2D graphs only convey information about the topology (2D connectivity), not topography (3D arrangement), nor surface-mapped properties or conformational flexibility. For effective data handling, the structures need to be represented in some type of computer-readable form revealing maximum information (composition, connectivity, topography, properties, etc).

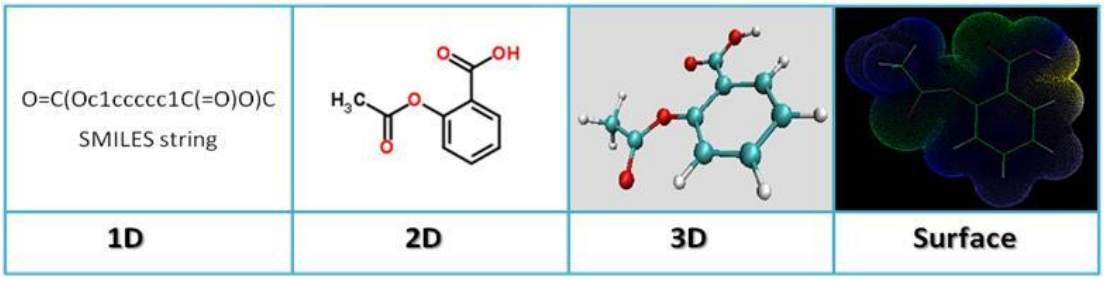

Figure 2-2: Molecules can be represented in many forms, from 1-dimensional to 3D surface mapped properties. Aspirin is illustrated here as an example.

Figure 2-2 illustrates the hierarchical scheme for the representation of aspirin with increasing information content. Line notations encode structural information as a linear sequence of letters and numbers (e.g., IUPAC nomenclature). Line notations can

encode 2D structural information as SMILES (simplified molecular input line entry system)[83] or 3D as IUPAC InChI (international chemical identifier).[84] Graphs are used for 2D representation and consist of nodes (atoms), and edges (bonds).[85] Connection tables are used to represent a graph (i.e., Molfile).[86] A 3D structure conformation needs each atom's x, y, z coordinates. Connectivity information can be explicitly defined (e.g., Protein Data Bank pdb file) or implicitly derived from bonding distances between atoms.[87] 3D structural conformations can be created from 2D representations, the earliest program was CONCORD.[88] Surfaces and surface-mapped properties are produced from 3D conformations but stored as x, y, z coordinates and the surface property values. CMD's "field point" representation of electrostatic, steric and hydrophobic fields mapped to the solvent accessible surface is an example of a surface-mapped property.[89]

In the same manner that molecular structural data has been represented in machine readable formats for chemical problems, materials structural data needs to be organized and represented similarly. There are two main differences between materials and pharmaceutical chemical problems. Cheminformatics is focused on molecular problems, limited to a single molecule or small molecule-receptor complex. Materials span multiple length scales and material composition is not limited to a single type. Type is defined to mean multiple simulation codes are required to model the system. For example at the molecular level, studying the yield strength of a CNT-reinforced epoxide composite grown from metal catalyst requires reactive potentials parameterized for carbon-metal, carbon-carbon and carbon-oxygen at a minimum. Figure 2-3 is an illustration of types of structural complexity.

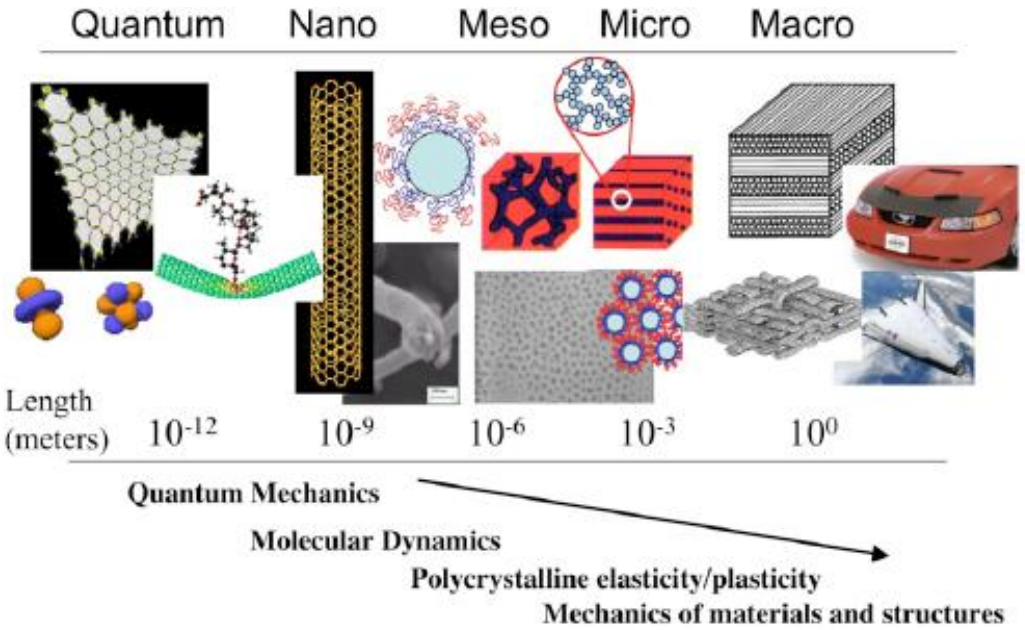

Figure 2-3: Structural complexity for materials span several time and length scales.[90]

Mesoscopic is defined as the "in-between" scale, between molecular and microstructure.[91] It addresses curvature and shape of meso-components, interfacial chemistry, morphology and certain topological defects.[91] Microstructure tackles features on the order of microns, such as grain size, void volume and distribution, dislocations.[10]

2.1.2 Descriptors

Molecules are real objects rich in chemical information, represented by structural models (Figure 2-2). A single model cannot convey all the chemical information inherent in a molecule. Therefore, several different types of models are used to represent a single molecule. Model properties are characterized by descriptors (variables) in structure-property relationships. There are thousands of pharmaceutical descriptors. E-DRAGON (freely available) and DRAGON (commercial) calculate more than 1,600[92] and 3,200[93] descriptors, respectively.

There are no hard and fast categories for molecular descriptors but the following table provides examples of common types. Dimensionality is the type of structural model from which the descriptor was derived.

Table 2-1: There are six general categories for descriptor types, based on dimensionality. Examples are provided for each type.

Category	Example	Dimensionality
Constitutional	Molecular weight	1D
	Number of methyl groups	1D
Topological	Kappa shape indices[94]	2D
	Randic connectivity index[95]	2D
Geometrical	Topographical indices[96]	3D
	Spherosity[97]	3D
Geometrical-Surface	Molecular electrostatic potential	3D-surface
	Hydrogen bonding potential	3D-surface
Physicochemical	Boiling point	1D
	Hydrophobicity	1D
Quantum Mechanical	Heat of formation	3D
	Molecular polarizability[98]	3D

Constitutional descriptors provide data about chemical composition (molecular weight, number of a structural fragment, bond counts). Topological descriptors reflect 2D connectivity information. Kappa shape indices calculate a measure of molecular shape compared to the most linear and most connected graph possible.[94] Geometrical descriptors convey 3D structural characteristics and conformational flexibility. Topographical indices are a measure of branching and shape for 3D structure.[96] Geometrical-surface descriptors yield 3D distribution information about various fields

(e.g., molecular electrostatic potential, hydrogen bonding potential). Physicochemical descriptors are physical and chemical properties that are measured (e.g., boiling point, temperatures, hydrophobicity). Quantum mechanical descriptors are derived from quantum level calculations including heat of formation, polarizabilities, dipole moments and orbital electron densities.[98]

Once a set of molecular descriptors has been calculated, it is necessary to vet the mathematical characteristics. Mean, standard deviation and coefficient of variance calculations are in (7), (8), and (9). Coefficient of variance evaluates whether a particular descriptor has inclusion value.[99] The mean and standard deviation are used in auto-scaling.

$$\mu = \frac{1}{N}\sum_{i=1}^{N} x_i \tag{7}$$

$$\sigma = \sqrt{\frac{1}{N}\sum_{i=1}^{N}\left(x_i - \mu\right)^2} \tag{8}$$

$$c_v = \frac{\sigma}{\mu} \tag{9}$$

Auto-scaling is a common data-preprocessing technique combining mean centering with unit variance scaling (UV-scaling), shown in (10).[82] Descriptors frequently have different numerical ranges and it is important to scale their values to weight all descriptors equally in the analysis. To mean-center about zero, subtract the mean value of a set of data from each of the individual points (numerator in (10)). UV-scaling weights all descriptors equally by dividing all mean-centered values by the standard deviation of the data set.

$$x_i' = \frac{x_i - \mu}{\sigma} \tag{10}$$

Correlation analysis provides a measure of dependence between descriptors. The Pearson correlation coefficient *r* calculates the measure of correlation between two descriptors *x* and *y*, in (11).[100] The coefficient varies between +1 (perfectly positively correlated) and -1 (perfectly negatively correlated).

$$r = \frac{\sum_{i=1}^{N}\left[\left(x_i - \mu_x\right)\left(y_i - \mu_y\right)\right]}{\sqrt{\sum_{i=1}^{N}\left(x_i - \mu_x\right)^2 \sum_{i=1}^{N}\left(y_i - \mu_y\right)^2}} \tag{11}$$

Descriptors must be defined at multiple length scales and for all material types in the system. The CNT-reinforced epoxide composite grown from metal catalyst has multiple components. At the simplest level, there is CNT reinforcement and a polymer matrix. The polymer properties near the CNT surface diverge from the bulk polymer properties. [101] This region is defined as the interphase and is a third component in this system. Further, the polymer could be a blend of two or more, increasing the complexity. To fully capture the details of the system, each component (CNT, polymer, interphase) and all the interactions (CNT-polymer, CNT-interphase, interphase-polymer, CNT-CNT, CNT-metal, polymer-metal, etc) must be included in the analysis across all length scales. Descriptors can capture the critical information about each component and interaction, reducing the need for large, complex simulations of complete material systems. Further, it may be possible to investigate material systems that are currently not addressable due to size and lack of appropriate simulation methods. Figure 2-4 lists potential CNT and CNT-polymer properties.

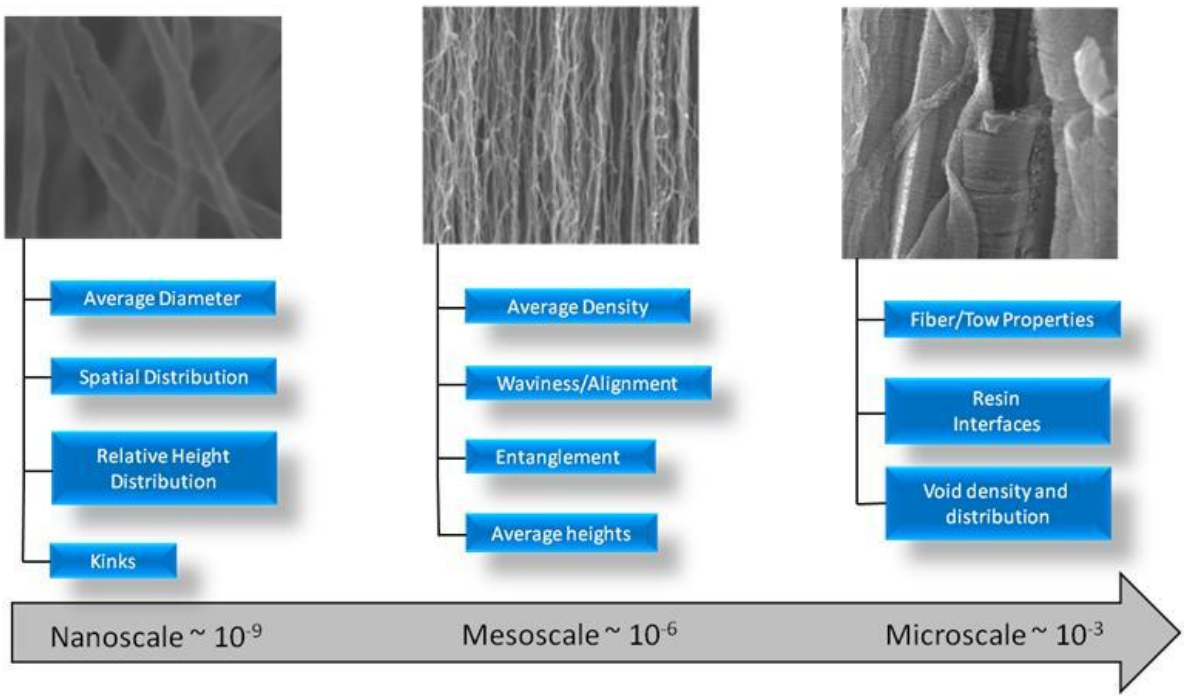

Figure 2-4: There are several potential descriptors for CNTs at the nanoscale, mesoscale and microscale.

2.1.3 Model Development

Mathematical model development has multiple steps. First, *data preparation* collects and pre-processes experimental and computational data. Second, quantitative structure property relationship (QSPR) *model building* a) clusters or classifies data, b) selects a set of features and c) develops a multivariate mathematical model for the property of interest. Third, *model validation* quantifies accuracy, robustness and predictive performance and defines the domain of applicability.

2.1.3.1 Data Clustering

Data clustering selects a subset of data for analysis by measure of a similarity metric. Analyses could be data from distinct clusters (very similar behavior) or from each of the homogeneous clusters to maximize coverage of activity space. Clustering

algorithms are unsupervised methods that divide heterogeneous data into homogeneous subgroups. Clustering is based on the similar property principle stating similar molecules have similar behavior (neighborhood behavior).[102] Unsupervised learning does not use information about the dependent variable. Classification is a supervised learning method that associates input data with the corresponding dependent variable. The clustering process is as follows.

1) Generate a set of suitable descriptors for the full data set.
2) Choose an appropriate metric of similarity.
3) Cluster the data into subgroups.
4) Examine results and select an appropriate subset based on the analysis goals (e.g., data reduction, diversity analysis).

Similarity (or conversely, the distance) is a numerical quantification of two objects' proximity. There are several similarity metrics but a handful has emerged for pharmaceutical applications. The Tanimoto coefficient and Hamming distance are two popular metrics.[103] The Tanimoto coefficient only considers the presence of attributes while the Hamming distance includes both the presence and absence of specified attributes. As with chemical data, it will be imperative to use standard materials datasets to benchmark performance of various similarity metrics, including utilization of composite scoring techniques, combining individual rankings into a single resultant score.[104]

There are two classes of non-overlapping clustering methods, hierarchical and non-hierarchical. Non-overlapping means each entity can only have membership in a

single cluster. Figure 2-5 provides types and examples of clustering algorithms, in-depth reviews are available by Downs and Jain.[105, 106]

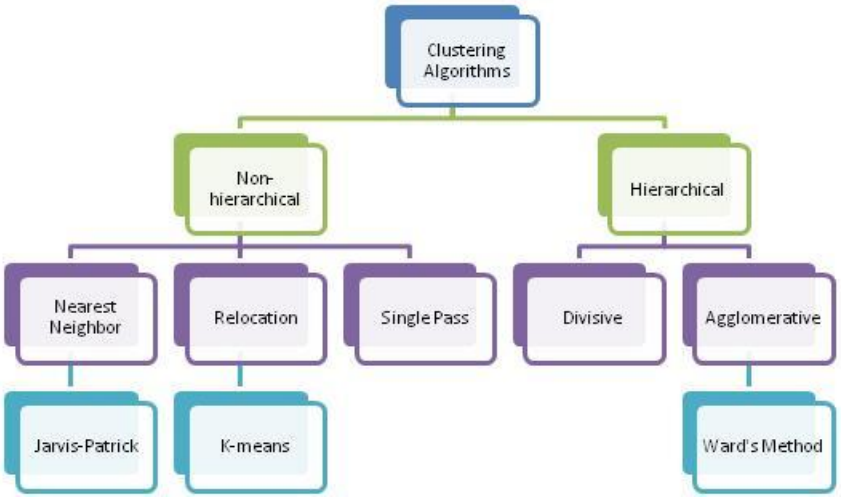

Figure 2-5: There are hierarchical and non-hierarchical clustering algorithms. Subcategories and examples of each are shown here.

Hierarchical methods iteratively divide (from full set) or merge (from single entities) to form clusters. Non-hierarchical methods select subgroups without forming a hierarchical relationship between clusters. Relocation methods start with a set of randomly selected centroid seeds, entities are assigned to clusters based on similarity to centroid. Centroids are recalculated, entities are relocated and this process continues until convergence or pre-defined iteration limit is exceeded. A popular relocation algorithm is the K-means method.[107] Nearest neighbor methods calculate pair-wise similarity between all compounds and create a nearest neighbor list for each entity. Criterion for assignment to a specific cluster is based on similarity between nearest neighbor lists. Two widely used cluster algorithms are Ward's method[108] and Jarvis-Patrick.[109] Ward's method usually outperforms Jarvis-Patrick and forms clusters

of equal size.[110, 111] Jarvis-Patrick is more computationally efficient than Ward's method (complexity of $O(N^2)$ versus $O(N^3)$).[112]

2.1.3.2 Feature Selection

The number of descriptors for a data set is the dimensionality. Feature selection is the crucial task of selecting the optimal descriptors for model building, balancing accuracy with interpretability. Filters and wrappers are two types of feature selection algorithms. Filters are computationally efficient, selecting variables as part of data pre-processing.[113] Wrapper methods are computationally inefficient learning algorithms and select features based on their predictive power.[113] Pearson correlation coefficients and principal component analysis (PCA) are filters.[113] Genetic algorithms, backward elimination methods and forward selection methods are wrappers.[113] Wrappers must have a scoring function to calculate predictive power. Lack of fitting (LOF),[114] compound standard error (CoSE)[115] and predictive residual error sum of squares (PRESS)[116] are common scoring functions. Selection methods are invariant to a chemical or materials application. But, it is likely that the number of additional length scales for material systems will increase complexity of feature selection.

Principal component analysis (PCA) transforms the original set of variables into a set of uncorrelated latent variables (principal components).[117] The first principal component captures the largest percentage of variance in the data; the second principal component captures the second largest, etc.[117] Scree plots[118] and 2) the "greater than 70% explained variance" rule of thumb[119] are both used to determine the minimal number of principal components to retain. Loadings and score plots are PCA tools that can reveal hidden or simplified structure in complex, large data.[112, 120]

Genetic algorithms (GA) mimic the natural adaptation in biological systems.[121] GAs work well for noisy, non-linear, medium-to-large data sets outperforming other feature selection algorithms.[121] However, GAs are computationally inefficient, are not guaranteed to converge to a global optimum and accuracy is dependent on the scoring function.[122] GAs have also been shown effective in outlier removal.[123, 124]

2.1.3.3 Quantitative Structure Property Relationship Models

Quantitative structure property relationships (QSPRs) are multivariate models relating the property of interest to the material structure. Descriptors are calculated to represent different information about the structure and are the independent variables in the QSPR. Linear, non-linear regression, partial least squares (PLS) and kernel-PLS are techniques to create QSPRs.[116, 125, 126] Linear regression identifies the relationship between a dependent variable *y* and one or more independent variables x_1, x_2, x_n by minimizing the difference between the actual and predicted values finding coefficients a_0, a_1, a_n.[127] $\bar{x}$ is the mean value and x_i are the observed x values. Calculations for the first two coefficients are shown in (12). Linear regression is solved with closed-form equations and always converges to a unique solution.[127]

$$y = a_o + a_1 x_1 + a_2 x_2 + \cdots + a_n x_n$$

$$a_1 = \frac{\sum_{i=1}^{N}(x_i - \bar{x})(y_i - \bar{y})}{\sum_{i=1}^{N}(x_i - \bar{x})^2} \qquad (12)$$

$$a_0 = \bar{y} - a_1 \bar{x}$$

Nonlinear solves mathematical functions that are nonlinear in the parameters. Nonlinear regression is an iterative process. The equation $y = a_o + a_1 x_1 + a_2 x_2^2$ is nonlinear in the variable x_2 but a simple substitution (i.e., x_3 equals x_2^2) transforms the

equation into a linear problem. The equation $y = a_0 + a_1 e^{b_2 x_1}$ is nonlinear in the parameter b_2 and a substitution cannot make it a linear problem. Kernel methods are techniques to solve nonlinear problems.[119] Nonlinear regression is solved iteratively, is not guaranteed to converge or have a unique solution. [127]

Partial least squares (PLS), or projection to latent structures, is an extension to principal component regression (PCR) that explains variance in the independent and dependent variables.[128] For PCR, the independent variables are the principal components (found with PCA). It is advantageous to use PLS when the number of variables is large relative to the number of data sets, with multicollinearity, and with more than one dependent variable.[128] Interpretability is challenging because of the multiple projections of both the independent and dependent variables.

2.1.3.4 Validation

Rigorous validation is crucial to model development and provides metrics on statistical significance, robustness, and predictive power. Calculation of statistical significance is common but robustness and predictive power are less practiced.[129] The coefficient of determination R^2 is the squared correlation coefficient that provides statistical significance. It is calculated in (13), ($y_i, y_{calc,i}, \bar{y}$ are the observed, calculated and average values, respectfully).[112]

$$R^2 = 1 - \frac{\sum_{i=1}^{N}\left(y_i - y_{calc,i}\right)^2}{\sum_{i=1}^{N}(y_i - \bar{y})^2} \qquad (13)$$

The cross-validated R^2 (Q^2 or q^2) calculates a metric of robustness.[130] Cross validation methods remove one or many values from the data set to create a test set, use the remainder of the data as a training set and calculate R^2. This is repeated

multiple times to obtain a mean Q^2 value (average all R_i^2 values). Cross-validated leave-many-out (CV LMO) has better performance than cross-validated leave-one-out (CV LOO).[131] Two other measures of robustness are bootstrapping[132] and y-scrambling.[133] Measure of predictive power is best derived from external validation methods but not always feasible due to lack of data. External validation methods separate the data set into training and test sets. The calculation of external Q^2 is shown in (14), ($y_{test\_i}, y_{test\_calc,i}, \bar{y}_{train}$ are the observed test values, predicted test values and average training value).[129]

$$Q^2_{ext} = 1 - \frac{\sum_{i=1}^{N,test}\left(y_{test\_i} - y_{test\_calc,i}\right)^2}{\sum_{i=1}^{N,test}\left(y_{test\_i} - \bar{y}_{train}\right)^2} \quad (14)$$

Assuming that a high Q^2 value is indicative of predictive ability is incorrect.[130] It is recommended to use the following set of criteria.[130]

$$Q^2 > 0.5$$

$$R^2 > 0.5$$

$$0.85 \le k \le 1.15; k = \frac{\sum y_i\, y_{calc,i}}{\sum y^2_{calc,i}}$$

$$\frac{(R^2 - R_o^2)}{R^2} < 0.1; R_o^2 = 1\frac{\sum\left(y_{calc,i} - y_i^{ro}\right)^2}{\sum\left(y_{calc,i} - \overline{y_{calc}}\right)^2};\ y_i^{ro} = k y_{calc,i}$$

Figure 2-6: To assess predictive ability accurately, the following four criteria are recommended.

2.1.3.5 Domain of Applicability

Domain of applicability is defined as the "response and chemical structure space in which the model makes predictions with a given reliability."[134] The distance from a potential data point to a data set is calculated and if it falls within the user-defined

threshold value, it is considered part of the domain of applicability. Leverage, h_i, is a distance-based metric used in domain of applicability calculations.[135]

$$h_i = x_i^T (X^T X)^{-1} x_i \quad (15)$$

X is the *n* by (*k – 1*) matrix of *k* model descriptor values for *n* training set observation and x_i is the descriptor row vector of the potential data point. This value is compared to a warning leverage h^*, which is usually set at *3k/n* (*n* is the number of data points in the set, *k* is the number of parameters or independent values). If leverage is greater than the warning leverage, the model is not considered reliable for the data point in question. A William plot, which is a plot of standardized cross-validated residuals versus the leverage values, is a visual evaluation tool for domain of applicability.[131]

2.2 Molecular Dynamics

Molecular dynamic (MD) simulations integrate Newton's laws evaluating the position and velocities of particles at time-consecutive configurations of the system. Thermostats maintain constant temperature and periodic boundary conditions are used to estimate accurate bulk properties with a small number of particles. Molecular dynamics (MD) compute equilibrium and transport properties for systems that are too large to be treated with quantum mechanics. MD is based on a fundamental hypothesis of statistical mechanics – the system ensemble average is equal to the time average.[136]

Ab initio methods explicitly solve the Schrodinger equation, with few approximations. But, computational cost limits the use of *ab initio*. Coupled cluster with single, double, and triple perturbative excitations (CCSD(T)) scales as N^7 while Moller-Plesset perturbation theory (MP2) scales as N^3, where N is the number of electrons.[137]

MD methods scale as N^2 (theoretical maximum considering all pair-wise interactions) but usually implemented as N or NlogN, where N is the number of atoms. Electronic and quantum predictions are not possible with MD because it is based on classical mechanics. MD force fields (potential) are parameterized from *ab initio* and experimental data for specific atom types, limiting applicability. Development of an effective potential is tedious and should satisfy four conditions. First, the potential energy function should be flexible, accommodating as wide a range of fitting data as possible.[138] Second, the potential should reproduce the fitting database with accuracy.[138] Third, it should satisfy the condition of transferability, at least being able to qualitatively describe structures not included in the fitting database.[138] Finally, the potential energy function should be computationally efficient.[138]

2.2.1 Generic Steps of Molecular Dynamics

There are four steps in an MD simulation, 1) initialize particle positions and velocities, 2) calculate forces acting on the particles, 3) integrate equations of motion to find new positions and velocities and 4) calculate properties of interest.[136, 139] In the initialization step, parameters (temperature, time-step, simulation time, etc) are provided. The initial positions are determined by system geometric and initial velocities are set by a Maxwell-Boltzmann distribution at the temperature of interest, setting the total kinetic energy to the total average statistical thermal energy, shown in (16).[139] T is the temperature, m_i (v_i) is the mass (velocity) of the each particle, N is the total number of particles and k_b is the Boltzmann constant.

$$\sum_{i=1}^{N} \frac{m_i v_i^2}{2} = \frac{3Nk_bT}{2} \qquad (16)$$

Many-body interactions (scale as N^2 with N representing the number of atoms) must be considered to calculate the forces on the particles. The force *F* on each particle is the negative first derivative of the potential energy function *V* with respect to position, shown in (17).

$$F_{ij} = -\nabla V = -\frac{\partial V}{\partial r_{ij}} = m_i \frac{d^2 r_{ij}}{dt^2} \quad (17)$$

Force calculations can be computationally reduced to scale as N by using efficient techniques for short and long range inter-atomic interactions.[140] To derive the new particle positions, velocities and accelerations, Newton's equations of motion are integrated with a predictor or predictor-corrector algorithm.[139] For this study, the velocity Verlet predictor algorithm is used.[141, 142]

2.2.2 Force Fields

The reactive empirical bond order (REBO) is one of the most successful potentials for describing molecular interactions in hydrocarbon systems. The theoretical basis for REBO was derived by Abell in 1985 from chemical pseudopotential theory.[143] Chemical binding energy E_b is written as a sum over nearest neighbor interactions in (18).[143]

$$E_b = \sum_i \sum_{j>i} [V^R(r_{ij}) - b_{ij} V^A(r_{ij})] \quad (18)$$

The functions are the pair-wise additive interactions for all inter-atomic valence electron repulsions V^R and attractions V^A, modeled as Morse-type equations. The term b_{ij} characterizes the many-body coupling between the bond from atom *i* to atom *j* in the

local environment of atom *i*. There are no predetermined atomic hybridizations, as with traditional force fields, and the local environment is used to calculate inter-atomic interactions; thus, covalent bond breaking and reformation is allowed.[18] Bond strength (bond order) has a complicated relationship with geometry but Abell argued that the local coordination number N is the primary factor. Using a Bethe lattice, he derived the following relationship.[143]

$$b \propto (N)^{-1/2} \tag{19}$$

Tersoff implemented Abell's theory as analytic parameterized forms describing covalent bonding in silicon and carbon structures.[144] Tersoff's derivation considered short range forces only.[145] Brenner extended Tersoff's potential to correct for over-binding of radicals and properly describe conjugated and unconjugated systems by including nonlocal effects to a first approximation (for example, capturing the difference in a C-C double bond character for 2-3-dimethyl-2-butene versus graphene).[145] He also extended the potential to accurately represent hydrocarbon systems. This potential is the first generation REBO (REBO-1st). REBO-1st is limited in that it is too restrictive to simultaneously fit equilibrium distances, energies and force constants for C-C bonding.[18] Also, both attractive and repulsive terms tend to finite values as the distance between atoms decreases.[18] The second generation REBO (REBO-2nd) improved the analytic functions and used an extended fitting database proving more accurate descriptions of bond energies, bond lengths and force constants as well as elastic properties and interstitial defect energies.[18] The analytic forms of the repulsive and attractive potentials for REBO-2nd are in (20) and (21).[18]

$$V^R(r) = f^c(r)\left(1 + \frac{Q}{r}\right)Ae^{-\alpha r} \quad (20)$$

$$V^A(r) = f^c(r)\sum_{n=1,3} B_n e^{-\beta_n r} \quad (21)$$

The repulsive term is a screened Coulomb potential that tends to infinity as the inter-atomic distance approaches zero. The attractive term overcomes the limitation of the Morse-type function to simultaneously fit the bond energies, lengths and force constants. $f^c(r)$ is a cutoff function that limit the range of covalent interactions to a finite radius. For this implementation, $f^c(r)$ is 1 for nearest neighbors and 0 for all others. *Q, A, B,* α and β are two-body adjustable fitting parameters that depend upon the types of interacting atoms.

The bond order term b_{ij} is a weighting factor for $V^A(r)$ based on the likelihood of bond formation. It depends on the local coordination number, bond angle, dihedral angle for C-C double bonds and conjugation or radical character.[18] Calculation of bond order is shown in (22) and (23).

$$\overline{b_{ij}} = \frac{1}{2}\left[b_{ij}^{\sigma-\pi} + b_{ji}^{\sigma-\pi}\right] + b_{ij}^{\pi} \quad (22)$$

$$b_{ij}^{\pi} = \prod {}_{ij}^{RC} + b_{ij}^{DC} \quad (23)$$

$b_{ij}^{\sigma-\pi}$ and $b_{ji}^{\sigma-\pi}$ depend on local coordination and bond angles for atoms *i* and *j* (original Tersoff implementation) and b_{ij}^{π} is a corrective term added by Brenner in REBO-1st to 1) capture radical character and conjugated systems ($\prod {}_{ij}^{RC}$), and 2) dependence on the dihedral angle for C-C double bonds (b_{ij}^{DC}).[18]

There are two major deficiencies for REBO-2nd. It lacks the inclusion of non-bonded interactions and torsional interactions (rotational barriers about single bonds).

These deficiencies are compensated for in the adaptive intermolecular reactive empirical bond order (AIREBO).[146]

$$E_{AIREBO} = E_{REBO} + E_{non-bonded} + E_{torsional} \quad (24)$$

Non-bonded interactions (van der Waals forces) are critical to the description of CNT-based systems. AIREBO implemented the 12-6 Lennard Jones (LJ) potential to account for van der Waal interactions in (25).[146, 147]

$$V_{LJ}(r_{ij}) = 4\varepsilon_{ij}[\left(\frac{\sigma_{ij}}{r_{ij}}\right)^{12} - \left(\frac{\sigma_{ij}}{r_{ij}}\right)^{6}] \quad (25)$$

Fitting parameters between atoms *i* and *j* are ε_{ij}, potential well depth, and σ_{ij}, distance where the potential between atoms *i* and *j* is zero. AIREBO tests three conditions to adaptively determine whether or not to include the LJ potential. These are 1) distance of separation for atoms *i* and *j*, 2) strength of their bonding interaction and 3) bond network connecting the atom pair.[146] This approach accurately captures non-bonding interactions without compromising the ability of REBO-2nd to form new bonds. Torsional interactions, more important in describing saturated hydrocarbons than CNTs are incorporated through an empirically derived term (26).[146] ω is the dihedral angle of the bond between atom pair.

$$V^{tors}(\omega) = \varepsilon[\frac{256}{405}cos^{10}\left(\frac{\omega}{2}\right) - \frac{1}{10}] \quad (26)$$

The dihedral angle potential is based on the local coordination environment. The constants were chosen such that when the potential was summed over the nine dihedral angles between identically substituted sp^3 carbons, the overall molecular

torsional potential has the expected three-fold symmetry with a minimum of zero and a maximum barrier height ε.[146]

2.2.3 Thermostat

The default MD simulation is to sample a microcanonical (constant NVE) ensemble where N is the number of particles, V is volume and E is energy. To be compatible with experiment, it is necessary to maintain a constant temperature (T) by sampling a canonical (constant NVT) ensemble. Thermostats are used to 1) maintain a constant temperature, 2) study temperature dependent processes, 3) remove heat in dissipative non-equilibrium MD simulations, and 4) avoid energy drifts due to numerical error accumulations.[140, 148] The Berendsen thermostat is implemented in this research and is based on a first-order relaxation equation with weak coupling to an external heat bath in equilibrium.[149] The Berendsen thermostat scales the velocities at each iteration step, adding a frictional force, proportional to the velocity, which smoothly reduces the kinetic energy to the correct value. The thermostat is simple, robust, and efficient with the formalism shown in (27), (28) and (29). The term $\varphi \frac{dr_{ij}}{dt}$ is the velocity scaling frictional force, γ is a user defined coupling constant, T_D is the desired system temperature and T is the current calculated system temperature.[148]

$$m_i \frac{d^2 r_{ij}}{dt^2} = F_{ij} - \varphi \frac{dr_{ij}}{dt} \tag{27}$$

$$\varphi = \gamma(1 - \frac{T_D}{T}) \tag{28}$$

$$T = \sum_{i=1}^{N} \frac{m_i v_i^2}{3k_b} \tag{29}$$

2.2.4 Numerical Integration

Newton's equations of motion are a linear, second order ordinary differential equation. With a continuous potential energy, motions of particles are coupled together creating a many-body problem that cannot be analytically solved. Numerical solutions to the many-body problem are found with predictor or predictor-corrector finite difference algorithms.[139] Good integration methods should conserve energy and momentum while permitting a long time-step δt and be time-reversible. The velocity Verlet predictor algorithm is implemented in this research.[141, 142] Predictor-corrector finite difference methods are more accurate but inefficient because they require two force calculations per iteration.[139] For each time-step in the simulation, the velocity Verlet algorithm 1) calculates the force at time t, 2) finds the acceleration from the force and 3) integrates to find new positions and velocities at time $t + \delta t$ (assumes constant force over δt). The choice of time-step is critical, too small and the simulation is wasting computational resources and only covering a limited amount of the desired phase space. If the time-step is too large, the simulation could yield anomalous results due to violations of energy and momentum conservation.[140] MD time-steps are limited by the fastest motion, the C-H bond stretching (~10^{-14} s).[139] For hydrocarbons, a time-step of 0.5 femtoseconds works well.[48, 60] The velocity Verlet method provides time-synchronized kinematic variables (position, velocity, acceleration) without compromising position.[142] This is an improvement over the popular leap-frog Verlet algorithm, which cannot provide time-synchronized kinetic information.[150] The velocity Verlet algorithm is shown in (30) and (31).

$$r(t+\delta t) = r(t) + \delta t v(t) + \frac{1}{2}\delta t^2 a(t) \quad (30)$$

$$v(t+\delta t) = v(t) + \frac{1}{2}\delta t[a(t) + a(t+\delta t)] \quad (31)$$

2.2.5 Periodic Boundary Conditions

An obstacle to an MD simulation is the large fraction of surface molecules. For example, if one thousand molecules are equally distributed in a 10 x 10 x 10 unit box, at least 488 molecules (~50%) reside on the cube faces.[140] Applying periodic boundary conditions (PBC) is a technique to effectively replicate a unit cell from the bulk lattice. A simulation with a small number of particles can experience forces as if they were part of the bulk lattice. In two dimensions, a square filled with particles is replicated in all directions such that the square is in the center of a 3 x 3 grid of identically filled squares. As particles move in the original box (central square of grid), the clone particles in the image squares move exactly the same way. If a particle exceeds the box's boundaries, it re-enters the other side (via a translation vector $x(r + T) = x(r)$ where T is an integer multiple of the width and height of the box sides) allowing the number of particles in the box to remain constant. PBCs can be implemented in 1, 2 or 3 axes. For example, PBCs are implemented for nanotubes along the axial direction (z-axis). The minimal cell size must be large relative to the range of molecular interactions or anomalous behavior will occur due to interaction of particles with their clones in image boxes.

CHAPTER 3

CNT DESCRIPTORS, STRUCTURE-PROPERTY RELATIONSHIPS

Values for carbon nanotube (CNT) mechanical properties vary due to a multitude of variables. A powerful approach that has not been applied to CNT mechanical property prediction is the development of descriptors and quantitative structure property relationships (QSPR). Twenty CNT computational descriptors are developed using a set of 78 Molecular Dynamic (MD) simulations. A subset of critical descriptors is selected and QSPRs are built from that subset. For Young's modulus, two descriptors were of critical importance: the density of the non-sp^2 hybridized carbons (C_{N2} / C_T) and the density of the number of methyl functional groups (M_N / C_T) on the CNT surface. QSPRs had an R^2 greater than 0.9. It is hoped that these two variables can be easily experimentally measured, paving the way for closed-loop computational-experimental development. For Poisson's ratio, a limiting value for armchair and zig-zag CNTs (wide range of diameters, defect density from 0% to 3%) was found to be 0.23 and 0.10, respectively.

3.1 Introduction

CNTs have unparalleled mechanical, electronic and thermal properties.[1, 2] With strength and stiffness values of 100 and 1,000 GPa, respectively, CNTs are thought to be the ultimate reinforcement in polymer composites.[1, 33, 68] CNTs have been used to reinforce polymer, ceramic and metal matrices for improved stiffness, strength and toughness.[151-154] Pristine, isolated single wall CNTs (SWCNT) are rarely available.[2] Chemical vapor deposition (CVD) grown multi-walled CNTs (MWCNT) are most economically produced in large quantities but have large numbers of defects reducing

their intrinsic properties. [2, 80, 155, 156] However, CNT properties have been altered to improve critical aspect ratio, inter-wall load transfer, interfacial CNT-polymer stress transfer, dispersion and alignment.[55, 77, 80, 157] There is a large degree of flexibility in tailoring CNTs for optimal composite performance, even if some variables lack complete control. But, the number of variables creates a huge parameter space that is both computationally and experimentally prohibitive to explore. There are four factors to address for mechanical property optimization in CNT-reinforced composites, a) aspect ratio, b) homogeneity of CNT dispersion, c) interfacial CNT-polymer stress transfer and d) CNT alignment. [2, 152] Critical aspect ratio is the minimal length to width ratio required to attain maximum load transfer in the polymer matrix.[42] For aspect ratios less than critical, CNTs will pull out of the matrix rather than fracture. When MWCNTs were functionalized with an epoxide terminated group, the critical aspect ratio was reduced by a factor of three.[80] Functionalization is also used to improve CNT dispersion and tailor the CNT-polymer interfacial bonding.[77, 156-160] In MWCNTs, load transfer was improved with inter-wall bonding.[15, 55, 57] Mechanical properties can be modified by several different variables that do not behave independently. Decoupling and quantifying the effects of individual CNT structural, experimental and manufacturing variables could lead to the ability to tailor mechanical properties.

Development of computational and experimental descriptors and quantitative structure property relationships (QSPRs) are powerful approaches that have not been explored in CNT-reinforced composites. Inspired by their role in drug design and discovery, is it possible to:

1) Identify the most relevant variables in optimizing a material property

2) Train the QSPR with a subset of data to facilitate accurate predictions within the entire parameter space of interest
3) Identify which variables require additional experimental or computational data to accurately capture their effect on the material property.

The purpose of this study is to develop QSPRs predicting Young's modulus and Poisson's ratio. These two elastic properties and the stress-strain curve are fundamental mechanical properties in short fiber composites.[42] Two analyses are performed: 1) vacancy only surface modifications and 2) vacancy plus methyl functionalized surface modifications.

3.2 Computational Methods, Description of CNT Systems

The adaptive intermolecular reactive empirical bond order (AIREBO) potential was used for molecular dynamics (MD) simulations. It extends the second generation of the reactive empirical bond order (REBO) potential to include torsional and pair-wise van der Waals interactions.[146] The REBO potential is well known to accurately describe carbon-carbon and hydrocarbon molecular short range interactions when allowing for bond breaking, bond formation and rehybridization.[18] The cutoff distance within REBO code should be modified to correct for overestimation of the maximum carbon-carbon bond breaking force.[20] The correction was unnecessary for this study because it was focused solely within the linear elastic region of CNT deformations.

Young's modulus, is a measure of stiffness defined as the ratio of axial stress (σ) to axial strain (ε) over ranges of stress in which Hooke's law holds true. 78 single-walled carbon nanotube (SWCNT) test cases were used in the analyses, covering a 10x range of radii, all three chiralities, surface vacancies, surface functionalization, and

multiple chiral angles. Pristine SWCNTs of equal length (100 Å) were created with JCrystalSoft Nanotube Modeler version 1.6.1. The SWCNTs were individually processed with Python scripts to create SWCNTs with four types of surface defects, 1) single vacancy, 2) double vacancy, 3) mixed single and double vacancy and 4) methyl surface functionalized. A 1.5% methyl surface functionalized SWCNT is shown in Figure 3-1.

Figure 3-1: An (8,3) SWCNT with 1.5% randomly distributed methyl surface functionalization is illustrated.

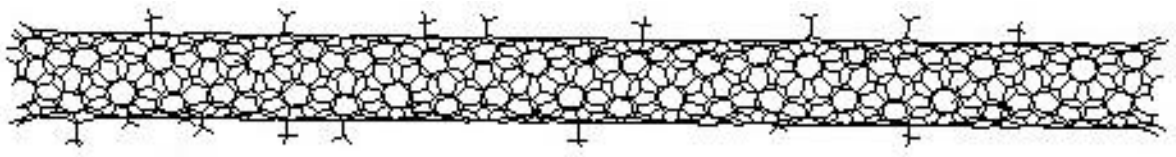

A single vacancy is a single missing atom while a double vacancy is side-by-side missing atoms. Vacancy percent is the amount of the SWCNT surface area covered by the specified type of vacancy. Vacancy positions were randomly selected, at least 4 Å from the CNT end and with at least 4 Å of separation between two vacancies. A vertical double defect had an orientation angle of maximum width greater than 45 degrees and a horizontal double defect had an angle less than or equal to 45 degrees (illustrated in Figure 3-2).

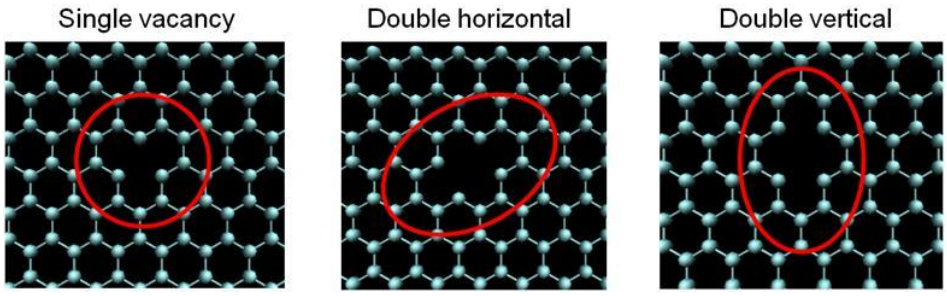

Figure 3-2: The left most figure is a single defect, middle figure is a double horizontal defect and the right figure is a double vertical defect. A horizontal defect has an orientation angle of maximum with less than 45 degrees.

Initial structures were relaxed at 0K for 150 – 250 ps (dependent on the test case) to reach the lowest energy conformation. Large chiral CNTs required the longest relaxation time while the smaller armchair and zigzag CNTs took the least. The coordinate system for the CNT was defined as x and y for the in-plane rings and z for the length-wise axis.

The tensile strain MD simulations had several steps. The outer ring of carbon atoms at both ends of the CNT were each moved 0.1 Å outward, increasing the length of the CNT to 100.2 Å (corresponding to 0.2 / 100 = 0.2% of tensile strain). This structure was fully relaxed at 0K while keeping the carbon atoms at the z-axis extremities fixed in place. Each 0.2% tensile strain relaxation took from 20 ps to 100 ps, based on CNT type, size and total percent strain. Starting from the relaxed structure of the 100.2 Å CNT, the outer ring of carbon atoms on both ends was each moved outward an additional 0.1 Å (total percent strain equals 0.4%) to a total CNT length of 100.4 Å. This iterative process of increasing the strain and relaxing the structure was repeated for a total of 5% strain, well within the ~10% tensile strain failure limit.[60] For each of the 78 SWCNT cases, 26 MD simulations were performed for a total of 2,028 total simulations. A time step of 0.5 fs was used, slower than the fastest process (C-H bond stretching) simulated.[60] To integrate Newton's equations of motion, the velocity Verlet method was implemented.[142] The Berendsen thermostat re-scaled the velocities of the particles to maintain the simulation temperature.[149] At each step, the total structure energy and geometries were collected.

Two methods were used to calculate Young's modulus, via a) the slope of the linear stress-strain curve and b) the second derivative of the strain energy density.

When the results of the two methods were different, the test case was investigated for errors, re-ran with additional relaxation time, etc. While the values are similar, the strain energy density was accepted as most accurate.[67] The linear stress-strain curve method is derived in (32), (33), (34) and (35). Symbols are defined as *Y* as Young's modulus, σ as stress, ε as strain, *F* as force, *A* as cross-sectional area, ΔL as change in length, *L* as current length, L_0 as original relaxed length (no strain) and *E* as strain energy. The cross-sectional area *A* is $2\pi Rh$, *h* equals 0.34 nm (defined as the wall thickness of the CNT) and *R* is the radius.[67] *R* was calculated by averaging the first three carbon ring radii for the fully relaxed structure with no applied strain. Defects cause some distortions in the cylindrical formation, with *R* deviating slightly from the theoretical value.

$$\sigma = Y\varepsilon \tag{32}$$

$$\frac{F}{A} = Y\frac{\Delta L}{L_0} \tag{33}$$

$$\frac{E_{L+\Delta L} - E_L}{\Delta L}\frac{1}{A} = Y\frac{\Delta L}{L_0} \tag{34}$$

$$Y = \left(\frac{E_{L+\Delta L} - E_L}{\Delta L}\right)\frac{L_0}{A\Delta L} \tag{35}$$

Determining Young's modulus via the second derivative of the strain energy density is shown in (36) through (40). *V* is defined as the volume, *k* is the spring constant, *A* is the cross-sectional area, *L* is current length, L_0 is original relaxed length and *E* is strain energy. This method is solved by plotting strain energy versus strain and curve-fitting a second degree polynomial.

$$Y = \frac{1}{V}\frac{\partial^2 E}{\partial \varepsilon^2} \tag{36}$$

$$\int \partial^2 E = \int (VY)\partial \varepsilon^2 \tag{37}$$

$$\int \partial E = VY \int \varepsilon \partial \varepsilon \tag{38}$$

$$E = \frac{1}{2} A L_0 Y \varepsilon^2 \tag{39}$$

$$\frac{2}{AL_0} E = Y \varepsilon^2 \tag{40}$$

Poisson's ratio is the reduction of diameter (or radius) relative to the increase in length as an axial load is applied, shown in (41). For this study, the Poisson's ratio values were calculated at an initial and final strain of 0% and 5%, respectively.

$$Poisson's\ Ratio = -\frac{lateral\ strain}{longitudinal\ strain} = -\frac{(r_f - r_i)/r_i}{(l_f - l_i)/l_i} \tag{41}$$

Poisson's ratio was calculated for multiple middle sections of the CNT, from 30% to 70% in 10% increments. Four of the 78 cases had a standard deviation greater than 0.02, all of which had a radii less than 4 Å and the maximum vacancy surface coverage of 3.0%. To calculate the average radius of the entire section, the center of mass of the CNT section was linearly translated to origin. Individual radii of all carbons were calculated and averaged for the initial and final strains. Length was calculated for the total CNT. Change in total length was evaluated against the delta change for each section and the ratio was verified to be the same.

3.3 Descriptors and Informatics Methods

Chemical descriptors are numerical representations of chemical information. There are many types of descriptors – constitutional, topological, geometric, geometric-

surface, physicochemical and quantum mechanical.[161] Most descriptors to date have been developed for use in drug design and discovery, with a primary focus on small drug-like molecules with molecular weights of less than 500.[162] While there has been some work on materials descriptors[163], the field is immature, especially for CNTs.[164] Much work is needed in the area of descriptor development for nanoparticles, such as to representing waviness, spatial and time distributions of filler particles, as well as multi-scale descriptors.[164] As a first approach, simple and easily interpretable materials-specific constitutional, topological and physicochemical descriptors were used. The single vacancy defect surface area was calculated as a circle with radius equal to a CNT carbon-carbon bond length (1.41 Å).[31] The double defect surface area was calculated as an ellipse with the semi-major and semi-minor axes equal to twice the C-C bond length and the C-C bond length, respectively. These are both first order approximations. Methyl groups have two effects, distortion of the CNT sp^2 surface hybridization and slight electron donating and steric hindrance of the functional group itself. For other types of functional groups, a scale factor would be worth creating and investigating, based on their electron donating / withdrawing and steric hindrance properties. Other future descriptor development could address representation of the manufacturing method (variant of chemical vapor deposition, arc discharge), manufacturing variables, post-processing variables (e.g., length and time of electron irradiation) and creation of experimental descriptors from characterization techniques, such as Raman spectroscopy.[165-167]

Deriving a quantitative structure property relationship (QSPR) involves multiple steps including data collection and preprocessing, data visualization, descriptor

selection, multivariate model development, and model validation.[129] Data collection and preparation was comprised of the MD simulations. While this data set is purely computationally, adding experimental data and recreating the mathematical models would be straightforward with the same procedure. However, the establishment of a vetting process to create a database for polymer nanocomposites has been a challenge to the academic community and reliable experimental data is not easily or readily available.[168] Clusters based on types of defects were manually created and results were analyzed. Descriptor selection is inherent to the mathematical model, partial least squares (PLS), selected to create the QSPR. PLS is a combination of principal component analysis (PCA) and multiple linear regression (MLR).[116] PLS determines a linear regression model by finding a direction vector in the descriptor space that maximizes the explained variance in the response. The premise is to reduce the dimensionality of the original data set via forming a set of latent variables without loss of essential data. PLS works well for large numbers of variables and can handle descriptor collinearity well. Interpretability is a disadvantage of PLS because the latent set of parameters is a projected linear combination of the original variables.[82, 129] Identification of important, stable descriptors is crucial. For small to moderately sized data, a good tool to visualize the effect of individual descriptors is a star plot.[126, 169, 170]

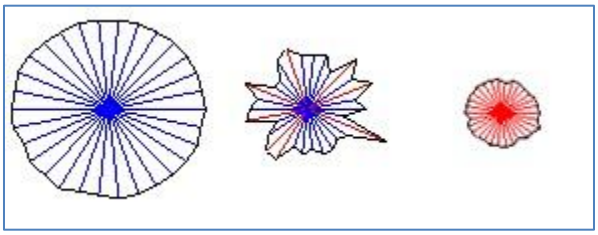

Figure 3-3: Spoke length in star plots is proportional to magnitude while color represents positive or negative correlation. A star plot of equal spoke length and consistent in color represents an important, stable descriptor.

A traditional star plot is composed of a sequence of equi-angular spokes, each spoke representing a variable, with length proportional to magnitude of the variable.[170] Altering the definition of the traditional star plot, the importance of each variable can be evaluated, with each spoke representing an observation.[169] Spoke length is proportional to the importance of the individual variable and the color represents the type of correlation, with red as negative and blue as positive correlation.[169] A star plot of large, uniform spoke length is indicative of a descriptor that is important and stable. The first and last star plot in Figure 3-3 are both stable with the first having a large positive correlation and the last a smaller negative correlation. A star plot with non-uniform spoke lengths or that has both red and blue color implies the descriptor may be ill-represented, fitting noise or describing weights from highly nonlinear models.[169] The middle star plot in Figure 3-3 is an example of a variable that oscillates positively (blue) and negatively (red) as well as with weight (variation in length of spokes). An external test set was used to capture model accuracy and predictive performance and y-scrambling was used to evaluate robustness.[129]

3.4 Results and Discussion

Naming conventions for the SWCNT test cases are explained and the data for all the analyses is provided in table format. Analysis 1 is a vacancy-only test set. The goals are to identify critical descriptors, build accurate and interpretable QSPRs, evaluate the similarities and differences of descriptors for Young's modulus and Poisson's ratio and interpret knowledge conveyed by the models. Analysis 2 is a vacancy and methyl surface functional group test set. The goals are the same as

analysis 1 but the primary objective is to modularly extend the QSPR to represent two different defect types by adding new surface functional group descriptors.

3.4.1 Naming Conventions

The naming convention for the test cases captures the type of CNT, chiral vector, defect type and percent defect loading. For type, 'zz' means 'zig-zag', 'arm' infers 'armchair', and 'chi' represents 'chiral'. The (*n, m*) chiral vector is explicitly stated at the first of the name. Defect types are represented by 'D' for double, 'S' for single, 'DHz' for 'double with the orientation of maximum width less than 45°', 'DVt' for 'double with the orientation of maximum width less than 45°, 'MetS' for 'single methyl surface functional group' and 'Perf' for 'perfect' CNT. The percent loading values for each defect type follows the defect type.

Table 3-1 presents the (10,0) CNT test case as an example.

Table 3-1: Naming conventions for the (10,0) SWCNT are presented.

Test Case Name	Type and Chiral Vector	Defect Type and % Loading
n10m0zz D0.375 S0.75	Zig-zag; (10,0)	Double – 0.375%, Single – 0.75%
n10m0zz DHz0.75	Zig-zag; (10,0)	Double horizontal – 0.75%
n10m0zz DVt1.5	Zig-zag; (10,0)	Double vertical – 1.5%
n10m0zz MetS3.0	Zig-zag; (10,0)	Methyl surface functionalization – 3.0%
n10m0zz Perf	Zig-zag; (10,0)	Perfect or pristine (no defects)
n10m0zz S0.5	Zig-zag; (10,0)	Single – 0.5%
n10m0zz S3.0	Zig-zag; (10,0)	Single – 3.0%

3.4.2 Nanotube Data for Analysis 1 and 2

CNT descriptors are defined in Table 3-2. The data for the analyses is listed in Table 3-3 through Table 3-8. The first two and last two columns are the same in each data table. The first column is the name of the CNT test case while the second indicates whether the test case is used in analysis 1, analysis 2 or both. Young's modulus and Poisson's ratio are the output variables of interest.

Table 3-2: Twenty descriptors and their definitions are provided. Simple descriptors including fragment counts and surface areas were used.

Descriptor Number	Descriptors	Definition
1	Area ($2\pi Rh$) ($Å^2$)	Cross-sectional area of nanotube
2	Chiral Angle	Chiral angle (radians)
3	Average Radius (Å)	Radius of relaxed nanotube as average of first three end rings
4	Theoretical Radius (Å)	Theoretical radius of perfect nanotube
5	Aspect Ratio	Ratio of the length to the diameter
6	% Single Defects	Percentage of single defects
7	% Double Defects	Percentage of double defects
8	% Methyl Groups	Percentage of surface functionalized methyl groups
9	# Missing C's (C_M)	Number of missing due to a vacancy defect
10	# Methyl Groups (M_N)	Number of methyl functional groups
11	# Total C's (C_T)	Total number of carbons in the test case
12	M_N / C_T	Ratio of methyl groups to total number of carbons
13	C_M / C_T	Ratio of missing carbons to total number of carbons
14	# Single Defects	Number of single defect types
15	# Double Defects	Number of double defect types
16	# Non-sp^2 C's (C_{N2})	Number of non-sp^2 hybridized carbons
17	C_{N2} / C_T	Ratio of non-sp^2 hybridized carbons to total number of carbons
18	Surface Area (S_P)	Total surface area of nanotube (uses average radius)
19	Defect Surface Area (S_D)	Surface area of defects
20	S_D / S_P	Ratio of defect area to total surface area

Table 3-3: Data for SWCNT cases 1 – 42 and descriptors 1 – 7 are defined in the following table. Descriptors are listed in columns 3 – 9.

Test Case	Analysis	Area ($2\pi Rh$) ($Å^2$)	Chiral Angle	Average Radius (Å)	Theoretical Radius (Å)	Aspect Ratio	% Single Defects	% Double Defects	Young's Modulus	Poisson's ratio
n17m9chi	1	194.44	0.35	8.97	9.06	11.06	0	0	835	0.212
n17m9chiS05	1	194.48	0.35	8.97	9.06	11.06	0.5	0	794	0.214
n17m9chiS15	1	194.44	0.35	8.97	9.06	11.07	1.5	0	730	0.229
n17m9chiS30	1	194.37	0.35	8.97	9.06	11.12	3	0	652	0.241
n20m0zz	1	168.72	0.00	7.78	7.93	12.46	0	0	947	0.086
n20m0zzS05	1	168.71	0.00	7.78	7.93	12.47	0.5	0	876	0.099
n20m0zzS15	1	168.71	0.00	7.78	7.93	12.49	1.5	0	818	0.135
n20m0zzS30	1	168.52	0.00	7.77	7.93	12.52	3	0	707	0.179
n20m20arm	1	292.35	0.52	13.49	13.73	7.18	0	0	811	0.247
n20m20armS05	1	292.30	0.52	13.48	13.73	7.18	0.5	0	764	0.245
n20m20armS15	1	292.31	0.52	13.48	13.73	7.19	1.5	0	705	0.253
n20m20armS30	1	291.82	0.52	13.46	13.73	7.22	3	0	632	0.266
n27m16chi	1	317.61	0.38	14.65	14.92	6.69	0	0	822	0.225
n27m16chiS05	1	317.69	0.38	14.66	14.92	6.68	0.5	0	790	0.232
n27m16chiS15	1	317.74	0.38	14.66	14.92	6.69	1.5	0	729	0.235
n27m16chiS30	1	317.76	0.38	14.66	14.92	6.71	3	0	643	0.251
n30m0zz	1	252.55	0.00	11.65	11.89	8.32	0	0	944	0.095
n30m0zzS05	1	252.48	0.00	11.65	11.89	8.33	0.5	0	859	0.105
n30m0zzS15	1	252.70	0.00	11.66	11.89	8.34	1.5	0	811	0.137
n30m0zzS30	1	252.58	0.00	11.65	11.89	8.37	3	0	688	0.182
n30m30arm	1	436.80	0.52	20.15	20.59	4.80	0	0	812	0.247
n30m30armS05	1	436.74	0.52	20.15	20.59	4.81	0.5	0	765	0.246
n30m30armS15	1	436.47	0.52	20.14	20.59	4.81	1.5	0	706	0.253
n30m30armS30	1	435.56	0.52	20.09	20.59	4.83	3	0	624	0.245
n8m3chiS30	1,2	83.68	0.27	3.86	3.90	25.72	3	0	714	0.248
n8m3chiS15	1,2	83.76	0.27	3.86	3.90	25.69	1.5	0	820	0.196
n8m3chiS05	1,2	83.79	0.27	3.87	3.90	25.69	0.5	0	873	0.160
n8m3chiPerf	1,2	83.76	0.27	3.86	3.90	25.69	0	0	918	0.158
n8m3chiMetS30	2	83.77	0.27	3.86	3.90	25.69	0	0	906	0.143
n8m3chiMetS15	2	83.77	0.27	3.86	3.90	25.69	0	0	913	0.147
n7m4chiS30	1,2	81.79	0.37	3.77	3.82	28.26	3	0	685	0.269
n7m4chiS15	1,2	81.75	0.37	3.77	3.82	28.27	1.5	0	773	0.237
n7m4chiS05	1,2	81.76	0.37	3.77	3.82	28.27	0.5	0	839	0.197
n7m4chiPerf	1,2	81.75	0.37	3.77	3.82	28.27	0	0	870	0.197
n7m4chiMetS30	2	81.76	0.37	3.77	3.82	28.27	0	0	858	0.192
n7m4chiMetS15	2	81.75	0.37	3.77	3.82	28.27	0	0	864	0.195
n7m4chiDVt15	1,2	81.74	0.37	3.77	3.82	28.31	0	1.5	733	0.321
n7m4chiDVt07	1,2	81.74	0.37	3.77	3.82	28.27	0	0.75	797	0.257
n7m4chiDHz15	1,2	81.79	0.37	3.77	3.82	28.33	0	1.5	692	0.221
n7m4chiDHz07	1,2	81.76	0.37	3.77	3.82	28.27	0	0.75	773	0.215
n7m4chiD075S15	1,2	81.74	0.37	3.77	3.82	28.32	1.5	0.75	713	0.277
n7m4chiD038S075	1,2	81.74	0.37	3.77	3.82	28.30	0.75	0.375	799	0.224

Table 3-4: Data for SWCNT cases 1 – 42 and descriptors 8 – 14 are defined in the following table. Descriptors are listed in columns 3 – 9.

Test Case	Analysis	% Methyl Groups	# Missing C's (C_M)	# Methyl Groups (M_N)	# Total C's (C_T)	M_N / C_T	C_M / C_T	# Single Defects	Young's Modulus	Poisson's ratio
n17m9chi	1	0	0	0	2164	0.0000	0.0000	0	835	0.212
n17m9chiS05	1	0	10	0	2154	0.0000	0.0046	10	794	0.214
n17m9chiS15	1	0	32	0	2132	0.0000	0.0150	32	730	0.229
n17m9chiS30	1	0	64	0	2100	0.0000	0.0305	64	652	0.241
n20m0zz	1	0	0	0	1880	0.0000	0.0000	0	947	0.086
n20m0zzS05	1	0	9	0	1871	0.0000	0.0048	9	876	0.099
n20m0zzS15	1	0	28	0	1852	0.0000	0.0151	28	818	0.135
n20m0zzS30	1	0	56	0	1824	0.0000	0.0307	56	707	0.179
n20m20arm	1	0	0	0	3240	0.0000	0.0000	0	811	0.247
n20m20armS05	1	0	16	0	3224	0.0000	0.0050	16	764	0.245
n20m20armS15	1	0	48	0	3192	0.0000	0.0150	48	705	0.253
n20m20armS30	1	0	97	0	3143	0.0000	0.0309	97	632	0.266
n27m16chi	1	0	0	0	3522	0.0000	0.0000	0	822	0.225
n27m16chiS05	1	0	17	0	3505	0.0000	0.0049	17	790	0.232
n27m16chiS15	1	0	52	0	3470	0.0000	0.0150	52	729	0.235
n27m16chiS30	1	0	105	0	3417	0.0000	0.0307	105	643	0.251
n30m0zz	1	0	0	0	2820	0.0000	0.0000	0	944	0.095
n30m0zzS05	1	0	14	0	2806	0.0000	0.0050	14	859	0.105
n30m0zzS15	1	0	42	0	2778	0.0000	0.0151	42	811	0.137
n30m0zzS30	1	0	84	0	2736	0.0000	0.0307	84	688	0.182
n30m30arm	1	0	0	0	4860	0.0000	0.0000	0	812	0.247
n30m30armS05	1	0	24	0	4836	0.0000	0.0050	24	765	0.246
n30m30armS15	1	0	72	0	4788	0.0000	0.0150	72	706	0.253
n30m30armS30	1	0	145	0	4715	0.0000	0.0308	145	624	0.245
n8m3chiS30	1,2	0	27	0	905	0.0000	0.0298	27	714	0.248
n8m3chiS15	1,2	0	13	0	919	0.0000	0.0141	13	820	0.196
n8m3chiS05	1,2	0	4	0	928	0.0000	0.0043	4	873	0.160
n8m3chiPerf	1,2	0	0	0	932	0.0000	0.0000	0	918	0.158
n8m3chiMetS30	2	3	0	27	959	0.0282	0.0000	0	906	0.143
n8m3chiMetS15	2	1.5	0	13	945	0.0138	0.0000	0	913	0.147
n7m4chiS30	1,2	0	29	0	951	0.0000	0.0305	29	685	0.269
n7m4chiS15	1,2	0	14	0	966	0.0000	0.0145	14	773	0.237
n7m4chiS05	1,2	0	4	0	976	0.0000	0.0041	4	839	0.197
n7m4chiPerf	1,2	0	0	0	980	0.0000	0.0000	0	870	0.197
n7m4chiMetS30	2	3	0	29	1009	0.0287	0.0000	0	858	0.192
n7m4chiMetS15	2	1.5	0	14	994	0.0141	0.0000	0	864	0.195
n7m4chiDVt15	1,2	0	28	0	952	0.0000	0.0294	0	733	0.321
n7m4chiDVt07	1,2	0	14	0	966	0.0000	0.0145	0	797	0.257
n7m4chiDHz15	1,2	0	28	0	952	0.0000	0.0294	0	692	0.221
n7m4chiDHz07	1,2	0	14	0	966	0.0000	0.0145	0	773	0.215
n7m4chiD075S15	1,2	0	26	0	954	0.0000	0.0273	14	713	0.277
n7m4chiD038S075	1,2	0	11	0	969	0.0000	0.0114	7	799	0.224

Table 3-5: Data for SWCNT cases 1 – 42 and descriptors 15 – 20 are defined in the following table. Descriptors are listed in columns 3 – 8.

Test Case	Analysis	# Double Defects	# Non-sp^2 C's (C_{N2})	C_{N2} / C_T	Surface Area (S_P)	Defect Surface Area (S_D)	S_D / S_P	Young's Modulus	Poisson's ratio
n17m9chi	1	0	0	0.0000	5588	0	0.0000	835	0.212
n17m9chiS05	1	0	30	0.0139	5591	63	0.0113	794	0.214
n17m9chiS15	1	0	96	0.0450	5596	203	0.0363	730	0.229
n17m9chiS30	1	0	192	0.0914	5614	406	0.0723	652	0.241
n20m0zz	1	0	0	0.0000	4740	0	0.0000	947	0.086
n20m0zzS05	1	0	27	0.0144	4745	57	0.0120	876	0.099
n20m0zzS15	1	0	84	0.0454	4750	178	0.0374	818	0.135
n20m0zzS30	1	0	168	0.0921	4751	355	0.0748	707	0.179
n20m20arm	1	0	0	0.0000	8196	0	0.0000	811	0.247
n20m20armS05	1	0	48	0.0149	8203	101	0.0124	764	0.245
n20m20armS15	1	0	144	0.0451	8208	304	0.0371	705	0.253
n20m20armS30	1	0	291	0.0926	8215	615	0.0749	632	0.266
n27m16chi	1	0	0	0.0000	9013	0	0.0000	822	0.225
n27m16chiS05	1	0	51	0.0146	9017	108	0.0120	790	0.232
n27m16chiS15	1	0	156	0.0450	9029	330	0.0365	729	0.235
n27m16chiS30	1	0	315	0.0922	9052	666	0.0736	643	0.251
n30m0zz	1	0	0	0.0000	7096	0	0.0000	944	0.095
n30m0zzS05	1	0	42	0.0150	7101	89	0.0125	859	0.105
n30m0zzS15	1	0	126	0.0454	7119	266	0.0374	811	0.137
n30m0zzS30	1	0	252	0.0921	7134	533	0.0747	688	0.182
n30m30arm	1	0	0	0.0000	12240	0	0.0000	812	0.247
n30m30armS05	1	0	72	0.0149	12251	152	0.0124	765	0.246
n30m30armS15	1	0	216	0.0451	12253	457	0.0373	706	0.253
n30m30armS30	1	0	435	0.0923	12251	920	0.0751	624	0.245
n8m3chiS30	1,2	0	81	0.0895	2407	171	0.0712	714	0.248
n8m3chiS15	1,2	0	39	0.0424	2409	82	0.0342	820	0.196
n8m3chiS05	1,2	0	12	0.0129	2410	25	0.0105	873	0.160
n8m3chiPerf	1,2	0	0	0.0000	2409	0	0.0000	918	0.158
n8m3chiMetS30	2	0	27	0.0282	2409	0	0.0000	906	0.143
n8m3chiMetS15	2	0	13	0.0138	2409	0	0.0000	913	0.147
n7m4chiS30	1,2	0	87	0.0915	2526	184	0.0728	685	0.269
n7m4chiS15	1,2	0	42	0.0435	2525	89	0.0352	773	0.237
n7m4chiS05	1,2	0	12	0.0123	2525	25	0.0100	839	0.197
n7m4chiPerf	1,2	0	0	0.0000	2525	0	0.0000	870	0.197
n7m4chiMetS30	2	0	29	0.0287	2525	0	0.0000	858	0.192
n7m4chiMetS15	2	0	14	0.0141	2525	0	0.0000	864	0.195
n7m4chiDVt15	1,2	14	56	0.0588	2528	178	0.0703	733	0.321
n7m4chiDVt07	1,2	7	28	0.0290	2525	89	0.0352	797	0.257
n7m4chiDHz15	1,2	14	56	0.0588	2533	178	0.0701	692	0.221
n7m4chiDHz07	1,2	7	28	0.0290	2525	89	0.0352	773	0.215
n7m4chiD075S15	1,2	6	66	0.0692	2529	165	0.0652	713	0.277
n7m4chiD038S075	1,2	2	29	0.0299	2527	70	0.0276	799	0.224

Table 3-6: Data for SWCNT cases 43 – 78 and descriptors 1 – 7 are defined in the following table. Descriptors are listed in columns 3 – 9.

Test Case	Analysis	Area ($2\pi Rh$) ($Å^2$)	Chiral Angle	Average Radius (Å)	Theoretical Radius (Å)	Aspect Ratio	% Single Defects	% Double Defects	Young's Modulus	Poisson's ratio
n5m5armS30	1,2	73.92	0.52	3.41	3.43	29.57	3	0	835	0.330
n5m5armS15	1,2	73.92	0.52	3.41	3.43	29.57	1.5	0	794	0.252
n5m5armS05	1,2	73.92	0.52	3.41	3.43	29.59	0.5	0	730	0.212
n5m5armPerf	1,2	71.32	0.52	3.29	3.43	30.65	0	0	652	0.208
n5m5armMetS30	2	73.93	0.52	3.41	3.43	29.57	0	0	947	0.207
n5m5armMetS15	2	73.93	0.52	3.41	3.43	29.57	0	0	876	0.208
n5m5armDVt15	1,2	73.90	0.52	3.41	3.43	29.60	0	1.5	818	0.319
n5m5armDVt07	1,2	73.92	0.52	3.41	3.43	29.58	0	0.75	707	0.270
n5m5armDHz15	1,2	73.91	0.52	3.41	3.43	29.75	0	1.5	811	0.225
n5m5armDHz07	1,2	73.92	0.52	3.41	3.43	29.67	0	0.75	764	0.224
n5m5armD075S15	1,2	73.91	0.52	3.41	3.43	29.68	1.5	0.75	705	0.287
n5m5armD038S075	1,2	73.91	0.52	3.41	3.43	29.59	0.75	0.375	632	0.232
n5m0zzS30	1,2	42.61	0.00	1.97	1.98	48.72	3	0	822	0.127
n5m0zzS15	1,2	42.40	0.00	1.96	1.98	48.96	1.5	0	790	0.102
n5m0zzS05	1,2	42.40	0.00	1.96	1.98	49.06	0.5	0	729	0.024
n5m0zzPerf	1,2	46.12	0.00	2.13	1.98	45.01	0	0	643	0.022
n5m0zzMetS30	2	42.44	0.00	1.96	1.98	49.00	0	0	944	0.035
n5m0zzMetS15	2	42.41	0.00	1.96	1.98	49.00	0	0	859	0.030
n10m10armS30	1,2	147.53	0.52	6.81	6.86	14.83	3	0	811	0.296
n10m10armS15	1,2	147.69	0.52	6.81	6.86	14.77	1.5	0	688	0.262
n10m10armS05	1,2	147.66	0.52	6.81	6.86	14.75	0.5	0	812	0.240
n10m10armPerf	1,2	141.46	0.52	6.53	6.86	15.39	0	0	765	0.235
n10m10armMetS30	2	147.59	0.52	6.81	6.86	14.75	0	0	706	0.192
n10m10armMetS15	2	147.75	0.52	6.82	6.86	14.74	0	0	624	0.200
n10m0zzS30	1,2	85.23	0.00	3.93	3.96	24.75	3	0	714	0.197
n10m0zzS15	1,2	85.26	0.00	3.93	3.96	24.62	1.5	0	820	0.136
n10m0zzS05	1,2	85.27	0.00	3.93	3.96	24.65	0.5	0	873	0.075
n10m0zzPerf	1,2	88.93	0.00	4.10	3.96	23.60	0	0	918	0.067
n10m0zzMetS30	2	85.19	0.00	3.93	3.96	24.64	0	0	906	0.077
n10m0zzMetS15	2	85.27	0.00	3.93	3.96	24.62	0	0	913	0.068
n10m0zzDVt15	1,2	85.21	0.00	3.93	3.96	24.77	0	1.5	685	0.154
n10m0zzDVt07	1,2	85.27	0.00	3.93	3.96	24.68	0	0.75	773	0.120
n10m0zzDHz15	1,2	85.26	0.00	3.93	3.96	24.71	0	1.5	839	0.192
n10m0zzDHz07	1,2	85.27	0.00	3.93	3.96	24.67	0	0.75	870	0.144
n10m0zzD075S15	1,2	85.26	0.00	3.93	3.96	24.72	1.5	0.75	858	0.179
n10m0zzD038S075	1,2	85.26	0.00	3.93	3.96	24.69	0.75	0.375	864	0.106

Table 3-7: Data for SWCNT cases 43 – 78 and descriptors 8 – 14 are defined in the following table. Descriptors are listed in columns 3 – 9.

Test Case	Analysis	% Methyl Groups	# Missing C's (C_M)	# Methyl Groups (M_N)	# Total C's (C_T)	M_N / C_T	C_M / C_T	# Single Defects	Young's Modulus	Poisson's ratio
n5m5armS30	1,2	0	25	0	815	0.0000	0.0307	25	648	0.330
n5m5armS15	1,2	0	12	0	828	0.0000	0.0145	12	735	0.252
n5m5armS05	1,2	0	4	0	836	0.0000	0.0048	4	796	0.212
n5m5armPerf	1,2	0	0	0	840	0.0000	0.0000	0	857	0.208
n5m5armMetS30	2	3	0	25	865	0.0289	0.0000	0	820	0.207
n5m5armMetS15	2	1.5	0	12	852	0.0141	0.0000	0	823	0.208
n5m5armDVt15	1,2	0	24	0	816	0.0000	0.0294	0	687	0.319
n5m5armDVt07	1,2	0	12	0	828	0.0000	0.0145	0	755	0.270
n5m5armDHz15	1,2	0	24	0	816	0.0000	0.0294	0	658	0.225
n5m5armDHz07	1,2	0	12	0	828	0.0000	0.0145	0	742	0.224
n5m5armD075S15	1,2	0	22	0	818	0.0000	0.0269	12	676	0.287
n5m5armD038S075	1,2	0	10	0	830	0.0000	0.0120	6	757	0.232
n5m0zzS30	1,2	0	14	0	456	0.0000	0.0307	14	695	0.127
n5m0zzS15	1,2	0	7	0	463	0.0000	0.0151	7	837	0.102
n5m0zzS05	1,2	0	2	0	468	0.0000	0.0043	2	890	0.024
n5m0zzPerf	1,2	0	0	0	470	0.0000	0.0000	0	874	0.022
n5m0zzMetS30	2	3	0	14	484	0.0289	0.0000	0	867	0.035
n5m0zzMetS15	2	1.5	0	7	477	0.0147	0.0000	0	991	0.030
n10m10armS30	1,2	0	50	0	1630	0.0000	0.0307	50	643	0.296
n10m10armS15	1,2	0	25	0	1655	0.0000	0.0151	25	721	0.262
n10m10armS05	1,2	0	8	0	1672	0.0000	0.0048	8	784	0.240
n10m10armPerf	1,2	0	0	0	1680	0.0000	0.0000	0	850	0.235
n10m10armMetS30	2	3	0	50	1730	0.0289	0.0000	0	801	0.192
n10m10armMetS15	2	1.5	0	25	1705	0.0147	0.0000	0	807	0.200
n10m0zzS30	1,2	0	28	0	912	0.0000	0.0307	28	727	0.197
n10m0zzS15	1,2	0	14	0	926	0.0000	0.0151	14	844	0.136
n10m0zzS05	1,2	0	4	0	936	0.0000	0.0043	4	906	0.075
n10m0zzPerf	1,2	0	0	0	940	0.0000	0.0000	0	910	0.067
n10m0zzMetS30	2	3	0	28	968	0.0289	0.0000	0	932	0.077
n10m0zzMetS15	2	1.5	0	14	954	0.0147	0.0000	0	944	0.068
n10m0zzDVt15	1,2	0	28	0	912	0.0000	0.0307	0	828	0.154
n10m0zzDVt07	1,2	0	14	0	926	0.0000	0.0151	0	893	0.120
n10m0zzDHz15	1,2	0	28	0	912	0.0000	0.0307	0	728	0.192
n10m0zzDHz07	1,2	0	14	0	926	0.0000	0.0151	0	836	0.144
n10m0zzD075S15	1,2	0	26	0	914	0.0000	0.0284	14	768	0.179
n10m0zzD038S075	1,2	0	11	0	929	0.0000	0.0118	7	887	0.106

Table 3-8: Data for SWCNT cases 43 – 78 and descriptors 15 – 20 are defined in the following table. Descriptors are listed in columns 3 – 8.

Test Case	Analysis	# Double Defects	# Non-sp^2 C's (C_{N2})	C_{N2} / C_T	Surface Area (S_P)	Defect Surface Area (S_D)	S_D / S_P	Young's Modulus	Poisson's ratio
n5m5armS30	1,2	0	75	0.0920	2159	159	0.0734	648	0.330
n5m5armS15	1,2	0	36	0.0435	2159	76	0.0353	735	0.252
n5m5armS05	1,2	0	12	0.0144	2161	25	0.0117	796	0.212
n5m5armPerf	1,2	0	0	0.0000	2083	0	0.0000	857	0.208
n5m5armMetS30	2	0	25	0.0289	2160	0	0.0000	820	0.207
n5m5armMetS15	2	0	12	0.0141	2160	0	0.0000	823	0.208
n5m5armDVt15	1,2	12	48	0.0588	2160	152	0.0705	687	0.319
n5m5armDVt07	1,2	6	24	0.0290	2160	76	0.0352	755	0.270
n5m5armDHz15	1,2	12	48	0.0588	2172	152	0.0701	658	0.225
n5m5armDHz07	1,2	6	24	0.0290	2167	76	0.0351	742	0.224
n5m5armD075S15	1,2	5	56	0.0685	2167	140	0.0644	676	0.287
n5m5armD038S075	1,2	2	26	0.0313	2161	63	0.0294	757	0.232
n5m0zzS30	1,2	0	42	0.0921	1182	89	0.0751	695	0.127
n5m0zzS15	1,2	0	21	0.0454	1176	44	0.0378	837	0.102
n5m0zzS05	1,2	0	6	0.0128	1179	13	0.0108	890	0.024
n5m0zzPerf	1,2	0	0	0.0000	1279	0	0.0000	874	0.022
n5m0zzMetS30	2	0	14	0.0289	1179	0	0.0000	867	0.035
n5m0zzMetS15	2	0	7	0.0147	1178	0	0.0000	991	0.030
n10m10armS30	1,2	0	150	0.0920	4314	317	0.0735	643	0.296
n10m10armS15	1,2	0	75	0.0453	4306	159	0.0368	721	0.262
n10m10armS05	1,2	0	24	0.0144	4299	51	0.0118	784	0.240
n10m10armPerf	1,2	0	0	0.0000	4116	0	0.0000	850	0.235
n10m10armMetS30	2	0	50	0.0289	4295	0	0.0000	801	0.192
n10m10armMetS15	2	0	25	0.0147	4299	0	0.0000	807	0.200
n10m0zzS30	1,2	0	84	0.0921	2403	178	0.0739	727	0.197
n10m0zzS15	1,2	0	42	0.0454	2391	89	0.0371	844	0.136
n10m0zzS05	1,2	0	12	0.0128	2395	25	0.0106	906	0.075
n10m0zzPerf	1,2	0	0	0.0000	2494	0	0.0000	910	0.067
n10m0zzMetS30	2	0	28	0.0289	2390	0	0.0000	932	0.077
n10m0zzMetS15	2	0	14	0.0147	2392	0	0.0000	944	0.068
n10m0zzDVt15	1,2	14	56	0.0614	2403	178	0.0739	828	0.154
n10m0zzDVt07	1,2	7	28	0.0302	2398	89	0.0370	893	0.120
n10m0zzDHz15	1,2	14	56	0.0614	2401	178	0.0740	728	0.192
n10m0zzDHz07	1,2	7	28	0.0302	2397	89	0.0371	836	0.144
n10m0zzD075S15	1,2	6	66	0.0722	2402	165	0.0687	768	0.179
n10m0zzD038S075	1,2	2	29	0.0312	2398	70	0.0291	887	0.106

Young's modulus values vary widely in the literature. Young's modulus was calculated as 1.47, 1.10 and 0.726 TPa for (10,0), (8,4) and (10,10) SWCNTs, respectively.[50] It was experimental calculated as 0.9 to 1.9 TPa[53] while one *ab initio* result yielded 0.5 to 1.1 TPa (radii between 3 and 7 Å).[46] Select MD results range from 0.311 to 1.107.[151, 171-174] Several studies have addressed vacancy-laden CNTs, capturing percent reduction in Young's modulus from virtually independent to 15%.[175-178] Reasons for variation include dependence on chirality and diameter, differing values used for the wall thickness[47], variation in procedural methods[48] and variation and of computational methods. With respect to vacancies, there is much variation in the number, type and distribution. The data set for this study is generated by a single computational method, employs the same procedural method across all cases, assumes a wall thickness of 0.34 nm[48], and evaluates effects of CNT chirality and diameter, vacancy type, size and distribution. Most of the reasons for variation among the literature are negated in this study (this is not to say this is the most accurate method but simply consistent).

Values for Poisson's ratio also have a large distribution in the literature. One DFT study predicted values between 0.11 and 0.19[46] while two MD results calculated 0.13 – 0.19[48, 179, 180] and another 0.32-0.36.[177] Analytical models proposed values of 0.21 and 0.277-0.280.[45, 181] Tight-binding MD found Poisson's ratios of 0.285 and 0.287.[174, 182] Other results include an *ab initio* rendered 0.32[50] and a finite element prediction of 0.31 – 0.35.[183] Reasons for variation are similar to above – different computational methods, dissimilar procedural approaches, variation in CNT morphologies, etc.

3.4.3 Analysis 1: Developing a Vacancy Only QSPR

The goals are to build accurate and interpretable QSPRs with a few critical descriptors, evaluate the similarities and differences of descriptors for Young's modulus and Poisson's ratio and interpret knowledge conveyed by the models. The primary goal is to identify critical descriptors, especially those that can be directly linked to experimental measurements.

3.4.3.1 Young's Modulus

From experimental and computational studies, it is well known that vacancies lead to a decrease in Young's Modulus, consistent with the data presented.[19, 65, 175, 178] Young's modulus was plotted against the number of missing carbon atoms. A quadratic fit yields a coefficient of determination (R^2) value equal to 0.63. While the number of vacancies does influence Young's modulus, it alone is insufficient to model change in Young's modulus.

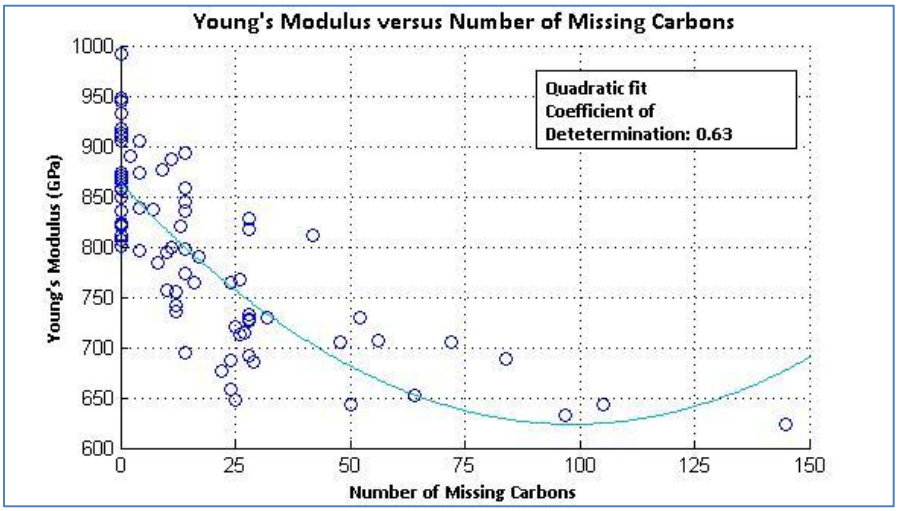

Figure 3-4: Young's modulus versus the number of missing carbon atoms shows a quadratic fit with a coefficient of determination 0.63.

The data was arranged into 5 sets, based on radius. Partitioning in this manner allows a quick isolation of radius, analytically shown to have an effect at less than approximately 2 nm, while allowing for a random distribution of all other variables. [184, 185] Results of a PLS model in parallel with star plot analysis and manual clustering identified the most important type of feature or specific feature for all data sets. 80% of the data was used to train the model and 20% used to test. R^2_{Train} and R^2_{Test} provided a measure of accuracy and predictive power.[129, 130] Y-scrambling (not shown) tested model robustness.[129] Results of the five models are presented in Table 3-9.

Table 3-9: Data for analysis 1 for Young's modulus is divided into 5 sets to isolate size effects. All descriptors were provided as input and the selected descriptors for each model were split across three feature types.

Data Set Description	**R^2_{Train} R^2_{Test}**	**Categories of Feature Types**		
		Size	**Chiral Angle**	**Counts, % Defects**
Test set 1; r = 2 – 7 Å	0.93 0.75	Surface Area (S_P)	Chiral Angle	C_{N2} / C_T % Double Defects
Test set 2; r = 3.5 – 7 Å	0.95 0.74	Surface Area (S_P)	Chiral Angle	# Single Defects C_{N2} / C_T % Double Defects
Test set 3; r = 7 – 21 Å	0.97 0.98	Surface Area (S_P)	Chiral Angle	C_M / C_T
Test set 4; r = 3.5 –21 Å	0.94 0.92	Surface Area (S_P)	Chiral Angle	C_{N2} / C_T % Double Defects
Test set 5; r = 2 – 21 Å	0.95 0.76	Surface Area (S_P)	Chiral Angle	C_{N2} / C_T % Double Defects

The primary goal of this analysis is to identify critical descriptors. Using all descriptors, the first step was identifying descriptor categories using PLS, star plots and manual clustering. Each model had three categories, a) measure of CNT size, b) chiral angle and c) measure of number or size of defects. The defect category had multiple descriptors. The ratio of non-sp^2 hybridized carbons to the total number of carbon (C_{N2} /

C_T) appears the most. This descriptor captures both the size and type of the surface vacancy. A reasonable approach to reduce the number of critical descriptors and improve model interpretability would be to only include C_{N2} / C_T in the defect category. If Young's modulus were independent of radii, the R^2_{Train} and R^2_{Test} would be approximately the same across all test sets. By comparing test sets 1 and 3 (as well as test sets 4 and 5), it is clear that radius has an effect, at least at smaller values. To improve model interpretability, surface area was replaced with radii in the size category. Surface area was proportional to radius since length was held constant. After multiple descriptor selection and model building runs (selecting different single descriptors per category), a second set of QSPRs were developed and presented in Table 3-10.

Table 3-10: Data for analysis 1 for Young's modulus is divided into 5 sets to isolate size effects. A single descriptor per feature type was provided as input.

Data Set Description	**R^2_{Train} R^2_{Test}**	**Categories of Feature Types**		
		Size	**Chiral Angle**	**Counts, % Defects**
Test set 1; r = 2 – 7 Å	0.93 0.66	Theoretical radius	Chiral Angle	C_{N2} / C_T
Test set 2; r = 3.5 – 7 Å	0.95 0.65	Theoretical radius	Chiral Angle	C_{N2} / C_T
Test set 3; r = 7 – 21 Å	0.99 0.99	Theoretical radius	Chiral Angle	C_{N2} / C_T
Test set 4; r = 3.5 –21 Å	0.95 0.89	Theoretical radius	Chiral Angle	C_{N2} / C_T
Test set 5; r = 2 – 21 Å	0.94 0.88	Theoretical radius	Chiral Angle	C_{N2} / C_T

The effect of down-selecting to one descriptor per category can be evaluated by comparing R^2_{Train} and R^2_{Test} values. Compared to Table 3-9, the values are very similar, indicating only a slight loss of accuracy and predictive ability. But, the reduced descriptor set yields an increase in model interpretability. To verify the descriptors are well-represented, star plots are shown in Figure 3-5. The descriptors are of uniform

spoke length and color per test case. However, chiral angle appears to have an inconsistent behavior, with a positive correlation for both test set 1 (r = 2 to 7 Å) and test set 3 (r = 7 to 21 Å) and a negative correlation for test set 5 (r= 2 to 21 Å). There are two factors in this seemingly inconsistent behavior.

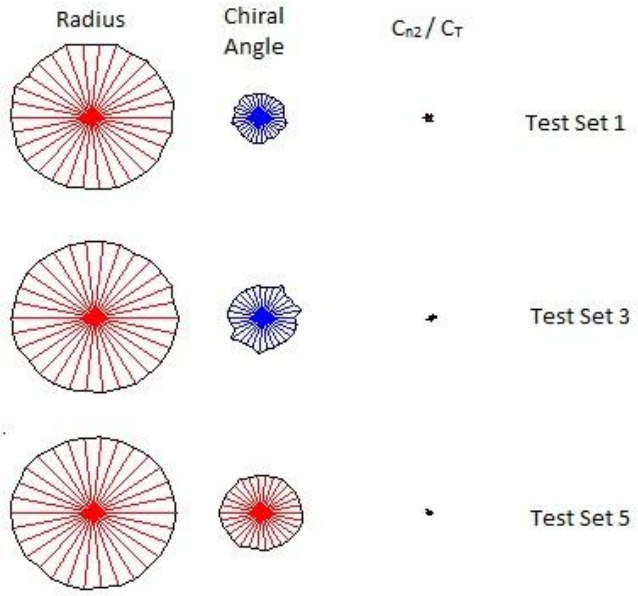

Figure 3-5: Young's modulus star plots with three most important descriptors for vacancy-only analysis.

First, the mechanism to attain the lowest energy state as a function of chirality and radius does vary. Resilience of CNTs to changes in Young's modulus will be discussed shortly. Second, C_{N2} / C_T falls within the size and defect categories – radii and C_{N2} / C_T are not orthogonal variables. It is very likely the PLS model simply associated more of the explained variance in the response with the radius in one model and C_{N2} / C_T in the other. Star plots are used to look at consistency in data, uniform spoke length and color. The least squares constraint can easily mask an otherwise straightforward interpretation, especially for non-orthogonal features. Direct interpretation of correlation from star plots is generally avoided. Given that C_{N2} / C_T can

be used to represent the size category, one final set of models was developed using only chiral angle and C_{N2} / C_T. The results (Table 3-11) showed almost no decrease in QSPR accuracy and predictivity with respect to the previous set. Size can be fully represented in the density descriptor C_{N2} / C_T, eliminating the need to experimentally characterize the radius.

Table 3-11: Young's modulus vacancy-only minimal feature selection confirms size is not required for an accurate QSPR.

Data Set Description	R^2_{Train} R^2_{Test}	**Categories of Feature Types**		
		Size	**Chiral Angle**	**Counts, % Defects**
Test set 1; r = 2 – 7 Å	0.91 0.67		Chiral Angle	C_{N2} / C_T
Test set 2; r = 3.5 – 7 Å	0.95 0.65		Chiral Angle	C_{N2} / C_T
Test set 3; r = 7 – 21 Å	0.97 0.98		Chiral Angle	C_{N2} / C_T
Test set 4; r = 3.5 –21 Å	0.92 0.88		Chiral Angle	C_{N2} / C_T
Test set 5; r = 2 – 21 Å	0.93 0.88		Chiral Angle	C_{N2} / C_T

Another goal of the analysis is to use the models and critical features to extract knowledge. A linear analysis of chiral angle, versus Young's modulus, in Figure 3-6, quantifies the effect of Young's modulus on chiral angle. Since it was shown that Young's modulus was not independent of radii for these test sets, three radii intervals were evaluated, less than 4 Å, 4 to 12 Å, and 12 to 21 Å.

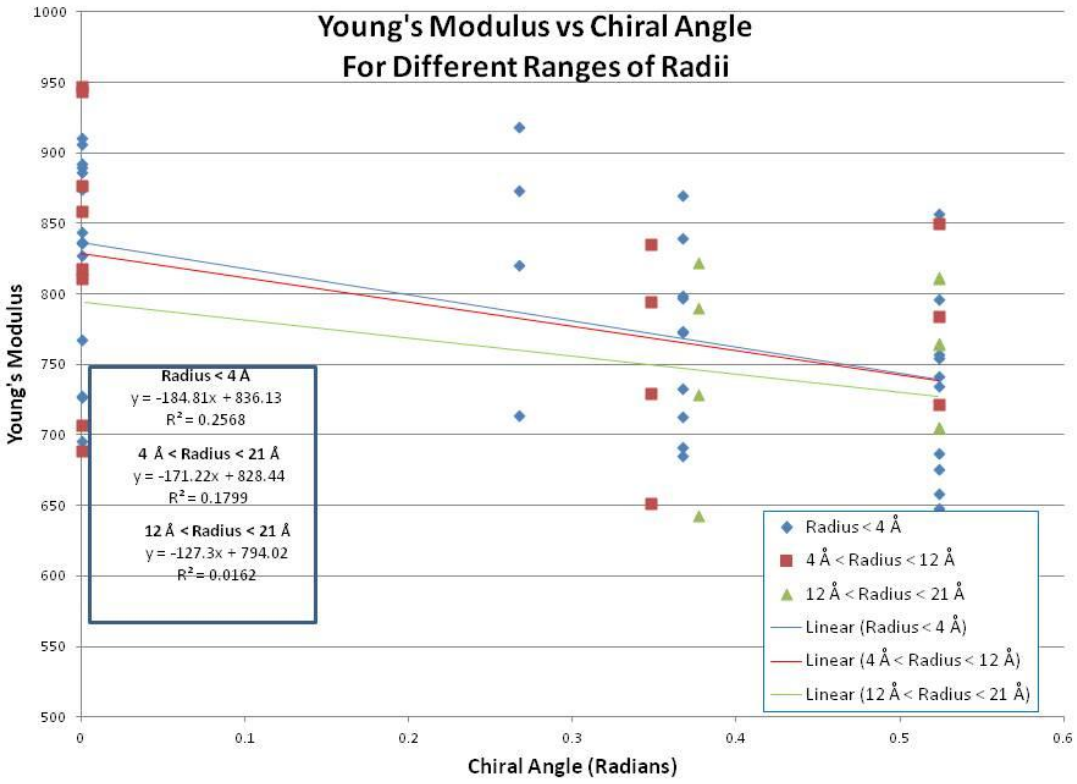

Figure 3-6: For radii greater than 1-2 nm, Young's modulus is virtually independent of chiral angle. The correlation coefficient for radii between 1-2 nm is ~0.0162 whereas for radii less than 0.4 nm, it is 0.2568.

The magnitude of the slope decreases as radii increases, confirming a lessening effect of chiral angle for larger radii. For radii less than 4 Å, the correlation coefficient is 0.2568. For radii from 12 to 21 Å, the correlation coefficient is 0.0162, rendering Young's modulus independent of chiral angle. The effect of chiral angle decreases by a factor of 16 between the two radii ranges.

Reduction of Young's modulus due to vacancies has been shown to be less significant for larger diameter CNTs.[178] Graphing C_{N2} / C_T (graph not shown) quantifies this effect. The R^2 values are shown in Table 3-12. Summation of the correlation coefficients provides a measure of how accurately chiral angle and C_{N2} / C_T can predict

Young's modulus. For the smaller radii CNTs (less than 4 Å), the two descriptors capture 90.4% of the variance. For the larger CNTs (radii equals 12 to 21 Å), the two descriptors capture 99% of the variance. C_{N2} / C_T is the dominant variable across all radii ranges and represents 97.4% for radii greater than 12 Å. C_{N2} / C_T alone is sufficient for accurately modeling Young's modulus based on these results.

Table 3-12: For all radii, C_{N2} / C_T captures the majority of the information needed to accurately predict Young's modulus.

Radii Range	Chiral Angle	C_{N2} / C_T	Total Percentage
R < 4 Å	0.2568	0.6473	90.4 %
4 Å < R < 12 Å	0.1799	0.7732	95.3 %
12 Å < R < 21 Å	0.0162	0.9738	99.0 %

Another question of interest is the resilience of larger CNTs as percentage vacancy is increased. In this study, resilience is defined as the amount of change from the baseline and is evaluated by the ratio of the defected CNT mechanical property to the pristine CNT mechanical property. Table 3-13 evaluates the delta Young's modulus over a range of diameters for armchair, zig-zag and chiral CNTs.

Table 3-13: Change in Young's modulus as percentage surface defects increases is presented. For armchair as the radius increases, the delta from the pristine Young's modulus slightly decreases, indicating larger armchair CNTs are more resilient. For zig-zag with an increase in radii, the deviation from the pristine Young's modulus slightly increases, indicated larger CNTs are less resilient.

CNT Type	Chiral Angle (deg)	Theo. Radius (Å)	$YM_{0.0\%}$	$YM_{0.5\%}$	$YM_{1.5\%}$	$YM_{3.0\%}$	$YM_{0.5\%}/YM_{0.0\%}$	$YM_{1.5\%}/YM_{0.0\%}$	$YM_{3.0\%}/YM_{0.0\%}$
(5,5)	0	3.4	856.5	796.1	734.9	647.6	0.929	0.858	0.756
(10,10)	0	6.9	850.2	784.1	721.4	642.7	0.922	0.849	0.756
(20,20)	0	13.7	811.0	764.4	704.8	631.9	0.943	0.869	0.779
(30,30)	0	20.6	811.8	765.1	705.5	624.4	0.942	0.869	0.769
(5,0)	30	2.0	874.1	889.5	836.9	695.4	1.018	0.957	0.796
(10,0)	30	4.0	910.4	906.4	844.0	726.5	0.996	0.927	0.798
(20,0)	30	7.9	947.2	876.3	817.7	706.8	0.925	0.863	0.746
(30,0)	30	11.9	943.7	858.6	810.9	688.2	0.910	0.859	0.729
(7,4)	21.1	3.8	869.6	839.4	772.9	685.1	0.965	0.889	0.788
(8,3)	15.3	3.9	918.1	873.3	820.3	713.6	0.951	0.893	0.777
(17,9)	19.9	9.1	834.8	794.3	729.7	651.7	0.951	0.874	0.781
(27,16)	21.6	14.9	822.4	789.9	728.9	642.9	0.960	0.886	0.782

For armchair CNTs, the ratio of the defected CNT to the pristine CNT is increased for all surface vacancy percentages. Thus, for larger armchair CNTs, the delta Young's modulus decreases slightly. This means that larger armchair CNTs are slightly more resilient to surface vacancies than smaller armchair CNTs. The opposite is observed for zig-zag. As radii increases, the ratio of the defected CNT to the pristine CNT is decreased. $YM_{1.5\%}/ YM_{0.0\%}$ decreases from 95.7% to 85.9%. This means that the larger diameter (30,0) CNT is approximately 10% less resilient to a 1.5% surface vacancy area than the smaller (5,0) CNT. The delta Young's modulus for chiral CNTs is approximately the same for all radii. One possible qualitative explanation is the following. For all CNTs, the trigonal planar sp^2 structure is highly strained for smaller diameters due to the curvature. Zig-zag CNTs are already in a low energy conformation with respect to an axial tension; zig-zag bond orientation increases the stiffness.[48, 186] For armchair, the energy barrier to relieve strain is less for smaller CNTs because a

bond rotation to stabilize the vacancy is less (more reactive CNTs) and a bond rotation also aligns the bonds with the axial tension (lower energy conformation). At larger diameters, the bond rotation barrier to stabilize the vacancy is increased because the structure is not as strained. Thus, Young's modulus is slightly more resilient to change to increased vacancy surface area for larger armchair CNTs than smaller. For zig-zag, the increased reactivity of the smaller CNT makes a bond rotation more likely; however, this increases the energy barrier to alleviate strain because it was originally in a low energy state. For larger diameters, the bond rotation is less likely (structure isn't as strained), which lowers the energy barrier to alleviate strain. The intermediate case is chiral, which exhibits no change and is consistent with the results.

3.4.3.2 Poisson's Ratio

Poisson's ratio varies widely in the literature based on chirality and surface defects. A recent paper reported finding variations from 0.06 to 1.414 and concluded accurate prediction Poisson's ratio for single walled CNTs is still an unsolved issue.[187] Poisson's ratio was taken from 0-5% delta strain shown in Table 3-14.

Table 3-14: Poisson's ratio is measured for middle-centered CNT sections from 30% to 70% of the original length. Delta strain is from 0 to 5%.

Test Case	Chiral Angle (Rad)	Radius (Å)	% Vacancy	Middle 30%	Middle 40%	Middle 50%	Middle 60%	Middle 70%	Std Dev
n5m0zzPerf	0	1.96	0.0	0.02	0.02	0.02	0.02	0.02	0.00
n10m10armPerf	0.52	6.81	0.0	0.23	0.23	0.23	0.23	0.23	0.00
n7m4chiPerf	0.37	3.77	0.0	0.20	0.20	0.20	0.20	0.20	0.00
n20m20armS05	0.52	13.48	0.5	0.25	0.24	0.25	0.25	0.25	0.00
n8m3chiS05	0.27	3.86	0.5	0.15	0.15	0.16	0.17	0.17	0.01
n20m20armS30	0.52	13.48	3.0	0.27	0.27	0.26	0.27	0.27	0.01
n7m4chiDHz15	0.37	3.77	3.0	0.23	0.22	0.21	0.22	0.23	0.02
n20m0zzS30	0	7.78	3.0	0.18	0.17	0.17	0.19	0.18	0.02
n10m0zzDVt15	0	3.93	3.0	0.16	0.15	0.15	0.16	0.15	0.06

Before identifying critical descriptors, the validity of the calculated Poisson's ratio values is discussed. There is almost no variation in Poisson's ratio for perfect CNTs of

all chiralities, which confirms the lateral contraction is linear throughout the CNT and should be independent of the CNT section size used for calculations. The largest variance across sections is observed for maximal percentage surfaces of the smaller CNTs. Variation in radial change is due to the presence of a defect and over-counting the effect of a vacancy is more likely in the smaller sections. It is important to consider a large section of the CNT for accurate calculations. Using 30 – 70% of the CNT for radial calculations rendered near constant results and the average of those values was selected as the recorded Poisson's ratio.

Figure 3-7 shows that Poisson's ratio has a strong dependence on chirality, with a coefficient of determination of 0.64. However, it alone is insufficient to provide an accurate model for the behavior of Poisson's ratio.

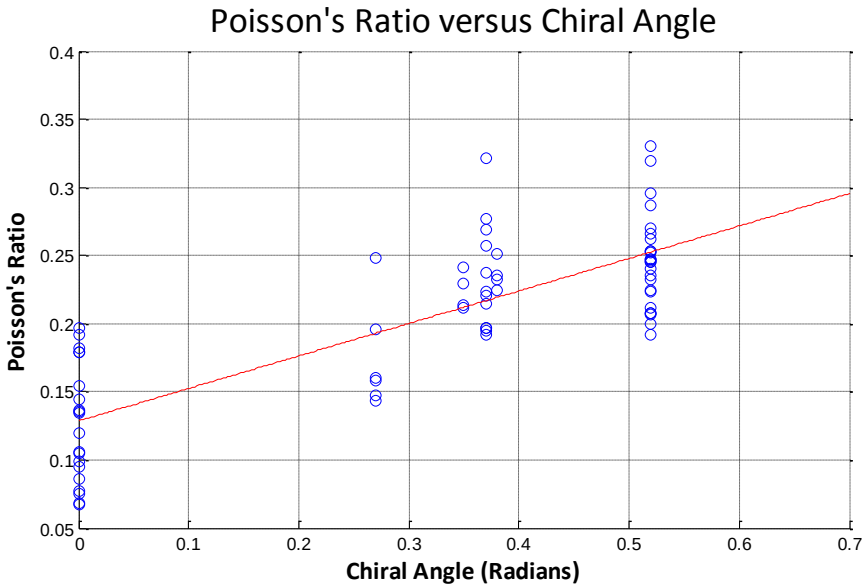

Figure 3-7: Poisson's ratio has a strong dependence on chirality.

Effect of surface vacancies on Poisson's ratio was evaluated for all three chiral types (radii between 12 and 15 Å). Over this range of radii, Poisson's ratio is only slightly dependent on chirality for armchair and chiral CNTs but the value changes by a

factor of 2 for zig-zag. This result is consistent with the findings in the previous section; zig-zag CNTs are less resilient to changes from pristine structure than either armchair or chiral.

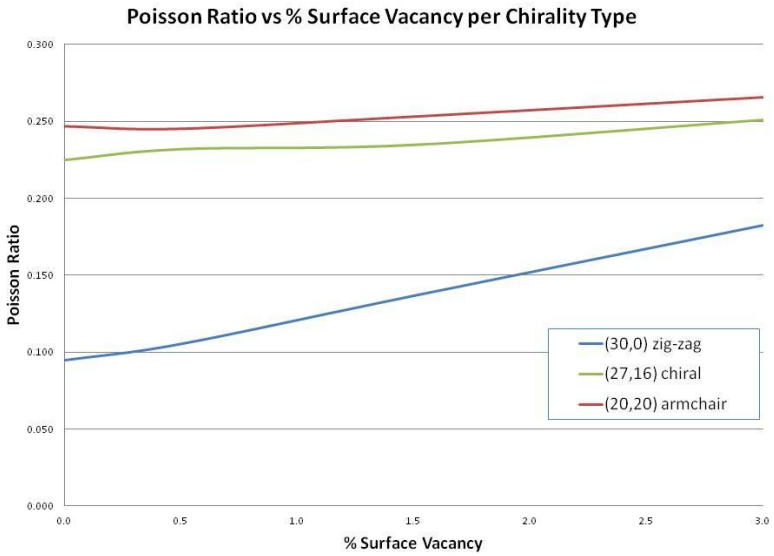

Figure 3-8: Poisson's ratio for both a (27,16) chiral and (20,20) armchair CNT is fairly constant as percentage surface defects increases from 0% to 3%. However, for the (30,0) zig-zag CNT, the value increases by a factor of 2.

As before, the data was arranged into 5 radii-partitioned sets to quickly isolate size-dependent behavior. For all cases, 80% of the data was used as a training set and the remaining 20% was used as an external test set. R^2_{Train} and R^2_{Test} provided a measure of accuracy and predictive power.[129, 130] Y-scrambling (not shown) tested model robustness.[129] Results of the five models are presented in Table 3-9.

Table 3-15: Data for analysis 1 (vacancy only) for Poisson's ratio is divided into 5 sets to isolate size effects. All descriptors were provided as input and the selected descriptors for each model were split across three feature types.

Data Set Description	R^2_{Train} R^2_{Test}	**Categories of Feature Types**		
		Size	**Chiral Angle**	**Counts, % Defects**
Test set 1; r = 2 – 7 Å	0.89 0.91	Surface Area (S_P)	Chiral Angle	C_M % Double Defects % Single Defects
Test set 2; r = 3.5 – 7 Å	0.87 0.87	Surface Area (S_P)	Chiral Angle	C_M / C_T % Double Defects
Test set 3; r = 7 – 21 Å	0.93 0.79	Surface Area (S_P)	Chiral Angle	C_M
Test set 4; r = 3.5 –21 Å	0.88 0.85	Surface Area (S_P)	Chiral Angle	C_M / C_T % Double Defects % Single Defects
Test set 5; r = 2 – 21 Å	0.88 0.91	Surface Area (S_P)	Chiral Angle	% Single Defects % Double Defects C_{N2} / C_T

As with Young's modulus, the primary goal is to identify critical descriptors. Using all the descriptors, the first step was to sort selected descriptors into categories. Each model had the same three categories as Young's modulus, a) measure of CNT size, b) chiral angle and c) measure of number or size of defects. For Poisson's ratio, number of missing carbons to total number of carbons C_M / C_T appeared the most frequently. Further, the other descriptors selected are percentage defects and not the number of defects. This means Poisson's ratio is more sensitive to the overall size of the defect whereas Young's modulus was sensitive to both size and type (C_{N2} / C_T). The accuracy and predictive measures R^2_{Train} and R^2_{Test} were relatively consistent across all data sets. Comparing test set 3 to test set 1 indicates a slight dependence on size for Poisson's ratio.

A reasonable approach to reduce the number of critical descriptors and improve model interpretability would be to only include C_M / C_T in the defect category. Results are presented in Table 3-16.

Table 3-16: Analysis 1 (vacancy only) for Poisson's ratio with a single descriptor per feature type provided as input has no decrement to accuracy and interpretability is improved.

Data Set Description	R^2_{Train} R^2_{Test}	**Categories of Feature Types**		
		Size	**Chiral Angle**	**Counts, % Defects**
Test set 1; r = 2 – 7 Å	0.93 0.81	Surface Area (S_P)	Chiral Angle	C_M / C_T
Test set 2; r = 3.5 – 7 Å	0.87 0.86	Surface Area (S_P)	Chiral Angle	C_M / C_T
Test set 3; r = 7 – 21 Å	0.96 0.83	Surface Area (S_P)	Chiral Angle	C_M / C_T
Test set 4; r = 3.5 –21 Å	0.87 0.89	Surface Area (S_P)	Chiral Angle	C_M / C_T
Test set 5; r = 2 – 21 Å	0.88 0.83	Surface Area (S_P)	Chiral Angle	C_M / C_T

Across all test sets, compared to the full descriptor set, the QSPRs were the same or better in terms of accuracy and predictive power and interpretability was greatly improved. Comparing test set 3 to test set 1 again shows a slight improvement in modeling Poisson's ratio at larger radii.

To compare the similarity between descriptors for models of Young's modulus and Poisson's ratio, three individual descriptors were used, C_{N2} / C_T, C_M / C_T, and S_D / S_P (ratio of defected surface area to pristine surface area) to represent the defect category. C_{N2} / C_T was the critical descriptor for Young's modulus, capturing type and size of defect. Both C_M / C_T, and S_D / S_P are measures of size of defects. All three of these descriptors capture a component of size and the descriptor surface area was removed from the model. Results are shown in Table 3-17 for test sets 4 and 5.

Table 3-17: Analysis 1 (vacancy only) for Poisson's ratio with a minimal feature selection compares the QSPR results using C_{N2} / C_T, C_M / C_T or S_D / S_P.

Data Set Description	**R^2_{Train} R^2_{Test}**	**Categories of Feature Types**		
		Size	**Chiral Angle**	**Counts, % Defects**
Test set 4; r = 3.5 –21 Å	0.85 0.87		Chiral Angle	C_{N2} / C_T
Test set 5; r = 2 – 21 Å	0.85 0.87		Chiral Angle	C_{N2} / C_T
Test set 4; r = 3.5 –21 Å	0.87 0.83		Chiral Angle	C_M / C_T
Test set 5; r = 2 – 21 Å	0.87 0.89		Chiral Angle	C_M / C_T
Test set 4; r = 3.5 –21 Å	0.87 0.83		Chiral Angle	S_D / S_P
Test set 5; r = 2 – 21 Å	0.87 0.89		Chiral Angle	S_D / S_P

Results for vacancy size (S_D / S_P or C_M / C_T) were only slightly better than for vacancy type and size (C_{N2} / C_T). Poisson's ratio is more sensitive to size of defect rather than type and size (as Young's modulus). Fairly accurate QSPRs can be generated for Poisson's ratio based on chiral angle and a single descriptor corresponding to a measure of vacancy density.

To compare the effect of the two critical descriptors on both the elastic mechanical properties Young's modulus and Poisson's ratio, multiple linear regression (MLR) models were built (Table 3-18).

Table 3-18: Multiple linear regression coefficients for analysis 1 (vacancy only) for both Young's modulus and Poisson's ratio at radii greater than 1 nm and less than 1 nm support that chiral angle is negligible for larger (greater than 1-2 nm) CNTs in the prediction of both outputs.

Property	Radii	Descriptor Coefficients		Intercept
Young's modulus (GPa)	$r \leq 12$ Å	Chiral Angle	-177	923
		C_{N2} / C_T	-2225	
	$r > 12$ Å	Chiral Angle	-130	869
		C_{N2} / C_T	-1930	
Poisson's ratio	$r \leq 12$ Å	Chiral Angle	0.273	0.08
		C_{N2} / C_T	1.06	
	$r > 12$ Å	Chiral Angle	0.104	0.19
		C_{N2} / C_T	0.16	

For Young's modulus, the dependence on chiral angle at radii greater than 12 Å is 26% less than for radii less than 12 Å. The dependence on C_{N2} / C_T decreases by 13%. The relative effect of C_{N2} / C_T compare to chiral angle for Young's modulus is large. For radii less than 12 Å, the coefficient of C_{N2} / C_T is 12 times larger than the coefficient for chiral angle. For radii greater than 12 Å, the ratio increases to 15. For Poisson's ratio, dependence on chiral angle and C_{N2} / C_T decreases even more, 62% and 85% respectively, from radii less than 12 Å to radii greater than 12 Å. The relative effect of C_{N2} / C_T is approximately 3.5 times more than chiral angle for radii less than 12 Å and only 1.6 times larger for radii greater than 12 Å.

There are two important observations. First, for Young's modulus, this study quantitatively illustrated chiral angle has a negligible effect at radii greater than 12 Å. Many studies report chiral independence greater than ~20 Å, from DFT to continuum level constitutive models.[45, 52, 184, 185, 188, 189] Results presented here are in agreement with those but have also presented the variance capture per radii as well. With respect to Poisson's ratio, the dependence on chiral angle decreases rapidly as radii increases. For larger CNTs, as those generally produced experimentally, this study implies chiral

angle is not a factor for either Young's modulus or Poisson's ratio. This is important because chiral angle is tedious to measure, via scanning tunneling microscopy or electron diffraction.[190-192] Second, both descriptors rapidly approach zero for the prediction of Poisson's ratio. This implies there is a limiting value for Poisson's ratio. That value would be the y-intercept for a set of large radii CNTs. The largest armchair (30,30) and chiral (27,16) CNTs have a small distribution of Poisson's ratios, 0.245 – 0.247 and 0.225 – 0.251, respectively. The largest zig-zag (30,0) CNT has a larger distribution from 0.095 to 0.182. From this data, the armchair and chiral CNTs have a limiting value of approximately 0.24-0.25. The limiting Poisson's ratio for zig-zag CNTs would fall between 0.1 – 0.18.

A limiting value, by definition, is independent of variables. Coefficients of variables should go to zero. Delta Poisson's ratio was defined as the delta between the assumed limiting value and calculated value. When the limiting value is correctly selected, the coefficient of chiral angle and C_{N2} / C_T will be minimized (approaching zero). Further, the y-intercept will approach zero as well. Using test set 3 (radii greater than 7 Å), the initial limiting factor for zig-zag was set to 0.12, armchair equal to 0.25 and chiral a linear combination of the two. By manually changing the zig-zag and armchair values, it was possible to minimize the y-intercept (0.01) and the coefficient of the chiral angle (-0.0004) by selecting 0.1 for zig-zag and 0.23 for armchair.

3.4.4 Analysis 2: Developing a Vacancy and Functional Group QSPR

The primary goal of analysis 2 is to evaluate whether the vacancy only descriptors and QSPRs can be modularly extended to model both vacancies and methyl surface functionalization. Surface functionalization has both positive and negative

effects on Young's modulus and Poisson's ratio.[193-195] The alkyl surface groups degrade the sp^2 hybridization of the CNT but the slight electron donating is beneficial to Young's modulus with small (< ~1.5%) percentage functionalization.[193, 194] While vacancies tend to increase Poisson's ratio, surface functional groups have been observed to decrease the value.[195] Identifying and quantifying the competitive effects of alkyl functionalization will aid in selecting an optimal value for percentage surface functionalization. Test cases are identified in Table 3-3 through Table 3-8 with a '2' in the analysis column. The test set covers radii from 2 to 7 Å, includes multiple types and sizes of vacancies, sizes of methyl functionalization and a range of chiral angles. In addition, vacancy-only test cases with radii from 7 to 21 Å (test set 4) were included. The importance of test set 4 is to determine if a defect, whether vacancy or functional group, can be sufficiently quantified by two descriptors – one representing the delta of intrinsic properties due to CNT surface structure change and another representing the type and size of functional group.

3.4.4.1 Young's Modulus

The study of the effect of functional groups on CNT moduli is sparse within the literature. Buckling (from axial compression) force was found to decrease by approximately 15% via ethylene functionalization of small diameter (r < 1.7 Å) CNTs.[196] Via an atomic scale finite element model, Zhang reasoned there was little effect on moduli unless functionalization exceeded 10%.[197] Another recent paper identified 10% functionalization as the optimal balance point between decrement of Young's modulus and increase in load transfer between CNT and a polymer matrix.[198] In armchair CNTs, ~7.5% vinyl functionalization yielded about a 10% decrement in Young's moduli while

~12% vinyl groups produced a 15% degradation.[193] Another study quantified moduli increases with small percent loadings of hydrocarbon functional groups for a variety of CNT sizes and chiralities.[194]

Data was arranged into 3 sets, based on radii. Comparison of test sets 1 and 2 will isolate the small radii effects. Comparison of test sets 2 and 4 will shed some light on whether vacancy and methyl groups can both be treated as defect descriptors.

Table 3-19: QSPRs for Young's modulus using all descriptors as inputs for cases including both vacancies and methyl surface functionalization use the same descriptors for the vacancy only analysis as well as an additional descriptor to represent the methyl group.

Data Set Description	$\mathbf{R^2_{Train}}$ $\mathbf{R^2_{Test}}$	**Categories of Feature Types**			
		Size	**Chiral Angle**	**Counts, % Defects**	**Functional Group**
Test set 1; r = 2 – 7 Å	0.91 0.97	L/D	Chiral Angle	% Double Defects % Single Defects S_D / S_P	% Methyl
Test set 2; r = 3.5 – 7 Å	0.95 0.89	Surface Area (S_P)	Chiral Angle	# Single Defects % Double Defects C_{N2} / C_T	% Methyl
Test set 4; r = 3.5 –21 Å	0.95 0.95	Surface Area (S_P)	Chiral Angle	Defect Surface Area (S_D) % Double Defects % Single Defects C_{N2} / C_T	% Methyl

To identify critical descriptors, they are first separated into four categories. For test set 1, aspect ratio was selected as a critical descriptor, which indicates Young's modulus is not independent of small radii. The R^2_{Test} and R^2_{Train} values provide a measure of predictive power and accuracy. Comparing test sets 2 and 4, accuracy and predictive power are very similar but the selected descriptors for the defect category are considerably different. This provides mixed results for the ability to model all defect types with a single QSPR. The methyl functional groups contribute to both descriptors

C_{N2} / C_T and M_N / C_T. The table below illustrates how to determine the contribution to each.

Table 3-20: To calculate the number of non-sp^2 carbons for a single defect, one must multiple by three whereas for a double defect, one must multiple by four. For a surface methyl group, there is a single non-sp^2 carbon per group.

Test Case	# Single Defects	# Double Defects	# Non-sp^2 C's (C_{N2})	C_{N2} / C_T	# Methyl Groups (M_N)	M_N / C_T
n7m4chiS30	29	0	87	0.0915	0	0
n7m4chiS15	14	0	42	0.0435	0	0
n7m4chiPerf	0	0	0	0.0000	0	0
n7m4chiMetS30	0	0	29	0.0287	29	0.0287
n7m4chiDVt15	0	14	56	0.0588	0	0

A single defect creates three non-sp^2 hybridized carbons, a double defect has four and a methyl group has a single non-sp^2 hybridized carbon. The methyl group contribution to C_{N2} / C_T captures the deleterious effects on the intrinsic CNT properties and M_N / C_T represents the intrinsic effect of the surface functional group (for example, its electron donating or withdrawing properties). It would be straightforward to add descriptors for other functional groups, extending the modular power of this informatics QSPR-descriptor approach. Namilae compared functionalizing a (10,10) CNT with multiple alkyl groups – C_2H_3, C_3H_5, C_4H_7, C_5H_9, all at about 1% density but distributed about the central region.[194] A high strain rate was used (0.2 fs time step, 1500 time steps, strain between 0.5 and 1 Å) possibly producing anomalous results.[60] However, it is the trends between the alkyl groups that are of interest. With the exception of a noted outlier, the results predicted an increase in stiffness of about 0.1% for each additional carbon.[194] This type of weighting for alkyl groups would be expected for an alkyl functional group descriptor. For example, one carbon could have a normalized weight

factor (coefficient to functional group descriptor) of 1, 2 carbons a factor of 1.1, 3 carbons 1.15, etc.

Extending the vacancy-only minimal feature set QSPR for Young's modulus (Table 3-11) to include M_N / C_T yields a slight degradation in accuracy compared to the full descriptor test set for analysis 2 Young's modulus but greatly improves interpretability. The results are shown in Table 3-21. Kuang identified a similar functional form for delta energy with vinyl groups: $\Delta E = (-ax^2 + bx)$*(Energy of pristine CNT), where x is proportional to M_N / C_T or C_{N2} / C_T (values are equal for methyl functionalization).[193] For small values of percentage surface functionalization, delta energy increases ($bx > ax^2$). As percentage functionalization increases, the delta energy decreases ($ax^2 > bx$).

Table 3-21: QSPRs for Young's modulus for both vacancies and methyl surface functionalization piece-wise extends the vacancy-only analysis to include M_N / C_T to represent the surface functionalization.

Data Set Description	**R^2_{Train} R^2_{Test}**	**Categories of Feature Types**			
		Size	**Chiral Angle**	**Counts, % Defects**	**Functional Group**
Test set 1; r = 2 – 7 Å	0.89 0.96		Chiral Angle	C_{N2} / C_T	M_N / C_T
Test set 2; r = 3.5 – 7 Å	0.92 0.93		Chiral Angle	C_{N2} / C_T	M_N / C_T
Test set 4; r = 3.5 –21 Å	0.92 0.95		Chiral Angle	C_{N2} / C_T	M_N / C_T

Comparing test set 2 to test set 4 for the minimal descriptor set clearly indicates that the vacancy-only QSPR can be modularly extended to model vacancies and methyl group defects. The R^2_{Test} and R^2_{Train} values are almost the same with identical descriptors.

Model validation includes accuracy, predictive power and robustness.[129] Robustness is a signal processing term and refers to approaches that are not significantly degraded when standard operating conditions change. Starting with a large number of variables that are difficult to control, it is likely that some variables will be selected by chance. Y-scrambling is used to test for this. The output y values are scrambled and the correlation coefficient is calculated. The y-scrambled R^2 value is compared to the R^2 values of the QSPR model. If the R^2 values are similar, the model is not robust. Y-scrambled was used to test robustness for all analyses. Example results are presented in Figure 3-9. The R^2 value for the y-scrambling results is 0.16, very desirable for robustness.

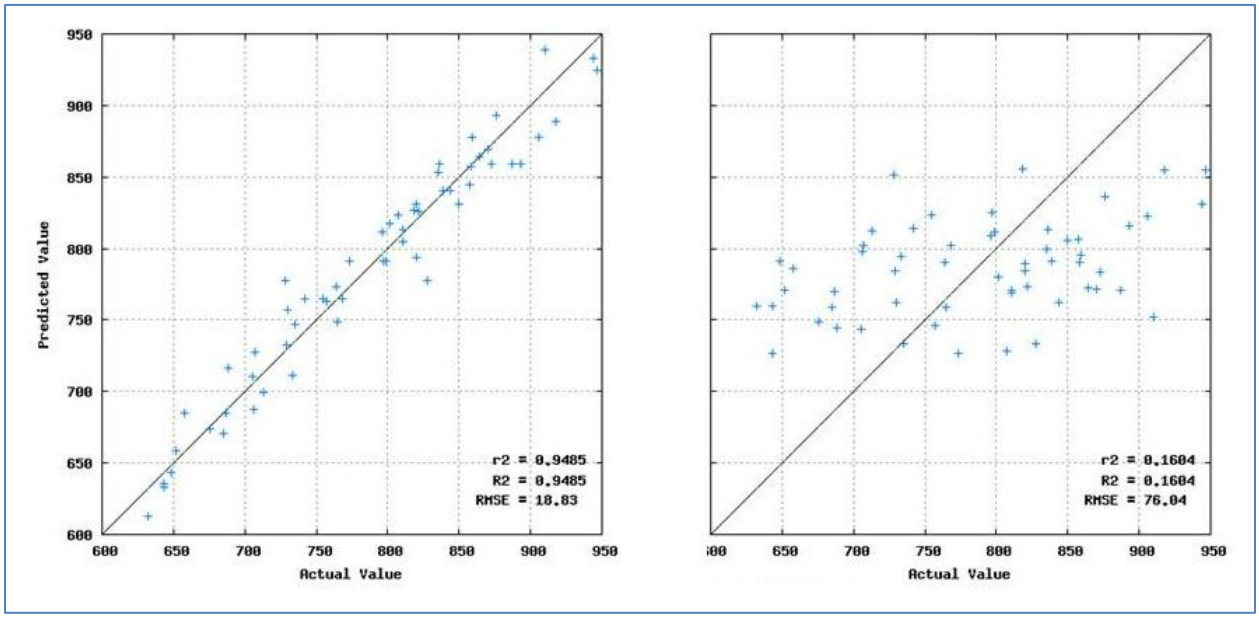

Figure 3-9: Y-scrambling provides a measure of robustness and was implemented for all analyses. Test set 4 (r = 3.5 –21 Å) predicting Young's modulus using all descriptors is provided as an example.

For both analyses of Young's modulus, C_{N2} / C_T was identified as a critical descriptor. It captures the non-linear decrease in Young's modulus with respect to

increase in defect size. As defect size increases, the change to Young's modulus grows smaller.[176-178, 193, 199] C_{N2} / C_T quantifies that change. Single-vacancy, double-vacancy, 4-vacancy and 7-vacancy defects are shown in Figure 3-10.

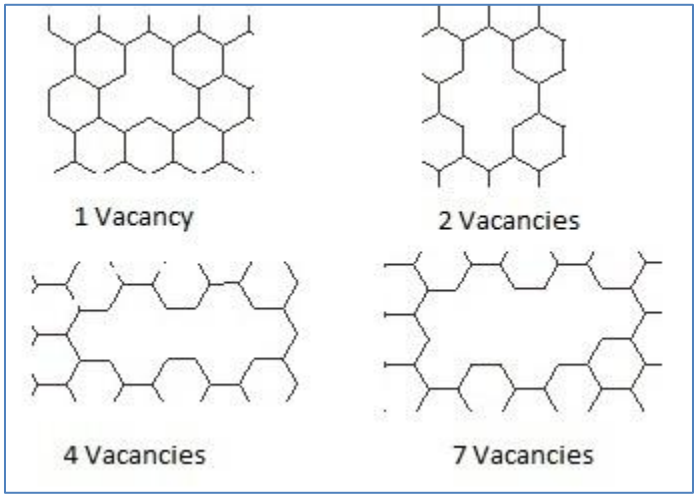

Figure 3-10: The number of non-sp^2 hybridized carbons increases non-linearly as size of the defect increases.

The single vacancy has 3 non-sp^2 hybridized carbons whereas the double, quadruple and 7-vacancy defects have 4, 7 and 9 respectively (as shown here). As defect sizes get larger, the arrangement of atoms leads to an average for the number of non-sp^2 hybridized carbons. A methyl group only has 1 non-sp^2 hybridized carbon. An advantage of C_{N2} / C_T is that should be easily experimentally measurable (Raman spectroscopy).[166, 167] If this is true, computational models can be directly linked to experimental data, tuning the computational models empirically to match that data, creating more accurate computational models.

3.4.4.2 Poisson's Ratio

Literature results for the effect of Poisson's ratio are extremely sparse. Coto found that Poisson's ratio decreases from 0.25 to 0.2 with 10% surface functionalization

of carboxylic groups.[195] In this study, for CNTs of radii approximately equal to 4 Å, methyl functionalization rendered a very slight increase for zig-zag (10,0), no change for armchair (5,5) and slight decrease for chiral (8,3). Poisson's ratio for the larger (10,10) armchair decreased.

Table 3-22: Poisson's ratio for methyl functionalized CNTs revealed only slight changes for zig-zag, armchair and chiral CNTs.

Test Case	Theoretical Radius (Å)	% Surface Defect	Type Defect	Poisson's Ratio
n8m3chiS30	3.90	3.0	Single vacancy	0.248
n8m3chiS15	3.90	1.5	Single vacancy	0.196
n8m3chiPerf	3.90	0		0.158
n8m3chiMetS30	3.90	3.0	Methyl group	0.143
n8m3chiMetS15	3.90	1.5	Methyl group	0.147
n5m5armS30	3.43	3.0	Single vacancy	0.330
n5m5armS15	3.43	1.5	Single vacancy	0.252
n5m5armPerf	3.43	0		0.208
n5m5armMetS30	3.43	3.0	Methyl group	0.207
n5m5armMetS15	3.43	1.5	Methyl group	0.208
n10m10armS30	6.86	3.0	Single vacancy	0.296
n10m10armS15	6.86	1.5	Single vacancy	0.262
n10m10armPerf	6.86	0		0.235
n10m10armMetS30	6.86	3.0	Methyl group	0.192
n10m10armMetS15	6.86	1.5	Methyl group	0.200
n10m0zzS30	3.96	3.0	Single vacancy	0.197
n10m0zzS15	3.96	1.5	Single vacancy	0.136
n10m0zzPerf	3.96	0		0.067
n10m0zzMetS30	3.96	3.0	Methyl group	0.077
n10m0zzMetS15	3.96	1.5	Methyl group	0.068

The data was arranged into three sets, based on radii. The R^2 values for all three test sets were approximately 0.9. Down-selecting to the minimal descriptor set and re-creating the QSPRs produced the results in Table 3-23.

Table 3-23: The minimal vacancy and methyl group descriptor set was used to predict Poisson's ratio.

Data Set Description	R^2_{Train} R^2_{Test}	Categories of Feature Types			
		Size	Chiral Angle	Counts, % Defects	Functional Group
Test set 1; r = 2 – 7 Å	0.88 0.95		Chiral Angle	C_{N2} / C_T	M_N / C_T
Test set 2; r = 3.5 – 7 Å	0.91 0.81		Chiral Angle	C_{N2} / C_T	M_N / C_T
Test set 4; r = 3.5 –21 Å	0.87 0.88		Chiral Angle	C_{N2} / C_T	M_N / C_T

Accuracy and predictive power were the same for the three descriptor model compared to the full descriptor QSPR but with an increase in interpretability. There is little difference between test set 1 and test sets 2 and 4, confirming Poisson's ratio has little dependence on radii even at small values. The accuracy and predictive power values for test set 2 and test set 4 are similar, indicating that the single-vacancy QSPR can be extended to both vacancy and methyl group defects. Effects of the functional group can be split into two categories – as a surface defect and polymer chain. These results indicate it is likely that a single QSPR can be extended to multiple surface defect types. However, investigation of more types of functional groups is necessary to fully reach that conclusion.

3.5 Conclusion

Carbon nanotubes (CNTs) have outstanding physical properties and are considered to be the ultimate mechanical filler for reinforcement of polymer composites.[33, 68] Experimental results have fallen well short of computational predictions, possibly due to the lack of inclusion of manufacturing defects in computational models. Further, some defects are desirable for optimization of CNT-composite properties, such as surface functionalization for improvement to interfacial

shear strength. There is no simple path to couple experimental and computational results and approaches. The number of variables affecting CNT and CNT-reinforced composite properties is both experimentally and computationally prohibitive for complete exploration of the parameter space. Inspired by their successful role in drug design and discovery, informatics-based descriptors and quantitative structure property relationships (QSPR) were investigated to potentially address these issues. Can the critical variables for specific material property optimization be identified, limiting the size of the parameter space? Can experimental and computational descriptors be included in a single model, enabling real-time improvements to empirical models and potentially linking experimental-computational efforts? Are the identified critical variables experimentally controllable and easily characterized?

MD simulations for a diverse set of CNTs were carried out to determine individual Young's moduli and Poisson's ratios. Twenty constitutional, topological and physicochemical descriptors were calculated and evaluated in QSPRs for both mechanical properties in two separate analyses: vacancy only and vacancy plus methyl functionalization. Star plots, partial least squares (PLS) and y-scrambling were used to aid in feature selection, data partitioning, critical variable identification, model accuracy, predictive power and robustness.

Analysis 1 focused on random distributions of vacancies. Young's modulus study analysis identified two critical descriptors, chiral angle and the density of non-sp^2 hybridized carbons (C_{N2} / C_T). For radii greater than 12 Å, C_{N2} / C_T alone captured 97.4% of the model variance. The correlation coefficient for training and test sets (3.5 to 21 Å) was 0.95 and 0.89, respectively. Zig-zag CNTs were shown to be less resilient

to vacancies. For Poisson's ratio, the 3.5 to 21 Å test set calculated R^2_{train} and R^2_{test} values of 0.85 for both. Two critical descriptors were identified, chiral angle and the number of missing atoms to total atoms (C_M / C_T). Difference in accuracy and predictive performance of QSPRs for Poisson's ratio using C_{N2} / C_T or C_M / C_T was negligible. For Poisson's ratio, the effect of chiral angle fell off rapidly with increased radii and Poisson's ratio approached a limiting value. For armchair and chiral CNTs (vacancy percentages between 0% and 3%), Poisson's ratio limit was close to 0.23 – 0.24. Zig-zag CNTs had a limiting Poisson's ratio of approximately 0.10. It is promising that chiral angle is less of a factor (or not) at larger diameters for Young's modulus and Poisson's ratio because it is difficult to characterize experimentally.[190-192] Potentially, Raman spectroscopy could be utilized to predict C_{N2} / C_T.[165-167]

Analysis 2 focused on both randomly distributed vacancies and methyl surface functional groups. Three critical descriptors were identified, chiral angle, C_{N2} / C_T, and the density of surface methyl groups (M_N / C_T). The training and test correlation coefficients were 0.92 and 0.95, respectively (3.5 to 21 Å). This analysis implies QSPRs can be modularly extended to multiple types of surface defects. Comparing data from Namilae and Kuang, the potential of using a weighting factor with a surface functional group descriptor is very promising and needs further study.[193, 194] Poisson's ratio selected the same critical descriptors chiral angle, C_{N2} / C_T, M_N / C_T. Poisson's ratio decreases with methyl group addition for chiral CNTs, was constant or decreased slightly for armchair CNTs and had a small increase for zig-zag CNTs (up to 3.0% surface vacancy).

CHAPTER 4

POISSON'S RATIO

This molecular dynamics (MD) analysis achieved a systematic evaluation of differences in Poisson's ratio based on procedural methods, chirality, delta strains, percentage surface defects, temperatures and strain rates. Poisson's ratio (delta strain of 0 – 5%) has a limiting value of 0.10 for zig-zag and 0.25 for armchair (carbon nanotubes (CNTs) with diameters greater than 2 nm) even for CNTs with surface vacancies or methyl functionalization up to 3.0%. Zig-zag CNTs are brittle whereas armchair CNTs demonstrated ductile behavior. For both chiralities, Poisson's ratio exhibits a strain varying, nonlinear elastic behavior. For zig-zag, a 1% delta strain centered about 4% strain was 45% less than a 1% delta strain centered about 1% strain. For armchair, the decrease between the 4% and 1% strain was less at 19%. A strain rates of $0.5 * 10^{-4}$ ps^{-1} or slower was identified sufficient to produce consistent results. Poisson's ratio decreases slightly from 0 K to 300 K and increases from 300 K to 1600 K, regardless of the presence of surface defects. Yield strength was proposed as a simple mathematical function of chiral angle.

4.1 Introduction

Single-walled CNTs are transversely isotropic, requiring five independent elastic properties for a full description of elastic mechanical behavior. These properties are Young's modulus (E), Poisson's ratio (ν), longitudinal shear modulus (G), plane-strain bulk (B) and in-plane shear moduli (S).[200] For linear behavior, the properties are related as follows.

$$\nu = \frac{E}{2G} - 1 \tag{42}$$

$$B = \frac{E}{3(1-2\nu)} \tag{43}$$

Poisson's ratio is defined as the ratio of the fraction of lateral contraction to the fraction of axial expansion as it is elastically stretched.[10] It provides insight into chemical bonding of atoms and delta energies for bond length and angle deviations from equilibrium.[201] When Poisson's ratio is less than ~0.125, changes in bond length are more energetically favorable than changes in bond angle.[202] For Poisson's ratio greater than ~0.125, bond angle changes are favorable.[202] Materials with a Poisson's ratio between 0 and 0.125 are generally accepted as brittle.[203] It is a function of the atomic packing density and arrangement, inferring information about the atomic properties of the material.[201] For highly nonlinear elastic materials (e.g., biomaterials, microstructured materials) it is advantageous to define a strain varying Poisson's ratio.[204] Accurate predictions for Poisson's ratio of CNTs is an unsolved issue with literature values from 0.06 to 1.414.[187] This analysis provides a systematic evaluation and understanding of discrepancies based on chirality, size, percentage defects, temperature and strain rates. For CNTs, this analysis will show Poisson's ratio is not constant in the elastic region and the cause of that nonlinear elastic behavior is driven by the unique atomic structure. Poisson's ratio is known to infer behavior about yield strength, in spite of the lack of a quantitative relationship between Poisson's ratio and plastic deformation behavior.[201] However, exploiting the strain varying behavior of Poisson's ratio in single-walled CNTs, this study was able to predict yield strengths on par with those predicted in the literature.

Values for Poisson's ratio have a large distribution in the literature. One DFT study predicted values between 0.11 and 0.19[46] while two molecular dynamics results calculated 0.13 – 0.19[48, 179, 180] and another 0.32-0.36.[177] Analytical models projected values of 0.21 and 0.277-0.280.[45, 181] Tight-binding molecular dynamics found Poisson's ratios of 0.285 and 0.287.[174, 182] Shen reported a value of 0.16[200] while Xiao calculated it to be 0.2.[205] Other results include an *ab initio* rendered 0.32[50] and a finite element prediction of 0.31 – 0.35.[183]

Walters and Yu measured the yield strength of SWCNT ropes to be 5.3%[66] and 5.8%[206], respectively. Arc discharge grown multi-walled CNTs (generally believed to be largely defect free with only the outer shell participating in load transfer) failed at 1.1 to 6.3% strains.[207] Early computational results were high, up to 30-40%, due to high strain rates.[59, 179] Development of an Arrhenius model via a temperature and strain rate evaluation provided computational results on par with experimental at 9 +/- 1%.[60] Other computational results include 15.8%[63] and 18.7%[62] Nardelli proposed a value based on the energies of bond rearrangements of 5-6% yield strain, in good agreement with experiments.[208]

There are many reasons for disagreement in the data. CNTs span multiple length scales with a variety of computational methods used for calculations. There are a multitude of properties to consider (chirality, size, surface defects, surface functionalization, delta strains, etc). Procedurally, strain rates, temperatures and calculation methods differ. This study uses molecular dynamics (MD) to quantify differences due to procedure and CNT properties. It will be shown that Poisson's ratio exhibits nonlinear elastic behavior. Defining as the average over 0-5% strain, a limiting

value of 0.10 for zig-zag and 0.25 for armchair will be derived. A simple mathematical function of Poisson's ratio will be used to predict yield strength, on the order of 10% for pristine zig-zag CNTs. Critical variables will be identified, setting the groundwork to identify descriptors and extend quantitative structure property relationships (QSPR) to plastic deformation behavior.[56, 112]

4.2 Computational Method and Description of CNT Systems

The adaptive intermolecular reactive empirical bond order (AIREBO) potential was used for MD simulations. It extends the second generation of the reactive empirical bond order (REBO) potential to include torsional and pair-wise van der Waals interactions.[146] The REBO potential accurately describes carbon-carbon and hydrocarbon molecular short-range interactions allowing for bond breaking, formation and rehybridization.[18] To correct for overestimation of the maximum force required to break a carbon-carbon bond, the cutoff distance within the REBO formulation was modified from 1.7 to 1.95 nm.[20, 209]

The test set was composed of 100 MD simulations, diameters from 2 to 23 Å, chiral angles representing zig-zag (0°), chiral (four angles between 15° and 22° and armchair (30°) and single vacancy and methyl functionalization surface defects at 1.5% and 3.0%. Five temperature and five strain rates were evaluated, from 0 K to 2400 K and 10^{-3} ps^{-1} to 10^{-6} ps^{-1}. Length was held constant at 100 Å. Pristine CNTs were created with JCrystal Nanotube Modeler. Surface defects were added with Python scripts. Position of defects were randomly selected, at least 4 Å from the CNT end and at least 4 Å of separation between any two defects. The effect of diameter on Poisson's ratio falls off rapidly with diameter increase.[56] Chiral angle and surface defects are

critical in accurately predicting Poisson's ratio.[56] Surface defects were limited to 3%, similar to the experimental results of Peng (0.02 – 3.75% vacancies).[55] These strain rate and temperatures are sufficient in predicting tensile strength for both pristine single and multi-walled CNTs.[60, 61] Strain rate is calculated in (44).

$$Strain\ Rate = \frac{\Delta l / l_o}{t} \tag{44}$$

Δl is delta length change, l_o is the initial length and t is the total relaxation time for applied strain. For example, if a CNT of 100 Å is stretched 0.25 Å and relaxed for 25,000 fs, the strain rate would be ((0.25 Å / 100 Å) / 25,000) fs^{-1} = 10^{-7} fs^{-1} = 10^{-4} ps^{-1}. For 80 of the 100 cases, temperature was 0 K and strain rates were on the order of 10^{-4} ps^{-1}. Tensile strain was applied by moving the carbons at both ends 0.1 Å, fixing them in place for a new length of 100.2 Å, allowing the structure to achieve the low energy conformation and then repeating this process 25-50 times for total strains between 5 and 10%. For 20 strain rate simulations, the applied strain was held constant at 0.25% per applied strain. As the CNT was stretched, the percentage strain increased slightly with each applied strain (0.25%, 0.5006%, 0.7519%, etc). A time step of 0.5 fs was used. Langevin friction force[210, 211] scheme was used as the thermostat to scale velocities to the appropriate temperature and the Berendsen[149] thermostat was used to maintain a constant temperature. The study took approximately 3,100 total simulations.

For a SWCNT, Poisson's ratio is the fractional change in radius to the fractional change in length as an axial load is applied, shown in (45). Initial and final are defined as the initial and final strains.

$$Poisson's\ Ratio = -\frac{lateral\ strain}{longitudinal\ strain} = -\frac{(r_f - r_i)/r_i}{(l_f - l_i)/l_i} \tag{45}$$

In the elastic region, Poisson's ratio is constant for most materials.[201, 212] However, this study shows Poisson's ratio varies with strain for CNTs by evaluated multiple delta strains. Multiple sections from 10% to 80% of the original CNT (centered about the midpoint) were analyzed. Python scripts on the order of a few thousand lines of code were written to create test cases, automate runs, collect data, perform calculations and analyze results.

4.3 Results and Discussion

Values for Poisson's ratio vary widely in the literature. Reasons for this variation include differences in procedural methods[48], multitude of variables necessary to consider[56] and the experimental conditions of strain rates and temperatures.[60, 61] Because CNTs range in length from nm to mm, multiple computational methods are used to evaluate them from *ab initio* to continuum level. This study focuses solely on MD, eliminating inconsistencies across different methods. The effect of each of the following will be quantified in this analysis.

1) Procedural differences from radii calculations and CNT section size
2) Effect of chirality, diameter and delta strain (elastic region)
3) Influence of surface vacancies and methyl functional groups $\leq$ 3%
4) Variance associated with computational strain rates and temperatures

4.3.1 Procedural Variation

Two procedural questions were considered, a) what is the most accurate method of calculating CNT radii and b) does Poisson's ratio vary based on the size of CNT section? The lateral strain calculation is very sensitive to small variances in average radius. In Figure 4-1, the individual carbon radii for (60,0) CNTs with 0% and 3.0% are

shown. For the 0% (60,0) CNT, the initial and final average radii (top and bottom row in figure) are 23 Å and 23.1 Å, respectively, for a delta average radii of 0.1 Å. For the 3.0% (60,0) CNT, the variance in the initial and final average is ~2 Å and ~1 Å, respectively. A small error in radii calculation would mask the delta average radii. If the average radius was miscalculated by +/- 0.05 Å, the resulting Poisson's ratio could be off by almost 50%.

There are several methods to calculate an average horizontal distance across a cylinder composed of discrete points. Three methods were evaluated, a) 3D surface meshing, b) diameter calculation with points opposite the cylinder's cross-section and c) calculating each carbon's radius. Of the three, the radii calculation proved most accurate and easiest to implement.

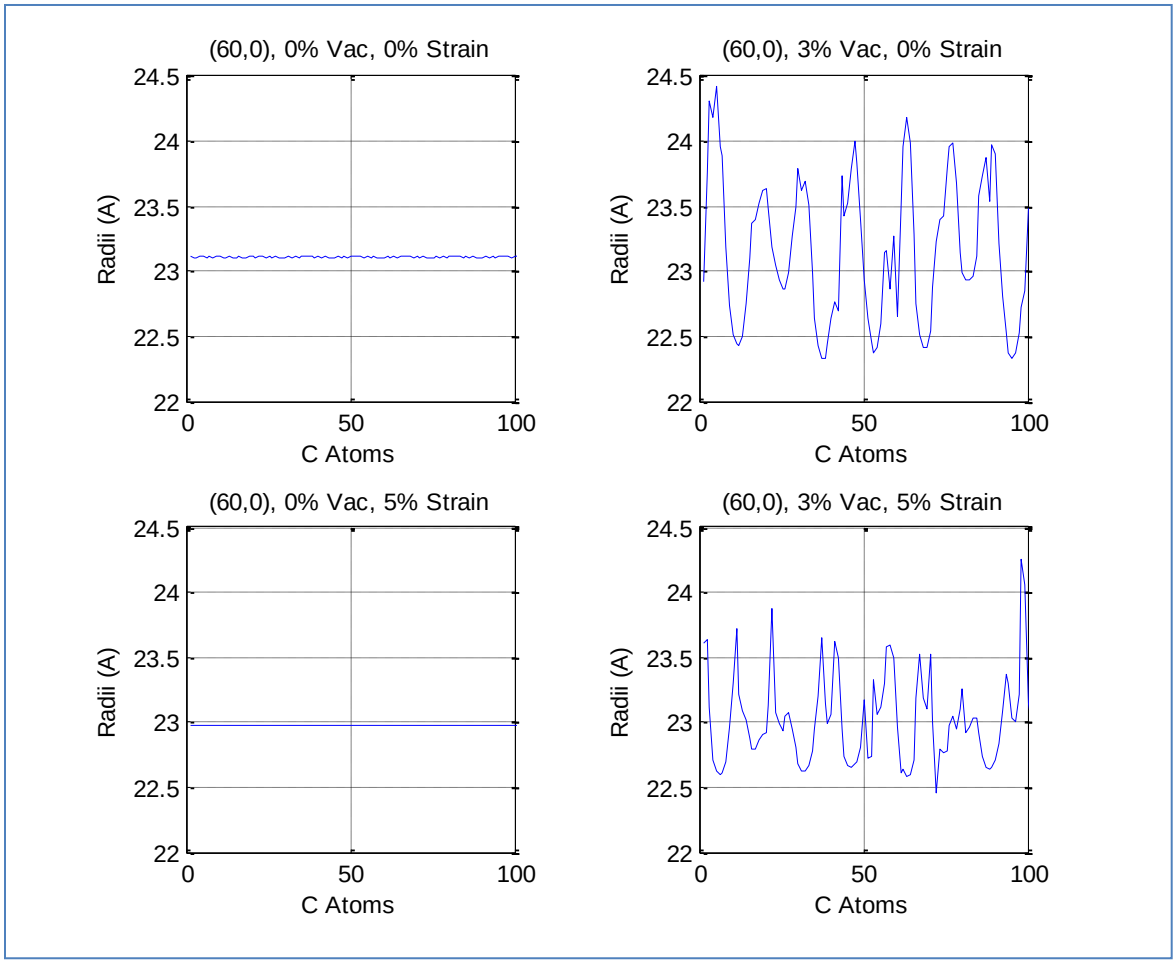

Figure 4-1 : The column on the right shows the 0% (60,0) CNT individual atomic radii at 0% strain (top) and 5% strain (bottom). The column on the left illustrates the 3% surface vacancy (60,0) CNT individual atomic radii. The deviation for individual radii for 3% surface vacancy is large, varying up to 2 Å between measurements.

Surface meshing programs can calculate the volume of a 3D object, which is a function of the average radius.[213] Meshlab is an open-source, fairly user-friendly package for processing and editing unstructured 3D triangular meshes.[214] It provides a complete tool set for editing, cleaning, healing, visually inspecting, rendering and converting meshes. While this approach could provide a very accurate solution, implementation was difficult. Radii calculations were not of sufficient accuracy but it was probably due to lack of user knowledge.

Visualization programs like Visual Molecular Dynamics (VMD) usually provide tools to measure distance between two discrete atoms.[215] While it is possible to measure or calculate the horizontal diameter, there are a few challenges. CNTs are a set of discrete points (carbon atoms) and two atoms opposite each other on a cross-section may not exist. Temperature and surface defects make the CNT surface to buckle in and out, with large variance in individual cross-section radii (see Figure 4-1). Several cross-section diameters will need to be calculated and averaged. The pseudo-code to calculate the CNT diameter is as follows.

For all atoms in the CNT

Select a ring of carbon atoms (difference in z-coordinate $\leq$ 0.5 Å)

For all atoms in the ring

Find the discrete atoms opposite

Calculate the distance between the two discrete points

Project distance through azimuth and elevation angles to the radius of the circle

Average all radii in horizontal ring, calculate standard deviation

Average all ring radii, calculate standard deviations

Azimuth and elevation angles are shown in Figure 4-2. Atoms *i* and *j* are selected based on their proximity to being directly opposite each other in a horizontal cross-section. The real distance between atoms *i* and *j* is *r* and r_{hz} is the radius of a perfectly horizontal cross-section.

$$r_{hz} = r\,cos(El)\frac{1}{cos\,(Az)} \tag{46}$$

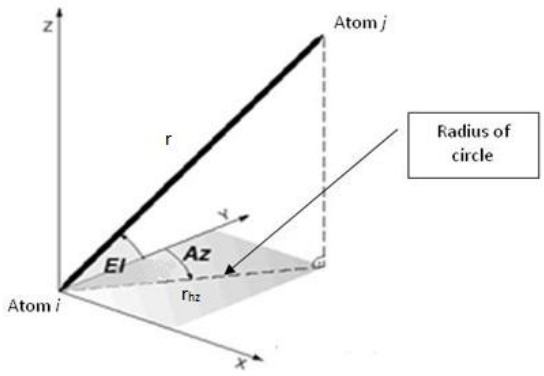

Figure 4-2: The azimuth and elevation angles required to project measurements between two discrete atoms to the radius of the circle, as described in the pseudo-code, is visually shown.

Atoms *i* and *j* are not exactly located opposite each other horizontally or vertically, making it necessary to mathematically project the delta to the radius of a perfectly horizontal cross-section. Results were reasonable but small measurement errors provided statistical variation on par with change in average radius.

The most accurate method was calculation of carbon radii. It was necessary to translate the center of mass to the origin because CNTs do move horizontally under strain, more so with defects and at higher temperatures.[182] All carbon radii were calculated and averaged for the initial and final strains.

The specified size of CNT section used for calculations was investigated for deviations in average initial and final radii calculations. Table 4-1 presents the variance for (10,0) zig-zag and (5,5) armchair CNTs, with radii of 3.96 Å and 3.43 Å, respectively. All CNT sections were centered about the midpoint.

Table 4-1: Poisson's ratio, defined at 0 to 5% delta strain) for various sized sections centered about the middle reveals that the value is the same for pristine CNTs regardless of section size but varies with both vacancy and methyl defects. This is an anomalous statistical effect and can be addressed by using the largest section size possible.

Test Case	5%	10%	20%	30%	40%	60%	80%	Std Dev
(10,0)	0.0669	0.0669	0.0669	0.0669	0.0669	0.0669	0.0669	0.0000
(10,0) 0.5% vacancy	0.0674	0.0673	0.0672	0.0658	0.0664	0.0813	0.0954	0.0113
(10,0) 1.5% vacancy	0.0690	0.2161	0.1871	0.1374	0.1344	0.1388	0.1404	0.0462
(10,0) 3.0% vacancy	0.2511	0.2860	0.2488	0.2296	0.1778	0.1853	0.2033	0.0393
(10,0) 1.5% methyl	0.0741	0.0719	0.0705	0.0703	0.0701	0.0659	0.0656	0.0031
(10,0) 3.0% methyl	0.0747	0.0634	0.0672	0.0770	0.0794	0.0729	0.0739	0.0056
(5,5)	0.2081	0.2082	0.2082	0.2081	0.2081	0.2080	0.2080	0.0001
(5,5) 0.5% vacancy	0.2022	0.2020	0.2021	0.2021	0.2023	0.2296	0.2310	0.0137
(5,5) 1.5% vacancy	0.3131	0.2637	0.2738	0.2478	0.2419	0.2712	0.2536	0.0237
(5,5) 3.0% vacancy	0.4475	0.3892	0.3762	0.3747	0.3327	0.3133	0.3161	0.0478
(5,5) 1.5% methyl	0.2036	0.2082	0.2064	0.2067	0.2071	0.2099	0.2116	0.0026
(5,5) 3.0% methyl	0.1287	0.2457	0.2105	0.2126	0.2153	0.2018	0.2068	0.0357

Poisson's ratios for pristine (10,0) and (5,5) nanotubes are 0.07 and 0.21, respectively, regardless of section used. This implies necking is not an issue and 0-5% strain is within the elastic region. The largest deviation across the CNT section sizes was found with the largest percentage surface defects. For the (5,5) CNT with 3.0% defects, Poisson's ratio calculated from the middle 5% was 0.4475 and 0.3161 from the middle 80% CNT section. The data illustrates fluctuation for the smaller sections approaching a steady-state value as the CNT section size increased. Visual inspection revealed this was due to over-counting the effect of a defect in the smaller sections. During the axial loading of the CNT, the edge atoms were fixed in place in all three dimensions, not allowing them to contract as much as they would if only the z-coordinate was fixed. Using 30 – 70% of the CNT for radial calculations rendered near constant results. Another important observation from Table 4-1 is the difference

between Poisson's ratio for the (10,0) and (5,5) CNT. The value of the (10,0) CNT is approximately 0.07 and the value for the (5,5) CNT is 0.21, a factor a three difference. Since these two CNTs are of similar radius, this difference must arise from chirality.

4.3.2 Variations Due to Delta Strain, Chirality and Diameter

The variance of Poisson's ratio was quantified with respect to chirality, diameter and delta strain. The study shows that Poisson's ratio is almost independent of radius for radii greater than 2 nm but is not independent of chirality. It is also shown that Poisson's ratio is dependent on delta strain. Data in Table 4-2 illustrates Poisson's ratio increases as radius increases approaching a limiting value for radii greater than 2 nm. The 0-5% delta strain value approaches 0.10 for zig-zag CNTs and 0.25 for armchair CNTs.

Chiral CNTs have a limiting value between zig-zag and armchair but closer to armchair. Zig-zag CNTs are brittle (Poisson's ratio < 0.125) and bond length changes are energetically favorable. Armchair are considered ductile (Poisson's ratio > 0.125) and bond angle deviations are energetically favorable. These results are in agreement with studies on ductile and brittle behavior of CNTs.[208, 216, 217]

Table 4-2: Poisson's ratio approaches a limiting value as the diameter increases. The limiting value is approximately 0.25 for armchair and 0.10 for zig-zag.

Test Case	Chiral Angle (Rad)	Radius (Å)	0-5% Delta Strain	0-2% Delta Strain	3-5% Delta Strain
Zig-zag					
(10,0)	0	3.96	0.0669	0.1057	0.0351
(20,0)	0	7.93	0.0857	0.1423	0.0416
(30,0)	0	11.89	0.0946	0.1546	0.0432
(60,0)	0	23.32	0.1001	0.1602	0.0456
Chiral					
(7,4)	0.37	3.82	0.1971	0.2285	0.1745
(8,3)	0.27	3.9	0.1573	0.1946	0.131
(17,9)	0.35	9.06	0.2121	0.2587	0.1787
(27,16)	0.38	14.92	0.2247	0.2712	0.1911
Armchair					
(5,5)	0.52	3.43	0.2081	0.2327	0.1916
(10,10)	0.52	6.86	0.2348	0.2746	0.2067
(20,20)	0.52	13.73	0.2467	0.2941	0.2122
(30,30)	0.52	20.59	0.2473	0.2948	0.2143

CNT size has two effects on Poisson's ratio, curvature and non-bonding interactions from the opposite CNT side. As the surface curvature increases (CNT decreases in radii), the out-of-plane non-bonding interaction term grows larger.[184, 218] Second, for radii less than ~1 nm, non-bonding interactions from orbitals on opposite sides of the CNT must be considered. Change in curvature is shown in Figure 4-3, decreasing rapidly to a radius of ~7 Å and approaching zero for radii greater than 15-20 Å. In Table 4-2, Poisson's ratio for zig-zag CNTs increases from 0.0669 to 0.0857 as radius increases from 3.96 Å to 7.93 Å. The value continues increasing from 7.93 Å (0.0857) to 23.32 Å (0.1001) but the change in Poisson's ratio is rapidly decreasing. The same trend is observed for both the chiral and armchair CNTs. As curvature

decreases, the out-of-plane non-bonding interaction term goes to zero. This is the basis for the limiting value of Poisson's ratio.

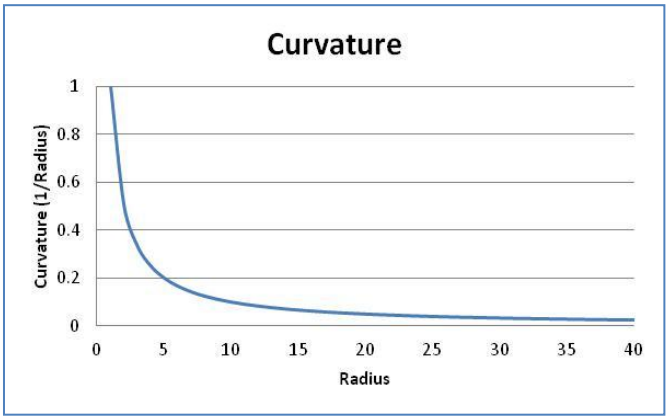

Figure 4-3: Circle curvature decreases rapidly to approximately 1-2 nm and then remains constant.

Figure 4-4 illustrates the effect of non-bonding interactions for very small CNTs (less than 7-10 Å in diameter). The function looks like a 3-part piece-wise linear function. Equilibrium distance for graphene spacing is 3.35 Å.[219] For CNT radii less than this distance, the repulsion term grows rapidly (includes non-bonding interaction from opposite side of CNT). This makes it energetically favorable for a zig-zag CNT (less than 10 Å) under axial tension to undergo a bond rotation to a chiral configuration.[208] As the CNT radius exceeds 7-10 Å, energy per atom is constant. This is the maximum effective interaction distance for van der Waals forces.[60, 136]

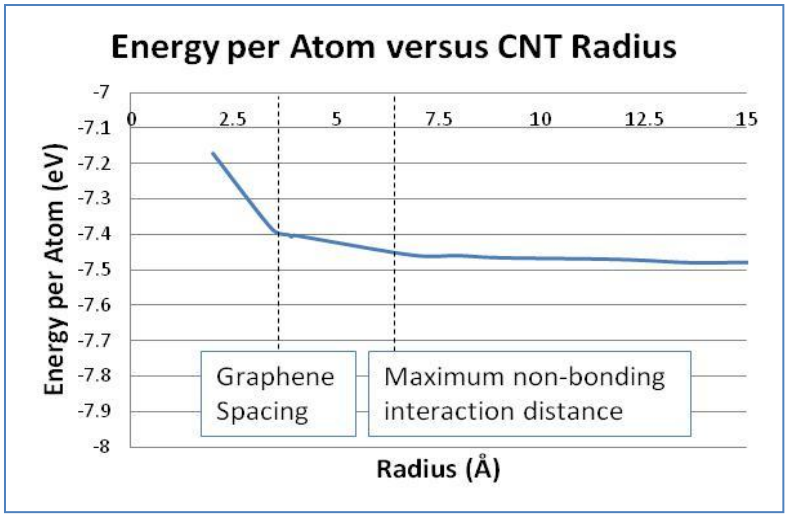

Figure 4-4: The energy per atom as the radii increases appears to be a three-piece linear function.

There is a strong dependence on chirality, visualized through an analysis of the hexagonal units under axial stress (Figure 4-5). Qualitatively, zig-zag hexagon unit bonds aligned with the stress vector will be forced closer together whereas armchair is pulled apart. The non-bonding interaction term grows quickly for zig-zag, leading to large energy barriers for bond angle changes (brittle). The opposite is true for armchair, making bond angle changes favorable (ductile). This is the basis for the strong dependence on chirality.

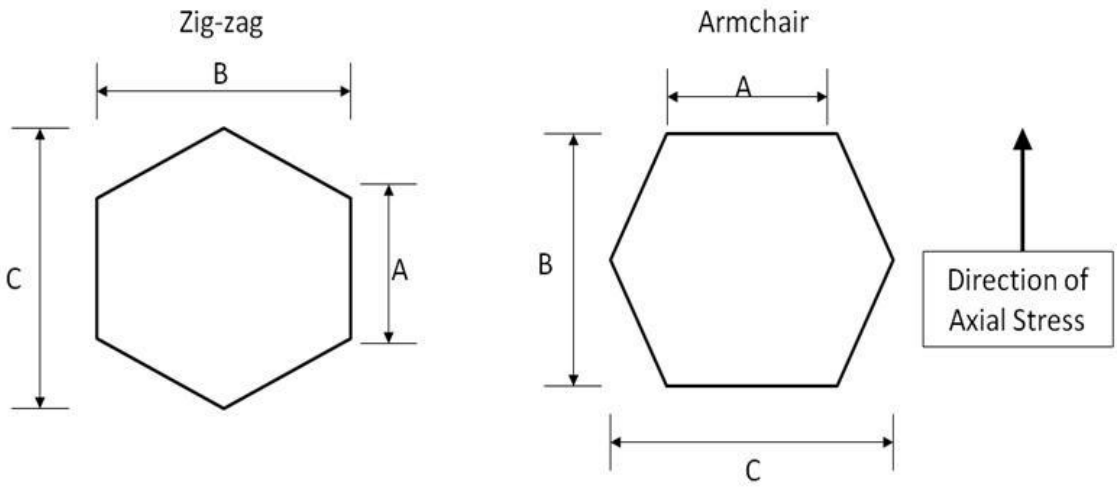

Figure 4-5: The hexagon unit for zig-zag and armchair CNTs shows how the zig-zag bonds are more aligned with the direction of an applied axial tension.

Hexagonal units for pristine (20,20) and (30,0) CNTs, radii of 13.7 Å and 11.9 Å, respectively, were analyzed (Table 4-3). For these CNTs, the effect of curvature is small and non-bonding interaction from opposite side is negligible. Poisson's ratio values for the individual hexagonal unit were calculated and in good agreement with Poisson's ratio values for the entire CNT. The lengths A, B and C are identified in Figure 4-5. The axial strain, proportional to delta height, changes linearly throughout 0 to 5% delta strain. The lateral strain, proportional to delta width, is not linear. A material with a Poisson's ratio of 0 is considered completely compressible with no lateral change as the axial tension or compression is applied whereas a material with a value of 0.5 is defined as completely incompressible compensating exactly for the volume change.[10] The hexagon area change (proportional to volume) is more than 50% smaller for the zig-zag CNT, consistent with brittle or compressible materials.

Table 4-3: The hexagonal unit analysis for the (20,20) and (30,0) CNTs compute a Poisson's ratio equal to the values for the entire CNT and also illustrates how bond length changes, bond angle changes and non-bonding interactions influence the non-linear strain varying behavior.

(20,20)	0.1 % Strain	0.1-1% Strain	1-2% Strain	2-3% Strain	3-4% Strain	4-5% Strain
A (Å)	1.400	1.401	1.401	1.406	1.408	1.409
B (Å)	2.420	2.444	2.468	2.493	2.517	2.540
C (Å)	2.786	2.773	2.761	2.746	2.736	2.730
Area (Å^2)	6.743	6.777	6.815	6.846	6.887	6.934
Delta Width (Å)		0.0061	0.0059	0.0050	0.0042	0.0025
Percentage Width		0.29%	0.28%	0.24%	0.20%	0.12%
Delta Height (Å)		0.024	0.024	0.025	0.024	0.023
Poisson's Ratio		0.296	0.289	0.270	0.251	0.228
(30,0)	**0.1 % Strain**	**0.1-1% Strain**	**1-2% Strain**	**2-3% Strain**	**3-4% Strain**	**4-5% Strain**
A (Å)	1.400	1.410	1.420	1.430	1.440	1.450
B (Å)	2.417	2.412	2.409	2.407	2.406	2.405
C (Å)	2.800	2.830	2.860	2.890	2.920	2.950
Area (Å^2)	6.768	6.826	6.890	6.956	7.026	7.095
Delta Width (Å)		0.0050	0.0030	0.0020	0.0010	0.0010
Percentage Width		0.21%	0.12%	0.08%	0.04%	0.04%
Delta Height (Å)		0.020	0.020	0.020	0.020	0.020
Poisson's Ratio		0.217	0.174	0.145	0.119	0.104

Poisson's ratio varies with delta strain. The lateral strain is proportional to delta width. For the (20,20) CNT, delta width falls off slowly with ~20% decrease from 0.5 – 2.5% strain and ~50% decrease from 2.5 – 5% strain. The (30,0) CNT values fall off more steeply, the lateral contraction decreasing ~300% from 0.5 – 2.5% strain.

For the zig-zag CNT as the axial load is applied, the energy to increase the bond length increases with strain. Fracture strain is the strain where the energy barrier to increase bond lengths exceeds that of the energy required to break bonds. Fitting the zig-zag delta width versus strain to an exponential decay function predicts a fracture strain on the order of 10%, in agreement with other literature results.[60, 205] For brittle

materials, yield strain and fracture strain are very similar. The importance of this is two-fold. First, since CNT yield strain appears to be a direct function of chirality, it is possible to get a measure of the chiral distributions of a forest of CNTs solely from yield strain measurements. Second, only the hexagonal unit was necessary to investigate yield strain. Thus, since only a small number of atoms are required, higher fidelity methods can be used to provide more accurate yield strain values. Predicting armchair yield strain is more challenging and will be described qualitatively. With increasing strain, the energy barrier to change the bond angle increases, eventually surpassing the energy barrier for a bond angle rearrangement, making bond angle changes favorable again. The first bond angle rearrangement leads to an (*n, n-1*) configuration. This mechanism continues until the armchair achieves a zig-zag configuration (n,0).[208, 216] The CNT will go from ductile (armchair) to brittle (zig-zag) behavior. Fitting the data to a quadratic equation, the first bond rotation takes place at approximately 5% strain. Representative potentials for non-bonding, bond length and bond angle energy terms are shown below.[62, 220]

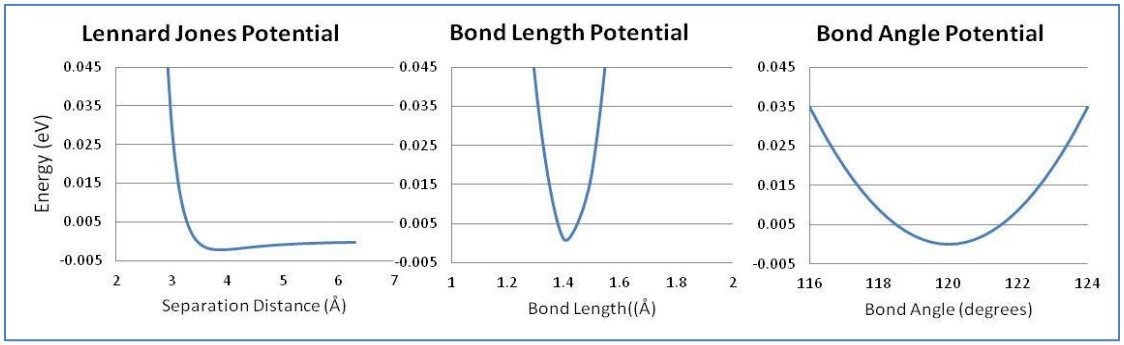

Figure 4-6: Representative curves for non-bonding, bond length and bond angle energy terms are illustrated.

99 of the 100 test cases rendered a larger Poisson's ratio for the 0-2% strain range than 3-5% strain range. The only case that did not was the (5,0) CNT with a radius of 1.98 Å (size factors dominate). The average $\Delta\nu$ ($(\nu_{0\text{-}2} - \nu_{3\text{-}5}) / \nu_{0\text{-}2}$) values for zig-zag, chiral and armchair were 45%, 30%, 19%, respectively. A subset of the data is presented in Table 4-4. Strain rate varying behavior is no doubt a factor in literature discrepancies. No mention to delta strains was found in any of the Poisson's ratio calculations in the literature.

Table 4-4: Using a 30% CNT section centered about the middle, dependence of Poisson's ratio for all CNT types based on delta strain is shown to be non-linear in the elastic region.

Test Case	Chiral Angle (Rad)	Radius (Å)	0-5% Delta Strain	0-2% Delta Strain	1-3% Delta Strain	2-4% Delta Strain	3-5% Delta Strain	$(\nu_{0\text{-}2} - \nu_{3\text{-}5}) / \nu_{0\text{-}2}$
(17,9)	0.35	9.1	0.2121	0.2587	0.2274	0.2015	0.1787	30.9%
(17,9), 0.5% Vacancy	0.35	9.1	0.2112	0.2560	0.2225	0.2005	0.1802	29.6%
(17,9), 1.5% Vacancy	0.35	9.1	0.2287	0.2656	0.2434	0.2214	0.2076	21.8%
(17,9), 3.0% Vacancy	0.35	9.1	0.2405	0.2496	0.2561	0.2525	0.2430	2.6%
(20,0)	0	7.9	0.0857	0.1423	0.0958	0.0640	0.0416	70.8%
(20,0), 0.5% Vacancy	0	7.9	0.0950	0.1532	0.1103	0.0783	0.0474	69.1%
(20,0), 1.5% Vacancy	0	7.9	0.1359	0.1927	0.1577	0.1336	0.0951	50.6%
(20,0), 3.0% Vacancy	0	7.9	0.1812	0.2303	0.2096	0.1776	0.1416	38.5%
(20,20)	0.52	13.7	0.2467	0.2941	0.2656	0.2369	0.2122	27.8%
(20,20), 0.5% Vacancy	0.52	13.7	0.2462	0.2882	0.2634	0.2387	0.2178	24.4%
(20,20), 1.5% Vacancy	0.52	13.7	0.2484	0.2778	0.2802	0.2546	0.2239	19.4%
(20,20), 3.0% Vacancy	0.52	13.7	0.2665	0.3027	0.2841	0.2576	0.2338	22.8%

4.3.3 Variations Due to Surface Defects

Surface defects change the sp^2 character of the CNT, having a direct effect on Poisson's ratio. Two types of defects, methyl functionalization and single vacancy, were evaluated. With increase in surface vacancies, Poisson's ratio increases for all chiralities. With increase in methyl functionalization, the value decreases for armchair

and increases slightly for zig-zag. Non-linear elastic strain-varying behavior is observed for both types of defects. Variations in Poisson's ratio due to the presence of surface vacancies are shown in Table 4-5.

Table 4-5: Using a 30% CNT section centered about the middle, dependence of Poisson's ratio on percentage surface vacancies for radii less than 10 Å is calculated.

Test Case	Chiral Angle (Rad)	Radius (Å)	0-5% Delta Strain	0-2% Delta Strain	3-5% Delta Strain	$(\nu_{0\text{-}2} - \nu_{3\text{-}5}) / \nu_{0\text{-}2}$
(30,0)	0	11.89	0.0946	0.1546	0.0432	0.1114
(30,0), 0.5% Vacancy	0	11.89	0.0998	0.1666	0.0459	0.1207
(30,0), 1.5% Vacancy	0	11.89	0.1337	0.1927	0.0838	0.1089
(30,0), 3.0% Vacancy	0	11.89	0.1882	0.2506	0.1345	0.1161
(60,0)	0	23.32	0.1001	0.1602	0.0456	0.1146
(60,0), 3.0% Vacancy	0	23.32	0.1144	0.1448	0.0873	0.0575
(27,16)	0.38	14.92	0.2247	0.2712	0.1911	0.0801
(27,16), 0.5 Vacancy	0.38	14.92	0.2322	0.2786	0.1994	0.0792
(27,16), 1.5% Vacancy	0.38	14.92	0.2351	0.2778	0.2097	0.0681
(27,16), 3.0% Vacancy	0.38	14.92	0.2486	0.2832	0.2264	0.0568
(20,20)	0.52	13.73	0.2467	0.2941	0.2122	0.0819
(20,20), 0.5% Vacancy	0.52	13.73	0.2462	0.2882	0.2178	0.0704
(20,20), 1.5% Vacancy	0.52	13.73	0.2484	0.2778	0.2239	0.0539
(20,20), 3.0% Vacancy	0.52	13.73	0.2665	0.3027	0.2338	0.0689
(30,30)	0.52	20.59	0.2473	0.2948	0.2143	0.0805
(30,30), 3.0% Vacancy	0.52	20.59	0.2557	0.2882	0.2245	0.0037

Poisson's ratio increases with increase in percentage surface vacancies but the effect is more pronounced for zig-zag. The 0-5% delta strain value for the (30,0) CNT doubles (0.946 to 0.1882) with 3.0% vacancies. The (60,0) CNT changes by approximately 15%, from 0.10 to 0.114. For the armchair CNT, Poisson's ratio (0-5% delta strain) increases from 0.2467 to 0.2665 with 3.0% vacancies. This can be visually explained with the hexagon unit structures in Figure 4-5. Bond angle deviations for zig-

zag CNTs move areas of high electron density closer together, making bond angle changes unfavorable. A surface vacancy removes electron density and lowers the barrier for changes in bond angles. As surface defects increase, Poisson's ratio increases for zig-zag CNTs (more pronounced at larger curvature). Armchair CNTs are ductile with bond angle changes already energetically favorable. But, removing electron density does reduce the barrier to bond angle changes, slightly increasing Poisson's ratio. As percentage surface defects increase, the strain-varying behavior is less prominent. The pristine (30,0) CNT 0-2% delta strain Poisson's ratio is ~4 times larger than the 3-5% delta strain value. But, for the (30,0) with 3.0% vacancies, the 0-2% delta strain Poisson's ratio is only about ~2 times larger than the 3-5% delta strain value. This is also observed for the (60,0) CNT. As defects increase in armchair and chiral CNTs, the difference between the 0-2% and 3-5% delta strain values decrease but is much less pronounced than for zig-zag.

Table 4-6 presents the difference in Poisson's ratio (0-5% delta strain) for 0.0% and 3.0% vacancies. As radius increases, this difference decreases. With increase in radius, the effect of vacancies on Poisson's ratio decreases.[56] For CNTs with small percentage vacancies (~3.0% or less) and larger radii (greater than ~2 nm), this data shows that a single limiting value is sufficient. The (30,30) CNT has a difference of 0.0084 and the (60,0) CNT a difference of 0.0143. This is approximately a 3.5% difference for the armchair and 15% for the zig-zag.

Table 4-6: With increase in diameter, the difference for Poisson's ratio between the pristine and 3.0% surface vacancy decreases rapidly becoming negligible.

CNT	Radius (Å)	$\nu_{Pristine}$	$\nu_{3.0\% Vacancy}$	$\nu_{3.0\% Vacancy} - \nu_{Pristine}$
Armchair				
(5,5)	3.43	0.2081	0.3747	0.1666
(10,10)	6.86	0.2348	0.2974	0.0626
(20,20)	13.73	0.2467	0.2665	0.0198
(30,30)	20.59	0.2473	0.2557	0.0084
Zig-zag				
(10,0)	3.96	0.0669	0.2296	0.1627
(20,0)	7.93	0.0857	0.1812	0.0955
(30,0)	11.89	0.0946	0.1882	0.0936
(60,0)	46.64	0.1001	0.1144	0.0143

Methyl functional groups had mixed effects. Poisson's ratio decreased for armchair but increased slightly for zig-zag. CNTs evaluated with methyl groups were small diameter and there will variation due to size and curvature effects. The changes in Poisson's ratio can be explained by the 1) change in sp^2 character of the CNT surface and 2) the steric hindrance and electron donating or accepting properties of the functional group. In both the armchair and zig-zag case, the sp^2 character of the CNT surface was decreased, leading to an increase in lateral contraction. However, with an armchair, the methyl group constrains the bond angle deviation, causing Poisson's ratio to decrease. For the zig-zag CNT, the methyl group actually decreases the resistance to bond angle deviation because it replaces a double-bond with a single bond (less repulsion). The electron donating or accepting properties of the surface functional group will have a direct effect on Poisson's ratio. For both chiralities, the strain varying behavior was observed for methyl functionalization.

Table 4-7: The effect on Poisson's ratio with methyl functionalization has competing effects, leading to mixed results.

Test Case	Chiral Angle (Rad)	Radius (Å)	0-5% Delta Strain	0-2% Delta Strain	3-5% Delta Strain	$(\nu_{0-2} - \nu_{3-5}) / \nu_{0-2}$
(10,10), 1.5% Methyl	0.52	6.86	0.2060	0.2409	0.1817	0.0592
(10,10), 3.0% Methyl	0.52	6.86	0.1799	0.2090	0.1602	0.0488
(10,10)	0.52	6.86	0.2348	0.2746	0.2067	0.0679
(10,10), 1.5% Vacancy	0.52	6.86	0.2635	0.2993	0.2400	0.0593
(10,10), 3.0% Vacancy	0.52	6.86	0.2974	0.3305	0.2777	0.0528
(10,0), 1.5% Methyl	0	3.96	0.0703	0.1093	0.0384	0.0709
(10,0), 3.0% Methyl	0	3.96	0.0770	0.1171	0.0443	0.0728
(10,0)	0	3.96	0.0669	0.0794	0.0538	0.0435
(10,0), 1.5% Vacancy	0	3.96	0.1374	0.2096	0.0738	0.1358
(10,0), 3.0% Vacancy	0	3.96	0.2296	0.2910	0.1717	0.1193

4.3.4 Variations Due to Strain Rate and Temperature Differences

Variations in strain rates and temperature have been shown to have an effect on elastic properties for pristine CNTs as well as those with surface vacancies and functionalization.[59, 177, 182, 195, 221] If the strain rate is too fast, it will produce anomalous results, such as inflated yield strain values. Table 4-8 presents Poisson's ratio for a (10,0) CNT with strain rates ranging from $0.5*10^{-6}$ ps^{-1} to 10^{-3} ps^{-1}, temperature is held constant at 300 K. If a strain rate is too high, the material system cannot fully relax and there will be unequal axial strains along the CNT. The standard deviation for the 30-70% CNT sections for the pristine (10,0) case increases from 0.0035 to 0.0078 as the strain rate decreases from $0.5*10^{-4}$ ps^{-1} to 10^{-3} ps^{-1}, with the latter two strain rates having similar standard deviation. Similar trends can be seen across the 1.5% and 3.0% test cases, with strain rates of $0.5*10^{-4}$ ps^{-1} or slower producing slightly more consistent results.

Table 4-8: The results for Poisson's ratio of a (10,0) CNT with surface vacancies from 0% to 3% is shown for multiple strain rates. Temperature was 0 K.

Test Case	Strain Rate	30% Section	40% Section	50% Section	60% Section	70% Section	80% Section
(10,0) 1.5% Vacancy	$0.5*10^{-6}$ ps^{-1}	0.1068	0.1116	0.1054	0.1006	0.1062	0.1089
(10,0) 1.5% Vacancy	10^{-5} ps^{-1}	0.1172	0.1046	0.1044	0.1024	0.1027	0.1116
(10,0) 1.5% Vacancy	$0.5*10^{-4}$ ps^{-1}	0.0868	0.1022	0.0944	0.0869	0.1034	0.1039
(10,0) 1.5% Vacancy	10^{-4} ps^{-1}	0.1207	0.1166	0.1101	0.1153	0.1206	0.1311
(10,0) 1.5% Vacancy	10^{-3} ps^{-1}	0.1406	0.1219	0.1237	0.116	0.1212	0.1446
(10,0) 3.0% Vacancy	$0.5*10^{-6}$ ps^{-1}	0.1857	0.1744	0.1886	0.168	0.1738	0.1766
(10,0) 3.0% Vacancy	10^{-5} ps^{-1}	0.1452	0.1393	0.1486	0.1256	0.1164	0.1289
(10,0) 3.0% Vacancy	$0.5*10^{-4}$ ps^{-1}	0.1685	0.1348	0.1469	0.143	0.1352	0.1455
(10,0) 3.0% Vacancy	10^{-4} ps^{-1}	0.1429	0.0964	0.1172	0.1242	0.1245	0.1353
(10,0) 3.0% Vacancy	10^{-4} ps^{-1}	0.1535	0.1197	0.1338	0.1266	0.1177	0.1309
(10,0)	$0.5*10^{-4}$ ps^{-1}	0.046	0.0519	0.0432	0.0475	0.0437	0.0503
(10,0)	10^{-4} ps^{-1}	0.0599	0.0544	0.05	0.0425	0.0491	0.0568
(10,0)	10^{-3} ps^{-1}	0.0513	0.058	0.0598	0.0472	0.0565	0.0700

A second method to identify an invalid strain rate is anomalous behavior in the vicinity of the yield strain. Table 4-9 presents data for delta strains from 0 – 12% strains in 2% increments at 300 K. If the strain rate is too fast, the strain varying behavior will not be as smoothly decreasing because the material system has not had time to fully equilibrate. Further, as stated earlier, it will also produce yield strains that are too large. The pristine CNT with the slowest strain rate ($0.5*10^{-4}$ ps^{-1}) smoothly decreases across the delta strains with an expansion occurring around 5%. This value is in line with the results of the hexagonal unit for the (30,0) CNT. The other two faster strain rates are more erratic. For the 10^{-3} ps^{-1} strain rate, Poisson's ratio decreases to 0.0152 and then increases to 0.0239 before decreasing again. The slowest three strain rates for the (10,0) 1.5% and 3.0% vacancy cases also exhibit a smooth decay across 0 – 5%. The faster two (10^{-4} ps^{-1} and 10^{-3} ps^{-1}) strain rates both portray oscillating behavior across

the 0-5% decrease. This substantiates that strain rates on the order of $0.5*10^{-4}$ ps^{-1} or slower are sufficient.

Table 4-9: The results for Poisson's ratio of a (10,0) CNT with surface vacancies from 0% to 3% is shown for multiple strain rates, at a temperature of 300 K. Delta strains from 0-2% to 10-12% were evaluated to identify any anomalous behavior in the vicinity of the yield strain.

Test Case	Strain Rate	0-2% ΔStrain	1-3% ΔStrain	2-4% ΔStrain	3-5% ΔStrain	4-6% ΔStrain	6-8% ΔStrain	8-10% ΔStrain	10-12% ΔStrain
(10,0) 1.5% Vacancy	$0.5*10^{-6}$ ps^{-1}	0.1201	0.1139	0.1066	0.093	0.1102	0.0372	0.2182	0.197
(10,0) 1.5% Vacancy	10^{-5} ps^{-1}	0.1961	0.1645	0.1039	0.087	0.1018	0.0539	0.2174	0.0633
(10,0) 1.5% Vacancy	$0.5*10^{-4}$ ps^{-1}	0.1576	0.1001	0.0693	0.0174	0.045	0.0357	0.2118	0.1362
(10,0) 1.5% Vacancy	10^{-4} ps^{-1}	0.1773	0.1345	0.1379	0.0608	0.0234	0.0761	0.1681	0.1088
(10,0) 1.5% Vacancy	10^{-3} ps^{-1}	0.1772	0.1428	0.1604	0.1149	0.0714	0.1107	0.0449	0.2527
(10,0) 3.0% Vacancy	$0.5*10^{-6}$ ps^{-1}	0.2721	0.2345	0.2203	0.1921	0.1233	0.1138	0.13	0.5033
(10,0) 3.0% Vacancy	10^{-5} ps^{-1}	0.2401	0.1859	0.1346	0.075	0.0726	0.0762	0.1257	0.5734
(10,0) 3.0% Vacancy	$0.5*10^{-4}$ ps^{-1}	0.2154	0.2069	0.1652	0.1333	0.1058	0.1014	0.058	0.3899
(10,0) 3.0% Vacancy	10^{-4} ps^{-1}	0.1808	0.1348	0.1281	0.1401	0.0955	0.1058	0.1044	0.2475
(10,0) 3.0% Vacancy	10^{-4} ps^{-1}	0.2185	0.1176	0.1054	0.1484	0.1065	0.0965	0.0769	0.0716
(10,0)	$0.5*10^{-4}$ ps^{-1}	0.0999	0.0646	0.0316	0.0098	-0.0063	-0.0081	-0.0318	-0.0382
(10,0)	10^{-4} ps^{-1}	0.0999	0.0818	0.0613	0.0458	0.0255	-0.04	-0.0224	-0.027
(10,0)	10^{-3} ps^{-1}	0.0927	0.0456	0.0152	0.0239	0.0213	-0.0132	-0.0284	-0.0395

Figure 4-7 is a plot of Poisson's ratio values for the (10,0) CNT with 1.5%vacancies for three strain rates. The top two in the legion are considered sufficiently slow whereas the last (10^{-3} ps^{-1}) is not. The two slower strain rates follow the same trend, decreasing to 7% strain, incurring an energy releasing molecular movement increasing Poisson's ratio and then decreasing again. The fast strain rate, 10^{-3} ps^{-1}, is more optimistic than the other two, decreasing to about 9% strain for the energy releasing mechanism and over-shooting the increase in expansion.

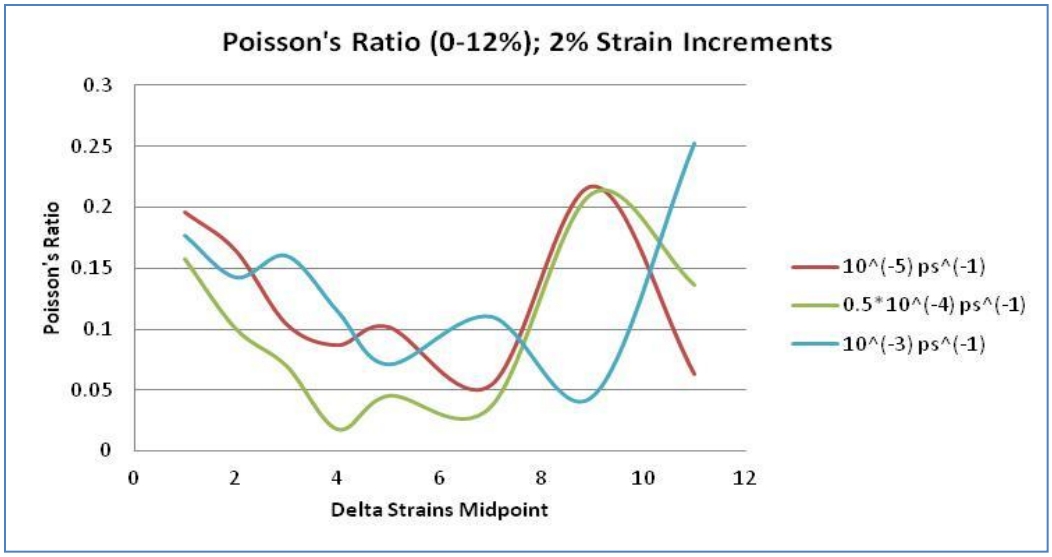

Figure 4-7: Strain rates are that are too fast exhibit erratic behavior, deviating from the behavior exhibited by slower, more appropriate strain rates.

Table 4-10 provides insight into temperature effects from 0 K to 1600 K on Poisson's ratio for pristine and 1.5% and 3.0% surface vacancy. All strain rates used were sufficiently slow. 2400 K was also evaluated, the value increasing to ~0.3 for the 1.5% case and holding constant at ~0.5 for the 3.0% test case. Values for middle sections from 50 – 70% were fairly consistent. With increase in temperature, there is a slight decrease in Poisson's ratio from 0 K to 300 K and an increase from 300 K to 1600 K.[182, 222] The same trend is visible in pristine, 1.5% or 3.0% defects although Poisson's ratio increases more with a higher percentage of surface vacancies. For the pristine and 1.5% test cases, contraction fluctuates +/- 30% with temperature. With the 3.0% case, however, rather than remaining fairly constant in the range from 800 K to 1600 K, it doubles.

Table 4-10: Poisson's ratio decreases from 0 – 300 K and then increases from 300 K to 1600 K.

Test Case	Temp (K)	Strain Rate	0-5% Strain 50% Section	0-5% Strain 60% Section	0-5% Strain 70% Section	0-2% Strain 50% Section	3-5% Strain 50% Section
(10,0)	0	$0.3*10^{-4}$ ps^{-1}	0.0669	0.0669	0.0669	0.1057	0.0351
(10,0)	300	$0.5*10^{-4}$ ps^{-1}	0.0432	0.0475	0.0437	0.0999	0.0098
(10,0)	800	$0.5*10^{-4}$ ps^{-1}	0.0566	0.0865	0.0604	0.0628	-0.0027
(10,0)	1600	$0.5*10^{-4}$ ps^{-1}	0.0428	0.0791	0.0707	-0.0333	0.0384
(10,0) 1.5% Vacancy	0	$0.3*10^{-4}$ ps^{-1}	0.1344	0.134	0.1388	0.2096	0.0738
(10,0) 1.5% Vacancy	300	10^{-5} ps^{-1}	0.1044	0.1024	0.1027	0.1961	0.087
(10,0) 1.5% Vacancy	800	10^{-5} ps^{-1}	0.1495	0.1655	0.1291	0.0633	0.1343
(10,0) 1.5% Vacancy	1600	10^{-5} ps^{-1}	0.1568	0.1431	0.1606	0.1662	-0.1014
(10,0), 3.0% Vacancy	0	$0.3*10^{-4}$ ps^{-1}	0.1778	0.1972	0.1853	0.291	0.1717
(10,0), 3.0% Vacancy	300	10^{-5} ps^{-1}	0.1486	0.1256	0.1164	0.2401	0.075
(10,0), 3.0% Vacancy	800	10^{-5} ps^{-1}	0.1734	0.2067	0.1788	0.1826	0.2517
(10,0), 3.0% Vacancy	1600	10^{-5} ps^{-1}	0.5279	0.4737	0.4864	0.7314	-0.0254

4.4 Conclusion

Poisson's ratio has a wide array of predicted values in the literature, from 0.06 to 1.414.[187] This analysis achieved a systematic evaluation of discrepancies based on chirality, delta strains, percentage surface defects, temperatures and strain rates. Poisson's ratio over a delta strain of 0 – 5% has a limiting value of 0.10 for zig-zag and 0.25 for armchair (diameters $>$ 2 nm, surface defects $\leq$ 3.0%). Poisson's ratios less than 0.125 are regarded as brittle materials with bond angle deviation from equilibrium being energetically unfavorable. [202, 203] Zig-zag CNTs are brittle materials while armchair are more ductile. For both chiralities, Poisson's ratio exhibits a strain varying, nonlinear elastic behavior. The strain varying behavior was investigated. For zig-zag, a 1% delta strain centered about 4% strain was 45% less than 1% delta strain centered about 1% strain. For armchair, the decrease between the 4% and 1% strain was less at 19%. Procedurally, with such small variances in delta width, it is important to implement

calculations with the least error possible. A method to calculate radii was proposed. When calculating Poisson's ratio, it is important to use a large section of the CNT, at least 30% and possibly up to 100%. Surface defects of vacancies and methyl function groups were considered as well. Both vacancies and methyl groups change the sp^2 character of the CNT surface, which has a direct bearing on Poisson's ratio. For vacancies, Poisson's ratio increased for all chiralities but the effect was more pronounced for zig-zag. As vacancies are created in zig-zag CNTs, the energy barrier to bond angle rotation is decreased, increasing the value of Poisson's ratio. The lateral contraction value of armchair CNTs did increase but only slightly. As armchair already had a ductile type behavior (energetically favorable bond angle deviations), the vacancy had less of an effect. For CNTs greater than 2 nm, Poisson's ratio differences between pristine CNTs and 3.0% defects is very small. With methyl functional groups, the lateral contraction value increased slightly for zig-zag and increased for armchair. Functional groups can be explained by splitting their effects in two pieces: 1) the change in sp^2 character of the surface and 2) the steric hindrance and electron donating or accepting properties of the functional group. In both armchair and zig-zag, the sp^2 character was decreased, about a third that of a vacancy. For the armchair, the methyl group increases the energy to bond angle deviation, which causes Poisson's ratio to decrease. For the zig-zag CNT, the methyl group single bond replaces a more electron dense double bond, slightly decreasing the non-bonding interaction as the sides of the hexagon are forced together under axial tension. The summation of changes to zig-zag led to a slight increase in Poisson's ratio. A strain rate of $0.5 * 10^{-4}$ ps^{-1} or slower was identified sufficient to produce consistent results. As temperature increases from 0 to

300 K, Poisson's ratio decreases slightly. As temperature increases from 300 K to 1600 K, it increases. This is directly proportional to the temperature dependent behavior of the bond length stretching and bond angle hinging constants.[223] Yield strength was modeled as an exponential decay of chiral angle, on the order of 10% for pristine CNTs, in good agreement with experimental and computational results.[60, 206, 207]

This analysis identifies chiral angle and delta strain as critical variables to predict Poisson's ratio, one the five properties required to understand behavior in the elastic region. Further, a direct relationship between yield strain and chiral angle (armchair or zig-zag) is proposed, extending understanding into the plastic region as well. This relationship directly links a continuum level material behavior to atomic behavior. Because Poisson's ratio was shown to be modeled by the hexagon unit structure of only a few atoms, it would be possible to use higher fidelity models to produce more accurate results of the strain varying behavior. Future work includes the development of descriptors and quantitative structure property relationships for the accurate prediction of yield strain.

CHAPTER 5

IMPROVING LOAD TRANSFER IN MULTI-WALLED CNTS

Cross-links between inner and outer walls of multi-walled carbon nanotubes are believed to increase load transfer and nanotube effectiveness for reinforcing composites. A cross-link, however, is a defect and will simultaneously decrease the stiffness of both walls participating in the cross-link. To investigate changes in Young's modulus of individual double-walled nanotubes (DWCNTs) as a function of cross-link density and type, molecular dynamics (MD) simulations are employed to evaluate strain coupling, corresponding load transfer from outer to inner walls and changes to the elastic moduli. Results show inter-wall sp^3 bonds and interstitial carbon atoms can increase load transfer between DWCNT walls with inter-wall sp^3 bonds being most effective. The maximum effective modulus (outer wall only, considers only outer wall cross-sectional area) increase is limited to about 25% for the small-diameter, short DWCNTs as the defects also decrease the stiffness of each of the nanotube walls. Quantitative structure property relationships (QSPR) can be used to pinpoint the optimal load transfer by balancing increase in strain coupling with the decrement to wall stiffness caused by inter-wall linkages.

5.1 Introduction

Carbon nanotubes (CNTs) are considered to be the ultimate mechanical fillers for reinforcement of polymer composites.[2, 33, 68] The small size, low density, large aspect ratio, and outstanding mechanical, electronic, and thermal properties achievable for individual carbon nanotubes make them attractive candidates for composites in diverse applications.[2, 67, 179]

Mechanical properties of many different types of CNT-polymer composites have been studied both experimentally[2] and theoretically.[67, 224] However, composite mechanical property improvement consistent with predictions has not come to fruition, regardless of type and volume fraction of CNTs used for reinforcement.[2, 67] Examples are certain CNT-epoxy composites[14, 68] and CNT-plastic composites that are melt-processed.[2, 152, 154] To optimize mechanical properties of CNT reinforced composites, there are four factors to consider: aspect ratio, homogeneity of nanotube dispersion, interfacial CNT-polymer stress transfer and alignment.[2, 152] This analysis focuses on interfacial-CNT polymer stress transfer through stress transfer to inner walls of the multi-walled CNTs. While the reason for not achieving high mechanical properties can be related to both the lack of efficient polymer-CNT interfacial stress transfer and poor dispersion of CNTs within the polymer matrix[2, 69, 225], it has been proposed[68, 226] that cross-links between inner and outer walls of multi-walled carbon nanotubes (MWCNTs) would increase CNT-polymer composite mechanical properties for instances where these former problems are solved. The low force constant for shear between the walls of MWCNTs[227-230] provides a limitation on MWCNT use as reinforcing agents, since tensile strains on outer walls are not transferred well to inner walls unless the MWCNTs are very long. The use of cross-links is proposed to help address this problem. Using descriptors and QSPRs developed for single-walled CNTs (SWCNT) earlier in this dissertation, it is possible to model the Young's modulus decrement to the walls as the cross-link percentage is increased. In conjunction with a model for load transfer, it would be possible to identify an optimal loading of cross-links to increase load transfer while minimizing decrease in individual wall stiffness.

Motivated by experimental studies demonstrating that electron[55, 231, 232], ion[233], or neutron[234] irradiation methods induce the appearance of defects and cross-links between layers in graphite or between the inner and outer walls of MWCNTs, molecular dynamics (MD) simulations have been used to study the load transfer behavior of MWCNTs having different cross-link structures under different load conditions. Xia and Curtin[235] studied the dependence of inner wall pullout force and friction for a double-walled nanotube (DWCNT) on the type of inner wall end termination. Xia et al[236] investigated the transverse shear, uniaxial compression, and pullout loading in DWCNTs with inter-wall sp^3 bonds. Huhtala[226] calculated the forces needed to start the sliding of the inner wall in DWCNTs having different defect types. Peng[55] performed MD simulations to study the load transfer in DWCNTs with Frenkel pair[237] defects. Shen[238] studied load transfer between inner and outer walls of DWCNTs under tensile and compressive loads, compared the results for capped and uncapped CNTs, and studied one case where the defects are interstitial carbon atoms. Song and Zha[239] studied the mechanical properties of DWCNTs having a regular pattern of sp^3 bonds between their walls. Byrne[15] showed that MWCNTs with inter-wall sp^3 bonding are stronger than single-walled nanotubes (SWNTs) with the same number of intra-wall defects. All of this work demonstrates significant improvements in load transfer between nanotube walls as a result of cross-linking.

While pullout and sliding forces are important when fracture of the inner or outer wall takes place, previous work has not systematically studied how inter-wall bridging influences the load transfer before CNT rupture. This study investigates how tensile strain is transferred from outer to inner walls of DWCNTs for different densities of two

different types of cross-linking defects, namely, interstitial carbon and direct inter-wall sp^3 bonding between the walls called “IC” and “SP^3” for short, respectively. The choice of these two types of defects was made based not only on previous theoretical work but also on recent experimental results showing the possibility of having MWCNTs with either type of defect. Urita[232] reported the observation of interstitial-vacancy pair defects in DWCNTs at temperatures below 400 K. Kanasaki[240] showed that femtosecond laser excitation is able to create meta-stable sp^3-bonded carbons between layers of graphite. In a recent theoretical paper, Muniz[241] demonstrated the stability of sp^3 bonding between the layers of MWCNTs. It is important to note that the interstitial carbons in IC defects also form sp^3 bonds with adjacent atoms. However, the SP^3 name is kept for the second defect since the walls are directly connected via a sp^3 bond rather than through an additional atom. While other types of defects can also be formed[226, 237], IC and SP^3 defects represent two main possibilities.

It will be shown that both types of defects significantly improve load transfer between the walls of the DWCNTs, with the inter-wall SP^3 the more efficient of the two. It will be verified that if the defects substantially deform the CNT hexagon structure, CNT stiffness decreases. Randomly adding hydrogen atoms to the surface of a pristine DWCNT simulates the effects of pyramidalization[242] of the corresponding outer wall carbons due to the functionalization or chemical bonding between a polymeric matrix and the DWCNT. In this case, the stiffness of the DWCNT slightly decreases with the increase in the number of these pyramidalization surface sites. Finally, a simple mechanical model for load transfer between the walls of the DWCNT will be developed and used to analyze the variation of Young’s modulus.

5.2 Computational Method and Description of Systems

The adaptive intermolecular reactive empirical bond order (AIREBO) potential was used for molecular dynamics (MD) simulations. It extends the second generation of the reactive empirical bond order (REBO) potential, also known as the Brenner-Tersoff potential, to include torsional and pair-wise van der Waals interactions.[146] The REBO potential is well known to accurately describe carbon-carbon and hydrocarbon molecular short range interactions when allowing for bond breaking, formation and rehybridization.[18]

The method of load transfer from the outer to the inner wall of a DWCNT is shown in the Figure 5-1. Arrows indicate the tensile forces are only applied to the outer walls and represent interfacial stresses from a surrounding strained polymer matrix (not shown). The effect of this applied strain on the inner wall is measured.

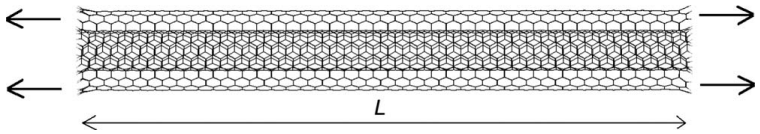

Figure 5-1: The mechanism of load transfer shows the axial force applied only to the outer wall while the inner wall is allowed to move freely.

Two DWCNTs of different chiralities were selected for this study: (4,0)@(13,0)DWCNT and (5,5)@(10,10)DWCNT, referred to as DWCNT-ZZ and DWCNT-ARM, respectively. The first and second pairs of indices for each CNT type describe the inner and outer CNTs, respectively. These DWCNTs satisfy the heat of formation stability rule (m,0)@(m+9,0) and (m,m)@(m+5,m+5) for zigzag and armchair tubes, respectively.[40] The total length was 100 Å with 1,800 and 2,500 total carbon atoms for DWCNT-ZZ and DWCNT-ARM, respectively. For every CNT and for both

types of defects, six cases of randomly distributed defect loadings were studied: 0, 2, 25, 50, 75 and 100 defects. For 2 defects, the separation distance was greater than 50 Å, half the length of the CNT. Defining the fraction of defects (f) as the ratio of cross-linking defects divided by the total number of atoms of the system[236], the largest f in this study is smaller than 5.6%. The corresponding fraction of defects (percentage defects) is provided in the following table.

Table 5-1: The number and corresponding fraction of defects for the DWCNT-ZZ and DWCNT-ARM is presented.

	DWCNT-ZZ	DWCNT-ARM
Number of Defects	Fraction of Defects	
0	0.0%	0.0%
2	0.1%	0.1%
25	1.4%	1.0%
50	2.8%	2.0%
75	4.2%	3.0%
100	5.6%	4.0%

These values were selected to be consistent with the experimental values in Peng's analysis, which varies from 0.02% to 3.75%.[55] Figure 5-2 is a cross-sectional view of the 0 K fully relaxed atomic structures with the interstitial carbon bonds (on left) and the SP^3 direct inter-wall bonds. Figure 5-2 illustrates a cross-section of atomic structures for both IC and SP^3 defects with no axial tension applied equilibrated at 0 K.

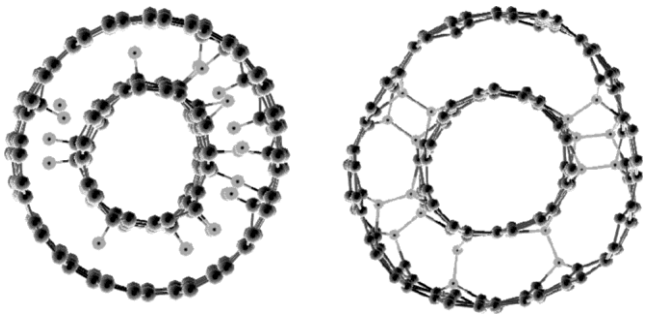

Figure 5-2: Interstitial carbons (IC) are presented on the left and inter-wall carbons (SP^3) are on the right.

Tensile strain was applied by moving the carbons at both ends of the outer wall away from the CNT 0.1 Å (for a total of 0.2 Å, 0.2% strain) and fixing them in place for a new length of 100.2 Å. The entire structure was allowed to fully relax to the low energy conformation and the process of stretching 0.2 Å and structure relaxation was repeated 51 times for a total of 10% tensile strain.[60, 61, 207] A total of 1,122 molecular dynamics simulations were carried out. A time step of 0.5 fs was used, each strain was relaxed 100 ps (strain rate = $2*10^{-5}$ ps^{-1}) and the Berendsen[149] thermostat was employed. At each step, the total energy and displacements of the inner and outer walls were compiled.

To study the effect of surface roughness on load transfer, the outer wall of the DWCNT-ARM was randomly functionalized with six loadings of hydrogen atoms: 0, 2, 25, 50, 75 and 100. The fraction of carbons that were functionalized became sp^3 hybridized (Figure 5-3). Tensile strain simulations were carried out in the same manner described earlier but only to 1% strain.

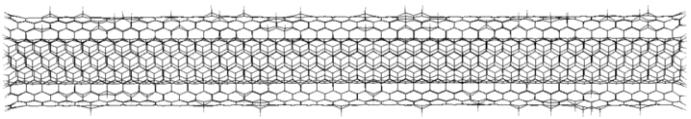

Figure 5-3: Hydrogen functionalized DWCNTs shows the non-^{sp2} character of the surface.

Determining Young's modulus via the second derivative of the strain energy density is as follows.[67]

$$Y = \frac{1}{V}\frac{\partial^2 E}{\partial \varepsilon^2} \tag{47}$$

$$\frac{2}{AL_0}E = Y\varepsilon^2 \tag{48}$$

E is the strain energy, ε the tensile strain, *V* is the volume (length * area) of the CNT, *Y* is Young's modulus, *A* is the cross-sectional area equal to $2\pi Rh$ (*R* is the cross-section radius and *h* = 0.34 nm as the wall thickness typically considered in theoretical and experimental Young's modulus analyses.[219] This method is solved via plotting strain energy versus strain and curve-fitting the second degree polynomial to the data. For this study, the effective Young's modulus is defined as Young's modulus only on the outer wall. Since axial tension was applied solely to the outer wall, only the cross-sectional area of the outer wall was included in the stiffness calculation.

A quantitative structure property relationship (QSPR) for load transfer will be built. Previous QSPRs in this dissertation provide models for the stiffness of the individual walls. Using both QSPRs together will facilitate the identification of an equilibrium point, where intrinsic decrease to wall stiffness is balanced by load transfer increase. QSPRs are easily adjusted with experimental data, decreasing the barrier to computational-experimental directed research. QSPRs can be updated with high fidelity models,

where necessary, through descriptors without the need for simulations of prohibitive numbers of atoms. QSPRs make it easier to connect multiple simulations of smaller systems (piece-wise) through descriptors as opposed to having to run a very large simulation of the entire system.

5.3 Results and Discussion

Load transfer from outer to inner walls of both DWCNTs was analyzed by inspection of inner wall strain variation as a function of applied tensile strain to the outer wall. Results of the outer-to-inner load transfer strain curves for both types of defects specific to each DWCNT are shown in Figure 5-4. The interstitial carbons (IC) are in the first column and SP^3 inter-wall in the second.

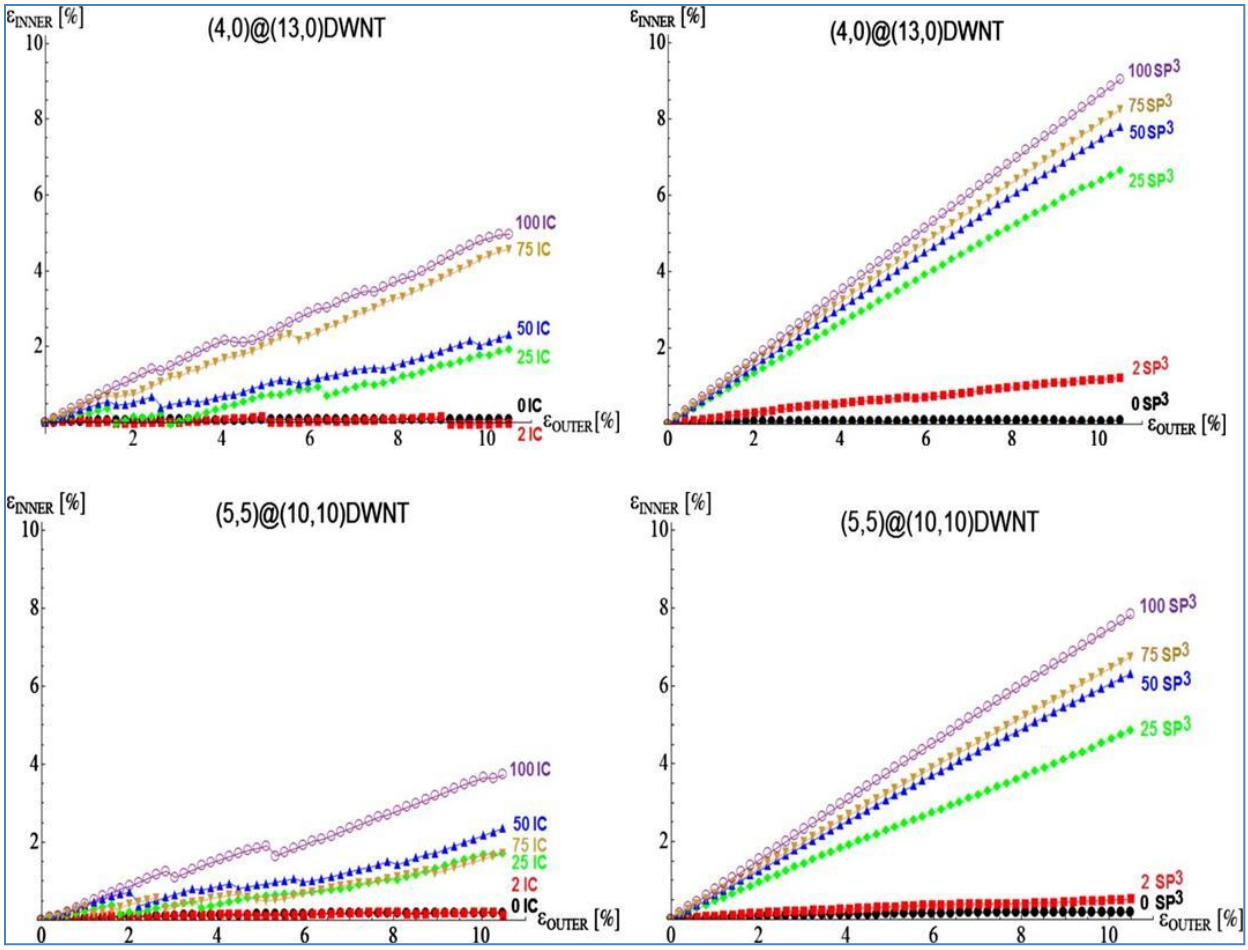

Figure 5-4: The outer wall to inner wall strain transfer curves for interstitial carbon (IC) and inter-wall (SP^3) linkage types are shown in the first and second columns, respectively.

While both SP^3 and IC cross-link types provide major increase in load transfer for the DWCNTs, the degree of stress transfer for SP^3 defect type is about twice as effective as the IC type. Load transfer in DWCNT-ZZ is more efficient than DWCNT-ARM. For DWCNT-ZZ, the molecular bonds are parallel to the applied tensile force whereas with the DWCNT-ARM, the nanotube bonds are at 30 degree angle to the applied force. The component of the force providing work in DWCNT-ARM is the axial force * cos(30 degrees) = 0.866 * force. This is observed easily in column two of Figure 5-4 for 100 SP^3 defects. For DWCNT-ZZ, the inner strain is 9.1 whereas it is 7.75 for

DWCNT-ARM, a ratio of 0.85. Differences between the defect types are a function of the energy barriers to deformation and are illustrated in Figure 5-5.

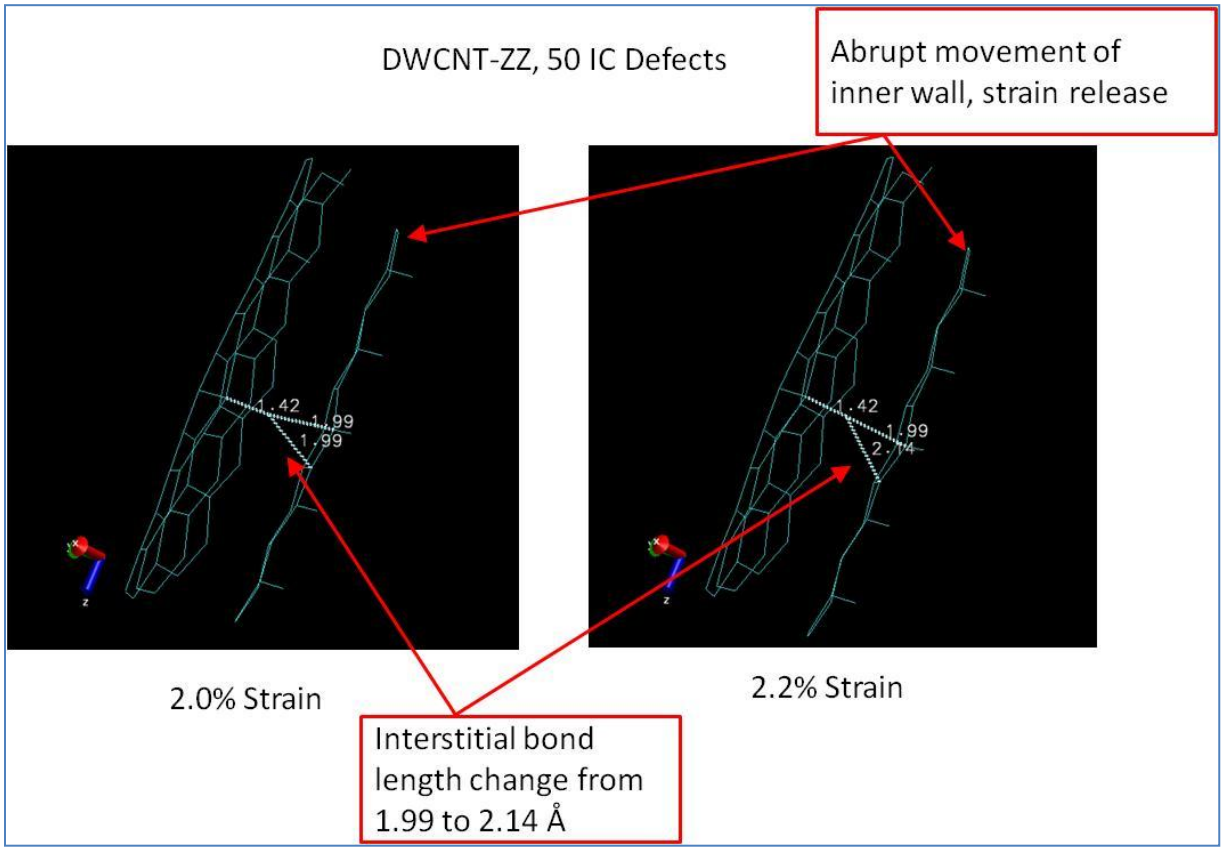

Figure 5-5: As a tensile strain is applied to the DWCNT-ZZ with IC linkage types, abrupt movements of the inner wall occur at points along the strain transfer curve, due to relative changes in energy barriers for specific strain releasing mechanisms.

The migration energy barrier of an interstitial atom is smaller than that of other defect types.[231] It is expected that overcoming the energy barriers to move the interstitial carbon (IC) would be less than that of increasing bond lengths over the inner wall. The IC carbon bonds are already strained. The figure on the left has bond lengths of 1.42 Å, 1.99 Å and 1.99 Å. At approximately 2.0% strain, the energy barrier to increase the bond length of the IC defect is less than that of increasing the bond lengths along the inner wall. There is an abrupt increase of IC bond length to 2.14 Å from 1.99

Å facilitating a sudden movement of the entire inner wall, allowing the CNT inner wall to contract slightly, releasing strain energy. This oscillating behavior between increasing the strain on the inner wall and increasing the strain on the IC bond continues throughout the application of axial tension and are identified as the dips on the left hand column of Figure 5-4. For SP^3 defects, the outer-to-inner load transfer strain curves are linear, indicating cost of breaking the SP^3 bonds is higher than increasing the strain to the walls, up to 10% outer wall strain studied in this analysis.

Strain transfer gain (defined as the following equation) is utilized to compare the change in degree of strain transfer between the outer and inner walls for the various loadings and types of defects.

$$S_{\bar{\epsilon}} = \frac{d\epsilon_{Inner}}{d\epsilon_{Outer}} \tag{49}$$

The variable $\bar{\epsilon}$ is the maximum strain value on the outer wall for the calculation. Variables ϵ_{Inner} and ϵ_{Outer} are the strains on the inner and outer walls, respectively. In this case, $\bar{\epsilon}$ is $\leq$ 1%, before the first discontinuity in the IC defect type (oscillating behavior described above). Table 5-2 presents the strain transfer gain values in terms of number of defects and percentage defects for both DWCNTs. As expected, for both types of defects, the DWCNT-ZZ shows a slight improvement in $S_{\bar{\epsilon}}$ compared to the DWCNT-ARM. The inter-wall bonds (SP^3) are more effective than the interstitial carbon (IC) for all defect loadings. At approximately 1-1.5% defects, there are large improvements in strain transfer gains for both types of defects but SP^3 defects realize about twice the delta improvement. Beyond 1-1.5%, the delta strain transfer gain is much smaller. For example, from 0.1% to 1.4% defects in DWCNT-ZZ, the

improvement for IC and SP^3 types are 0.16 and 0.50, respectively. From 1.4% to 2.8%, the improvement for IC and SP^3 types are 0.14 and 0.10, respectively.

Table 5-2: The strain transfer gain for both DWCNT types increases with number of defects but increases much faster for the inter-wall SP^3 bond.

		DWCNT-ARM		DWCNT-ZZ		
Number Defects	% defects	IC	SP^3	% defects	IC	SP^3
0	0.0%	0.05	0.05	0.0%	0.05	0.05
2	0.1%	0.07	0.08	0.1%	0.10	0.15
25	1.0%	0.22	0.47	1.4%	0.26	0.65
50	2.0%	0.39	0.62	2.8%	0.40	0.75
75	3.0%	0.35	0.65	4.2%	0.51	0.80
100	4.0%	0.40	0.75	5.6%	0.60	0.86

Figure 5-6 shows $S_{\leq 1\%}$ for the four permutations of DWCNT and defect types. Strain transfer gain improves as percentage defects are increased for both types of DWCNTs. However, the rate of strain transfer gain is maximized at approximately 1.5% defects for both defect types.

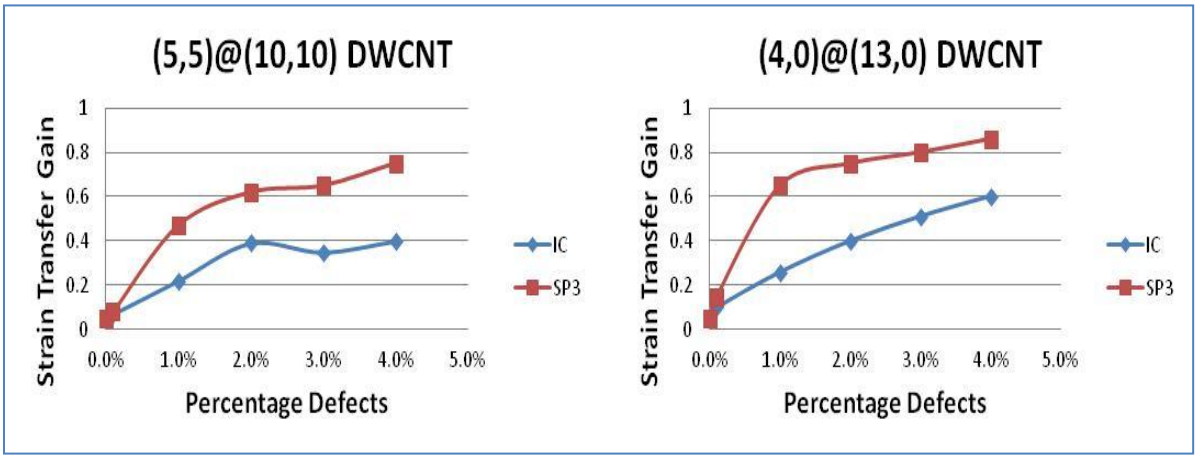

Figure 5-6: The rate of strain transfer rate relative to the number of defects for the DWCNT-ARM is shown on the left while the DWCNT-ZZ is illustrated on the right.

Effective Young's Modulus results for the DWCNT-ARM and DWCNT-ZZ are in Table 5-3 and Table 5-4. Effective Young's modulus was calculated from the second derivative of the strain energy (equations (47) and (48)) for outer wall strains up to 1%, considering only the cross-sectional area of the outer wall. The maximum rate of change in effective Young's modulus can be seen at about 1–1.5% for both DWCNT-ZZ and DWCNT-ARM. Effective Young's modulus improvement from 1-2% IC and SP^3 defect types in DWCNT-ARM is 9.3% and 7.8%, respectively. From 2-3%, the improvement is 4.3% and 1.0% for the IC and SP^3 types, respectively. For DWCNT-ZZ, the improvement to effective Young's modulus starts to decrease for SP^3 defect type beyond 1.4%. The maximum improvement to effective Young's modulus is ~30% and 7-15% for DWCNT-ARM and DWCNT-ZZ, respectively.

Table 5-3: Young's modulus (GPa) for the DWCNT-ARM for both IC and SP^3 linkage types have a maximum rate of improvement at approximately 1-1.5%.

		IC		SP^3	
Number Defects	% Defects	Young's Modulus	% Improvement	Young's Modulus	% Improvement
0	0.0%	870		870	
2	0.1%	880	1.1%	885	1.7%
25	1.0%	957	10.0%	1040	19.5%
50	2.0%	1038	19.3%	1111	27.7%
75	3.0%	1070	23.0%	1120	28.7%
100	4.0%	1125	29.3%	1132	30.1%

Table 5-4: Young's modulus (GPa) for the DWCNT-ZZ for both IC and SP^3 linkage types have a maximum rate of improvement at approximately 1-1.5%.

		IC		SP^3	
Number Defects	% Defects	Young's Modulus	% Improvement	Young's Modulus	% Improvement
0	0.0%			1000	
2	0.1%	1015	1.5%	1030	3.0%
25	1.4%	1040	4.0%	1155	15.5%
50	2.8%	1060	6.0%	1132	13.2%
75	4.2%	1062	6.2%	1100	10.0%
100	5.6%	1072	7.2%	1070	7.0%

The following figure illustrates the percentage improvement to effective Young's modulus for the DWCNTs. The maximum rate of change for improvement to effective Young's modulus is approximately 1-1.5% for both types of DWCNTs. This directly corresponds to the position of maximum rate of change of strain transfer gain (Figure 5-6).

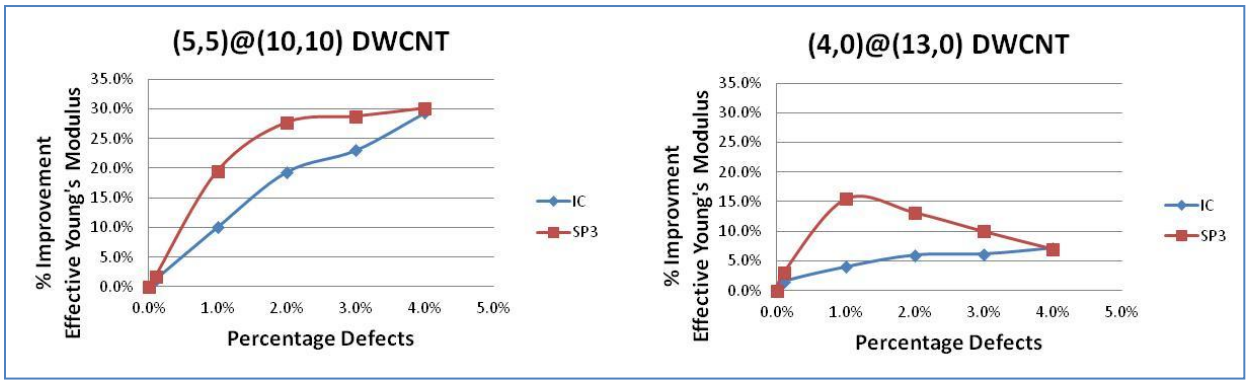

Figure 5-7: Effective Young's modulus has a maximum rate of change of improvement at approximately 1-15.% for both types of DWCNTs.

A simple mechanical model is developed to analyze the results. With no cross-links, an external force applied to the outer wall of the DWCNT will cause a strain inversely proportional to its stiffness. With the increase in cross-links, that external force is divided across both the outer and inner walls, producing respective outer and

inner walls strains inversely proportional to each CNT's stiffness. Let *F* be the resultant external force on the outer wall, then:

$$F = F_{Outer} + F_{Inner} \tag{50}$$

The next force on the outer wall is F_{Outer} while F_{Inner} is the net force on the inner wall. Let the axial change in length for the inner and outer CNT be Δ_{Inner} and Δ_{Outer}, respectively. In the elastic region, Hooke's law holds and the spring constants are set as k_{Inner} and k_{Outer}. Substituting the definition of strain transfer gain for Δx_{Inner} (equation (49)) yields the following:

$$F = k_{Outer}\Delta x_{Outer} + k_{Inner}\Delta x_{Inner} \tag{51}$$

$$\Delta x_{Inner} = S_{\bar{\epsilon}}\Delta x_{Outer} \tag{52}$$

$$F = k_{Outer}\Delta x_{Outer} + k_{Inner}S_{\bar{\epsilon}}\Delta x_{Outer} \tag{53}$$

$$F = (k_{Outer} + k_{Inner}S_{\bar{\epsilon}})\Delta x_{Outer} \tag{54}$$

If the dependence of the spring constants on the defect concentration was negligible, the maximum effective Young's modulus would correspond to the maximum strain gain transfer $S_{\bar{\epsilon}}$, which would be 1 since the inner and outer walls would be considered a parallel association of equally strained springs.[55] However, the spring constants and stress gain transfer are a function of both the type and number of defects. As the strain gain transfer increases due to the defect loading, the spring constants of the individual walls decrease, leading to a limited increase in moduli. This is most clearly exhibited in the effective Young's modulus of the (4,0)@(13,0) in which the value increases to a maximum at approximately 20 defects or 1-1.5%. The effect of

the decrease in spring constants overcomes the increase in strain transfer gain. While strain transfer is still increasing, the rate of change (second derivative) is decreasing.

To test this assumption of decreased stiffness of the individual walls of DWCNT-ZZ with increasing defect concentration, another set of MD tensile strain simulations were executed. The SP^3 defect was used and inner and outer walls were equally stretched. Since both walls of the CNT were stretched, the cross-sectional area of both walls was used in the calculation. Figure 5-8 unmistakably shows a linear decrease in stiffness with increase in defect concentration. Thus, the spring constants are decreasing linearly with increase in defect concentration. Structural changes due to incorporation of defects are due to the decrease in moduli observed in Figure 5-7.

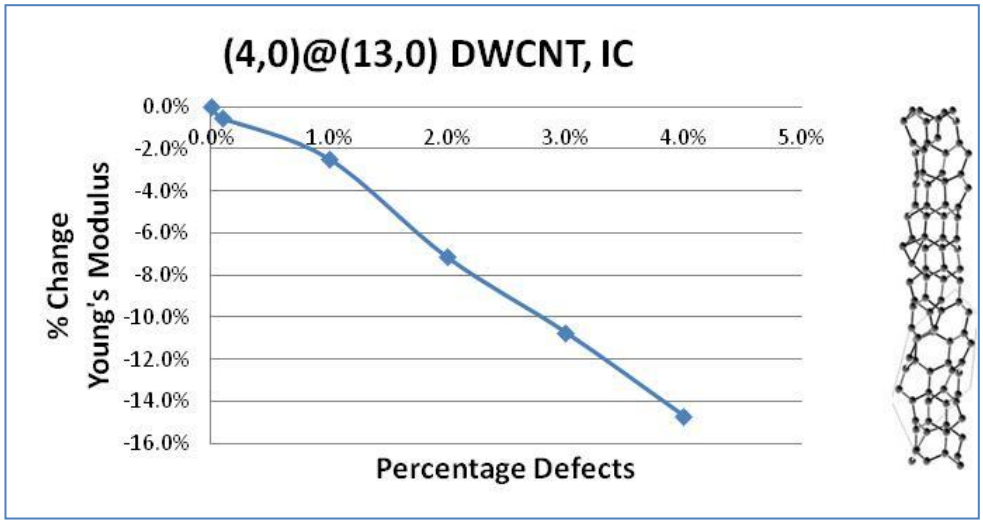

Figure 5-8: Young's modulus, using both walls, shows a linear decrease in stiffness as percentage surface vacancies is increased.

To identify which structural changes are causing the decrease in the DWCNT-ZZ stiffness, the inner and outer wall atomic structures were visualized as a function of the number of sp^3 hybridized bonds. Because of the small diameter, the inner wall of DWCNT-ZZ was significantly altered by the presence of SP^3 defects. While

interstitial carbons do change the structure, it is not nearly as strong a deformation as SP^3 (Figure 5-2). The CNTS analyzed in this study were small diameter. The decrease in wall stiffness with the incorporation of defects is exaggerated by that small diameter. It is expected that the introduction of the same fraction of defects to larger diameter DWCNTs will have less of an effect.[243]

In the case of formation of IC defects by irradiation, generation of vacancies in the walls of irradiated CNTs is expected. Because vacancies cannot directly cause inter-wall load transfer, other than by potentially increasing surface roughness, vacancies were not directly considered in this analysis. Addition of vacancies will decrease Young's modulus due to the increase of non-sp^2 character of the CNT surface.[178] The SP^3 creates less of a vacancy than the IC defect type and the wall will incur less of a decrement to the stiffness. In both cases, the effective Young's modulus will increase due to the presence of inter-wall cross-links while the stiffness of the individual walls decreases due to the degree of vacancy created by each type of defect. It is important to individually quantify each effect, possibly through new CNT descriptors, to develop accurate mathematical models. The effect of vacancies decreases as radius increases, up to approximately 2 nm.[178, 181, 184] Since Young's modulus is independent of chirality[45, 178], it is noted that the increase in effective Young's modulus is greater for DWCNT-ARM (r = 7 Å) than DWCNT-ZZ (r = 5 Å).

Results obtained on the effect of randomly adding hydrogen to the outer wall of the (5,5)@(10,10) DWCNT are as follows. Hydrogen functionalization of the outer wall pulls the carbon atoms away from the inner walls. This is expected to lead to a decrease in inter-wall stress transfer. Further, the outer wall stiffness will suffer a

decrement due to the increase in non-sp^2 character. Calculations show a slight decrease in effective Young's modulus, due to one or both of these effects.
For the descriptor and QSPR development, it was noted that the defect type affects the strain transfer gain. This QSPR will focus on predictions for interstitial carbons but, future work will address developing a scale factor for types of defects as well assigning a weight factor for the number of a particular type that occurs via experimental methods.

A multiple linear regression model (MLR) was built for $S_{\bar{\epsilon}}$. The variables were chiral angle and the ratio of non-sp^2 hybridized carbons to the total number of carbons (C_{N2} / C_T). This descriptor was highly critical in the analysis of Young's modulus earlier in the dissertation. The correlation coefficient was 0.965. Chirality is a factor. Even with diameter increase, it is assumed chirality will be a factor due to the alignment of the armchair and zig-zag bonds to the applied tensile stress.

Table 5-5 : The MLR coefficients for $S_{\bar{\epsilon}}$ illustrate both chiral angle and C_{N2} / C_T are critical variables.

Variables	Coefficient
Chiral Angle	0.08735
C_{N2} / C_T	0.02188
Intercept	9.48303

An MLR model was built for Young's modulus, trained on the small diameter vacancy and methyl data set used earlier in this dissertation. Coefficients are almost the same for the vacancy only test set with radii < 12 Å but include a third variable,

number of methyl groups per total carbon atoms (M_N / M_T). Coefficients are found in the following table.

Table 5-6 : The MLR coefficients to predict Young's modulus are very similar to the SWCNT coefficients, supporting the hypothesis that results from simpler simulations can be piece-wise added to provide comparable accuracies to larger, more complex simulations.

Variables	Coefficient
Chiral Angle	-188.1
C_{N2} / C_T	-2247.4
M_N / C_T	1740.2
Intercept	932.1

Stiffness is the spring constant and is related to Young's Modulus via the following.

$$Young's\ Modulus = k\frac{L}{A} \tag{55}$$

$$F = (k_{Outer} + k_{Inner}S_{\bar{\epsilon}})\Delta x_{Outer} \tag{56}$$

With these two MLR equations and equation (49), enough information is available to find a balance point between decrement of intrinsic wall properties and improvement of load transfer.

5.4 Conclusion

The MD quasi-static simulations show the effect of randomly located inter-wall cross-links on inter-wall strain transfer and modulus for 100 Å long, small diameter DWCNTs. Of the two types of cross-links investigated, direct cross-links (SP^3

defects) and cross-links via interstitial carbon atoms (IC defects), the SP^3 defects provide the highest enhancement of inter-wall strain transfer and the highest enhancement of Young's modulus by associated force transfer (except at the highest observed defect concentration, where the Young's modulus is insensitive to defect type). Discontinuities in plots of inner wall strain versus outer wall strain are due to the energetic capability of the IC defects to relieve strain on the inner wall by shifting bonding site, which apparently does not occur for the SP^3 defects, where there are no discontinuities in the linear relationship between applied outer wall strain and resulting inner wall strain up to the maximum applied outer wall strain of 10%. Additional details are as follows. Transfer of a strain on the external DWCNT wall to the inner wall is close to complete for 100 SP^3 defects on a 100 Å long DWCNTs containing 1800–2500 total carbons and still large, but reduced, when the defect concentration is halved. The transfer of outer wall strain to inner wall strain is sharply decreased (by an amount that depends on defect concentration) when SP^3 cross-linking defects are replaced by the same number of IC defects. Similar results were obtained for (4,0)@(13,0) and (5,5)@(10,10) DWCNTs containing the same type and concentration cross-linking defect, though stress transfer from outer to inner wall was greatest for the former DWCNT (Figure 5-4).

A maximum effective Young's modulus increase (of about 25%) on defect incorporation was achieved for incorporation of either SP^3 defects or IC defects in (5,5)@(10,10) DWCNTs. However, the maximum observed effective Young's modulus had similar values for both nanotubes and both defect types. Computationally observed degradation of wall stretching force constants due to wall structure limits the

increase of effective Young's modulus due to inter-wall cross-links. For the investigated DWCNT having the smaller initial inner wall diameter (4,0)@(13,0) DWCNT, effective Young's modulus reached a maximum, at about 25 SP^3 defects per 100 Å tube length, and then sharply decreased for higher defect concentrations, while for the IC defect in the (4,0)@(13,0) DWCNT or either defect in the (5,5)@(10,10) DWCNT, the maximum effective Young's modulus was for the highest defect concentration. This result suggests that degradation of wall stiffness is largest for SP^3 defects in the (4,0)@(13,0) DWCNT, which is reasonable considering the small inner wall diameter.

Although the formation and meta-stability of sp^3 bonded carbons in graphite by femtosecond laser excitation[240], the stability of the SP^3 defects presented by AIREBO potential should be further investigated. Since Frenkel pair defects also are formed by sp^3 bonds, the SP^3 results at low temperatures and strains would be similar if the cross-linking type is the Frenkel pair. *Ab initio* and DFT calculations are going to be employed in future investigations of the stability of these defects in different carbon nanotubes.

Figure 5-4 shows the inner wall strain nearly follows the strain applied to the outer wall for SP^3 defect types. Therefore, it is expected that when the outer wall strain reaches its failure strain value, the inner wall strain will be also close to its failure strain value. In the case of an external strain causing the breaking of the outer wall, the inner walls linked to the outer one by sp^3 bonds would also break. This was experimentally observed by Peng.[55] They showed that the number of broken most-external walls of MWCNTs subjected to large tensile strains was just 1 for the non-irradiated MWCNTs (so without any cross-link) and more than 1 for all electron irradiated MWCNTs. This

indicates that load transfer is very efficient for defect induced MWCNTs as predicted by our simulations.

Less extensive studies were conducted on the effect of outer wall functionalization by random hydrogen substitution on inter-wall strain transfer. These results are for (5,5)@(10,10) DWCNT, a maximum number of hydrogen substitutions of 100 for the 100 Å long DWCNT, and a maximum strain of 1%. It was found that this hydrogen substitution slightly decreases DWCNT effective Young's modulus.

CHAPTER 6

SUMMARY

This dissertation studied the potential to use a combined physics-based molecular dynamics (MD) and informatics approach to navigate the large problem space for carbon nanotube (CNT) reinforced materials consistent with experimental data. Carbon nanotubes (CNT) have unparalleled mechanical properties, spanning several orders of magnitude over both length and time scales. Results from computational and experimental methods vary greatly. In chapter 3, descriptors and quantitative structure property relationships (QSPRs) were used to study CNT mechanical properties for CNTs with surface vacancies and surface functional groups. Two descriptors were identified as critical, the density of non-sp^2 hybridized carbons and the density of methyl groups functionalizing the surface. There are two important observations. First, QSPR can be developed for CNT mechanical properties relative to surface defects with a limited number of descriptors, reducing the complexity of the problem facilitating navigation of a larger problem space. Second, both of these descriptors can be experimentally measured, paving the way for closed-loop computational-experimental development. For example, rather than refining an empirical potential for more accurate comparison to experimental data, the QSPR can be refined directly through the descriptor. Chapter 4 illustrates that informatics can facilitate discovery of hidden knowledge. Further evaluation of the critical descriptors selected for Poisson's ratio lead to the discovery that Poisson's ratio has strain-varying nonlinear elastic behavior. The goal of chapter 5 was to illustrate the power of piece-wise QSPRs to model a more complex system. First, QSPRs were developed to model the changes to intrinsic wall

stiffness with surface defects for single-walled CNTs. Second, QSPRs were developed to model the changes in strain gain transfer with inter-wall bonding in double-walled CNTs (DWCNTs). The two sets of QSPRs were combined to capture the decrement in both walls' elastic moduli simultaneously with the improvement to inter-wall load transfer. This illustrates that results from simpler systems can used in a piece-wise fashion to model more complex systems, reducing the need for more time-consuming complex system analyses.

REFERENCES

1. Endo, M.; Strano, M. S.; Ajayan, P. M., Potential applications of carbon nanotubes. In *Carbon Nanotubes*, Springer-Verlag Berlin: Berlin, 2008; Vol. 111, pp 13 - 61.

2. Coleman, J. N.; Khan, U.; Blau, W. J.; Gun'ko, Y. K., Small but strong: A review of the mechanical properties of carbon nanotube-polymer composites. *Carbon* **2006,** *44* (9), 1624-1652.

3. Che, J. W.; Cagin, T.; Goddard, W. A. In *Thermal conductivity of carbon nanotubes*, 2000; pp 65-69.

4. Committee on Integrated Computational Materials Engineering, N. R. C., *Integrated Computational Materials Engineering: A Transformational Discipline for Improved Competitiveness and National Security*. National Academy Press: Arlington, Va, 2008; p 152.

5. Schafrik, R.; Christodoulou, L.; Williams, J. C., Collaboration is an essential part of materials development. *Journal of the Minerals, Metals and Materials Society* **2005,** *57* (3), 14-16.

6. Rajan, K., Informatics and Integrated Computational Materials Engineering: Part II. *Journal of the Minerals, Metals and Materials Society* **2009,** *61* (1), 47-47.

7. Ouzounis, C. A.; Valencia, A., Early bioinformatics: the birth of a discipline - a personal view. *Bioinformatics* **2003,** *19* (17), 2176-2190.

8. Rodgers, J. In *Materials Informatics 1999 Conference Documentation*, Materials Informatics, Boston, Ma, June 1, 1999; Rodgers, J., Ed. Knowledge Press: Boston, Ma, 1999.

9. Backman, D. G.; Wei, D. Y.; Whitis, D. D.; Buczek, M. B.; Finnigan, P. M.; Gao, D. M., ICME at GE: Accelerating the insertion of new materials and processes. *Journal of the Minerals, Metals and Materials Society* **2006,** *58* (11), 36-41.

10. Calister Jr, W., *Materials science and engineering: an introduction*. 7th ed.; John Wiley & Sons: United States, 2007.

11. Olson, G. B., Designing a new material world. *Science* **2000,** *288* (5468), 993-998.

12. Allison, J.; Backman, D.; Christodoulou, L., Integrated computational materials engineering: A new paradigm for the global materials profession. *Journal of the Minerals, Metals and Materials Society* **2006,** *58* (11), 25-27.

13. Yao, S.; Wei, F.; Yan, X.-T.; Ion, W. J.; Eynard, B., Research on the Optimization Model of Aircraft Structure Design for Cost Global Design to Gain a Competitive Edge. Springer London: 2008; pp 167-176.

14. Ajayan, P. M.; Schadler, L. S.; Giannaris, C.; Rubio, A., Single-Walled Carbon Nanotube–Polymer Composites: Strength and Weakness. *Advanced Materials* **2000,** *12* (10), 750-753.

15. Byrne, E. M.; McCarthy, M. A.; Xia, Z.; Curtin, W. A., Multiwall Nanotubes Can Be Stronger than Single Wall Nanotubes and Implications for Nanocomposite Design. *Physical Review Letters* **2009,** *103* (4).

16. Veedu, V. P.; Cao, A.; Li, X.; Ma, K.; Soldano, C.; Kar, S.; Ajayan, P. M.; Ghasemi-Nejhad, M. N., Multifunctional composites using reinforced laminae with carbon-nanotube forests. *Nat Mater* **2006,** *5* (6), 457-462.

17. Putz, K. W.; Palmeri, M. J.; Cohn, R. B.; Andrews, R.; Brinson, L. C., Effect of cross-link density on interphase creation in polymer nanocomposites. *Macromolecules* **2008,** *41* (18), 6752-6756.

18. Brenner, D. W.; Shenderova, O. A.; Harrison, J. A.; Stuart, S. J.; Ni, B.; Sinnott, S. B., A second-generation reactive empirical bond order (REBO) potential energy expression for hydrocarbons. *Journal of Physics-Condensed Matter* **2002,** *14* (4), 783-802.

19. Mielke, S. L.; Troya, D.; Zhang, S.; Li, J. L.; Xiao, S. P.; Car, R.; Ruoff, R. S.; Schatz, G. C.; Belytschko, T., The role of vacancy defects and holes in the fracture of carbon nanotubes. *Chemical Physics Letters* **2004,** *390* (4-6), 413-420.

20. Shenderova, O. A.; Brenner, D. W.; Omeltchenko, A.; Su, X.; Yang, L. H., Atomistic modeling of the fracture of polycrystalline diamond. *Physical Review B* **2000,** *61* (6), 3877-3888.

21. Srivastava, D.; Makeev, M. A.; Menon, M.; Osman, M., Computational Nanomechanics and Thermal Transport in Nanotubes and Nanowires. *Journal of Nanoscience and Nanotechnology* **2008,** *8* (7), 3628-3651.

22. Klimeck, G.; McLennan, M.; Brophy, S. B.; Adams, G. B.; Lundstrom, M. S., nanoHUB.org: Advancing education and research in nanotechnology. *Computing in Science & Engineering* **2008,** *10* (5), 17-23.

23. Donley, M. *United States Air Force Unmanned Aircraft Systems Flight Plan 2009-2047*; Washington, D.C., May 18, 2009, 2009.

24. Lorell, M.; Levaux, H., *The cutting edge: a half century of fighter aircraft R&D*. RAND: Santa Monica, Ca, 1998.

25. Sullivan, M. *Defense Acquisitions: Opportunities Exist to Achieve Greater Commonality and Efficiencies among Unmanned Aircraft Systems*; July 30, 2009, 2009.

26. Deo, R.; Starnes, J.; Holzwarth, R., Low-cost composite materials and structures for aircraft applications. In *RTO AVT Specialists' Meeting on "Low Cost Composite Structures"*, Loen, Norway, 2001.

27. Lorell, M., *The U.S. Combat Aircraft Industry, 1909-2000: Structure, Competition, Innovation*. RAND: Santa Monica, Ca, 2003.

28. Younossi, O.; Kennedy, M.; Graser, J., *Military Airframe Costs: The Effects of Advanced Materials and Manufacturing Processes*. Rand: Santa Monica, California, 2001.

29. Strong, B., *Fundamentals of Composites Manufacturing: Materials, Methods and Applications*. 2nd ed.; Society of Manufacturing Engineers: Dearborn, Michigan, 2007.

30. Iijima, S., Helical microtubules of graphitic carbon. *Nature* **1991,** *354* (6348), 56-58.

31. Saito, R.; Dresselhaus, M. S.; Dresselhaus, G., *Physical Properties of Carbon Nanotubes*. Imperial College Press: London, 2007; p 259.

32. Wang, X.; Li, Q.; Xie, J.; Jin, Z.; Wang, J.; Li, Y.; Jiang, K.; Fan, S., Fabrication of Ultralong and Electrically Uniform Single-Walled Carbon Nanotubes on Clean Substrates. *Nano Letters* **2009,** *9* (9), 3137-3141.

33. Baughman, R. H.; Zakhidov, A. A.; de Heer, W. A., Carbon Nanotubes--the Route Toward Applications. *Science* **2002,** *297* (5582), 787-792.

34. Javey, A.; Guo, J.; Wang, Q.; Lundstrom, M.; Dai, H., Ballistic carbon nanotube field-effect transistors. *Nature* **2003,** *424* (6949), 654-657.

35. Kreupl, F.; Graham, A. P.; Duesberg, G. S.; Steinhögl, W.; Liebau, M.; Unger, E.; Hönlein, W., Carbon nanotubes in interconnect applications. *Microelectronic Engineering* **2002,** *64* (1-4), 399-408.

36. Hong, S.; Myung, S., Nanotube Electronics: A flexible approach to mobility. *Nature Nanotechnology* 2007, pp 207-208.

37. Kordas, K.; Toth, G.; Moilanen, P.; Kumpumaki, M.; Vahakangas, J.; Uusimaki, A.; Vajtai, R.; Ajayan, P. M., Chip cooling with integrated carbon nanotube microfin architectures. In *Applied Physics Letters*, American Institute of Physics: 2007; Vol. 90, pp 123105-1.

38. Ge, M.; Sattler, K., Vapor-Condensation generation and STM analysis of fullerene. *Science* **1993,** *260* (5107), 4.

39. Charlier, J. C.; Michenaud, J. P., Energetics of multilayered carbon tubules. *Physical Review Letters* **1993,** *70* (12), 1858.

40. Shan, B.; Cho, K., First-principles study of work functions of double-wall carbon nanotubes. *Physical Review B* **2006,** *73* (8), 081401.

41. Yu, M. F., Fundamental mechanical properties of carbon nanotubes: Current understanding and the related experimental studies. *Journal of Engineering Materials and Technology-Transactions of the Asme* **2004,** *126* (3), 271-278.

42. Agarwal, B. D.; Broutman, L. J.; Chandrashekhara, K., *Analysis and Performance of Fiber Composites*. 3rd ed.; Wiley: 2006; p 560.

43. Callister, W. D., *Materials Science and Engineering, An Introduction*. 7th ed.; John Wiley and Sons: 2007; p 721.

44. Overney, G.; Zhong, W.; Tománek, D., Structural rigidity and low frequency vibrational modes of long carbon tubules. *Zeitschrift für Physik D Atoms, Molecules and Clusters* **1993,** *27* (1), 93-96.

45. Lu, J. P., Elastic Properties of Carbon Nanotubes and Nanoropes. *Physical Review Letters* **1997,** *79* (7), 1297.

46. Sánchez-Portal, D.; Artacho, E.; Soler, J. M.; Rubio, A.; Ordejón, P., Ab initio structural, elastic, and vibrational properties of carbon nanotubes. *Physical Review B* **1999,** *59* (19), 12678.

47. Vodenitcharova, T.; Zhang, L. C., Effective wall thickness of a single-walled carbon nanotube. *Physical Review B* **2003,** *68* (16), 165401.

48. Mylvaganam, K.; Zhang, L. C., Important issues in a molecular dynamics simulation for characterising the mechanical properties of carbon nanotubes. *Carbon* **2004,** *42* (10), 2025-2032.

49. Odegard, G. M.; Gates, T. S.; Nicholson, L. M.; Wise, K. E., Equivalent-continuum modeling of nano-structured materials. *Composites Science and Technology* **2002,** *62* (14), 1869-1880.

50. Zhou, G.; Duan, W.; Gu, B., First-principles study on morphology and mechanical properties of single-walled carbon nanotube. *Chemical Physics Letters* **2001,** *333* (5), 344-349.

51. Yu, M.-F.; Lourie, O.; Dyer, M. J.; Moloni, K.; Kelly, T. F.; Ruoff, R. S., Strength and Breaking Mechanism of Multiwalled Carbon Nanotubes Under Tensile Load. *Science* **2000,** *287* (5453), 637-640.

52. Hernandez, E.; Goze, C.; Bernier, P.; Rubio, A., Elastic properties of single-wall nanotubes. *Applied Physics A: Materials Science & Processing* **1999,** *68* (3), 287-292.

53. Krishnan, A.; Dujardin, E.; Ebbesen, T. W.; Yianilos, P. N.; Treacy, M. M. J., Young's modulus of single-walled nanotubes. *Physical Review B* **1998,** *58* (20), 14013.

54. Treacy, M. M. J.; Ebbesen, T. W.; Gibson, J. M., Exceptionally high Young's modulus observed for individual carbon nanotubes. *Nature* **1996,** *381* (6584), 678-680.

55. Peng, B.; Locascio, M.; Zapol, P.; Li, S.; Mielke, S. L.; Schatz, G. C.; Espinosa, H. D., Measurements of near-ultimate strength for multiwalled carbon nanotubes and irradiation-induced crosslinking improvements. *Nat Nano* **2008,** *3* (10), 626-631.

56. Borders, T. L.; Fonseca, A.; Zhang, H.; Cho, K.; Rusinko, A., Developing Descriptors to Predict Mechanical Properties of Nanotubes. *Journal of Chemical Information and Computer Sciences* **submitted**.

57. Fonseca, A. F.; Borders, T.; Baughman, R. H.; Cho, K., Load transfer between cross-linked walls of a carbon nanotube. *Physical Review B* **2010,** *81* (4), 045429.

58. Stach, E., Nanomaterials: Nanotubes reveal their true strength. *Nat Nano* **2008,** *3* (10), 586-587.

59. Yakobson, B. I.; Campbell, M. P.; Brabec, C. J.; Bernholc, J., High strain rate fracture and C-chain unraveling in carbon nanotubes. *Computational Materials Science* **1997,** *8* (4), 341-348.

60. Wei, C. Y.; Cho, K. J.; Srivastava, D., Tensile strength of carbon nanotubes under realistic temperature and strain rate. *Physical Review B* **2003,** *67* (11).

61. Wei, C. Y.; Cho, K.; Srivastava, D., Tensile yielding of multiwall carbon nanotubes. *Applied Physics Letters* **2003,** *82* (15), 2512-2514.

62. Belytschko, T.; Xiao, S. P.; Schatz, G. C.; Ruoff, R. S., Atomistic simulations of nanotube fracture. *Physical Review B* **2002,** *65* (23).

63. Samsonidze, G. G.; Samsonidze, G. G.; Yakobson, B. I., Kinetic Theory of Symmetry-Dependent Strength in Carbon Nanotubes. *Physical Review Letters* **2002,** *88* (6), 065501.

64. Zhang, P.; Lammert, P. E.; Crespi, V. H., Plastic Deformations of Carbon Nanotubes. *Physical Review Letters* **1998,** *81* (24), 5346.

65. Zhang, S. L.; Mielke, S. L.; Khare, R.; Troya, D.; Ruoff, R. S.; Schatz, G. C.; Belytschko, T., Mechanics of defects in carbon nanotubes: Atomistic and multiscale simulations. *Physical Review B* **2005,** *71* (11).

66. Yu, M.-F.; Files, B. S.; Arepalli, S.; Ruoff, R. S., Tensile Loading of Ropes of Single Wall Carbon Nanotubes and their Mechanical Properties. *Physical Review Letters* **2000,** *84* (24), 5552.

67. Srivastava, D.; Wei, C.; Cho, K., Nanomechanics of carbon nanotubes and composites. *Applied Mechanics Reviews* **2003,** *56* (2), 215-230.

68. Schadler, L. S.; Giannaris, S. C.; Ajayan, P. M., Load transfer in carbon nanotube epoxy composites. *Applied Physics Letters* **1998,** *73* (26), 3842-3844.

69. Ma, W.; Liu, L.; Zhang, Z.; Yang, R.; Liu, G.; Zhang, T.; An, X.; Yi, X.; Ren, Y.; Niu, Z.; Li, J.; Dong, H.; Zhou, W.; Ajayan, P. M.; Xie, S., High-Strength

Composite Fibers: Realizing True Potential of Carbon Nanotubes in Polymer Matrix through Continuous Reticulate Architecture and Molecular Level Couplings. *Nano Letters* **2009,** *9* (8), 2855-2861.

70. Hull, D.; Clyne, T. W., *An Introduction to Composite Materials*. 2nd ed.; Cambridge University Press: 1996.

71. Qian, D.; Dickey, E. C.; Andrews, R.; Rantell, T., Load transfer and deformation mechanisms in carbon nanotube-polystyrene composites. *Applied Physics Letters* **2000,** *76* (20), 2868-2870.

72. Eitan, A.; Fisher, F. T.; Andrews, R.; Brinson, L. C.; Schadler, L. S., Reinforcement mechanisms in MWCNT-filled polycarbonate. *Composites Science and Technology* **2006,** *66* (9), 1162-1173.

73. Moniruzzaman, M.; Chattopadhyay, J.; Billups, W. E.; Winey, K. I., Tuning the Mechanical Properties of SWNT/Nylon 6,10 Composites with Flexible Spacers at the Interface. *Nano Letters* **2007,** *7* (5), 1178-1185.

74. Frankland, S. J. V.; Caglar, A.; Brenner, D. W.; Griebel, M., Molecular Simulation of the Influence of Chemical Cross-Links on the Shear Strength of Carbon Nanotube-Polymer Interfaces. *Journal of Physical Chemistry B* **2002,** *106* (12), 3046-3048.

75. Thostenson, E. T.; Ren, Z.; Chou, T.-W., Advances in the science and technology of carbon nanotubes and their composites: a review. *Composites Science and Technology* **2001,** *61* (13), 1899-1912.

76. Fiedler, B.; Gojny, F. H.; Wichmann, M. H. G.; Nolte, M. C. M.; Schulte, K., Fundamental aspects of nano-reinforced composites. *Composites Science and Technology* **2006,** *66* (16), 3115-3125.

77. Xie, X.-L.; Mai, Y.-W.; Zhou, X.-P., Dispersion and alignment of carbon nanotubes in polymer matrix: A review. *Materials Science and Engineering: R: Reports* **2005,** *49* (4), 89-112.

78. Hamming, L. M.; Qiao, R.; Messersmith, P. B.; Catherine Brinson, L., Effects of dispersion and interfacial modification on the macroscale properties of TiO2 polymer-matrix nanocomposites. *Composites Science and Technology* **2009,** *69* (11-12), 1880-1886.

79. Kim, J. K.; Mai, Y. W., *Engineered Interfaces in Fiber Reinforced Composites*. 1st ed.; Elsevier: Oxford (UK), 1998; p 401.

80. Duncan, R. K.; Chen, X. G.; Bult, J. B.; Brinson, L. C.; Schadler, L. S., Measurement of the critical aspect ratio and interfacial shear strength in MWNT/polymer composites. *Composites Science and Technology* **2010,** *70* (4), 599-605.

81. Rajan, K., Materials Informatics part I: A diversity of issues. *Journal of the Minerals, Metals and Materials Society* **2008,** *60* (3), 50-50.

82. Gasteiger, J.; Engel, T., *Chemoinformatics*. Wiley-VCH: 2003.

83. Weininger, D., SMILES, a chemical language and information system. 1. Introduction to methodology and encoding rules. *Journal of Chemical Information and Computer Sciences* **1988,** *28* (1), 31-36.

84. Prasanna, M. D.; Vondrasek, J.; Wlodawer, A.; Bhat, T. N., Application of InChI to curate, index, and query 3-D structures. *Proteins: Structure, Function, and Bioinformatics* **2005,** *60* (1), 1-4.

85. Ivanciuc, O., Coding the constitution - graph theory in chemistry. In *Handbook of Chemoinformatics*, Gasteiger, J., Ed. Wiley-VCH: Weinheim, 2003.

86. Dalby, A.; Nourse, J. G.; Hounshell, W. D.; Gushurst, A. K. I.; Grier, D. L.; Leland, B. A.; Laufer, J., Description of several chemical structure file formats used by computer programs developed at Molecular Design Limited. *Journal of Chemical Information and Computer Sciences* **1992,** *32* (3), 244-255.

87. Berman, H. M.; Battistuz, T.; Bhat, T. N.; Bluhm, W. F.; Bourne, P. E.; Burkhardt, K.; Feng, Z.; Gilliland, G. L.; Iype, L.; Jain, S.; Fagan, P.; Marvin, J.; Padilla, D.; Ravichandran, V.; Schneider, B.; Thanki, N.; Weissig, H.; Westbrook, J. D.; Zardecki, C., The Protein Data Bank. *Acta Crystallographica Section D* **2002,** *58* (6 Part 1), 899-907.

88. Rusinko, A.; Sheridan, R.; Nilakantan, R.; Haraki, K.; Bauman, N.; Venkataraghavan, R., Using CONCORD to construct a large database of 3-dimensional coordinates from connection tables. *Journal of Chemical Information and Computer Sciences* **1989,** *29*, 5.

89. Cheeseright, T.; Mackey, M.; Rose, S.; Vinter, A., Molecular Field Extrema as Descriptors of Biological Activity: Definition and Validation. *Journal of Chemical Information and Modeling* **2006,** *46* (2), 665-676.

90. Breneman, C., Atomistic to material system complexity. 2008.

91. Antonietti, M.; Ozin, G. A., Promises and Problems of Mesoscale Materials Chemistry or Why Meso? *Chemistry - A European Journal* **2004,** *10* (1), 28-41.

92. Tetko, I. V.; Gasteiger, J.; Todeschini, R.; Mauri, A.; Livingstone, D.; Ertl, P.; Palyulin, V. A.; Radchenko, E. V.; Zefirov, N. S.; Makarenko, A. S.; Tanchuk, V. Y.; Prokopenko, V. V., Virtual computational chemistry laboratory -- design and description. In *Journal of Computer-Aided Molecular Design*, Springer Science & Business Media B.V.: 2005; Vol. 19, pp 453-463.

93. Riesi, M. Talete SRL, DRAGON. http://www.talete.mi.it/products/dragon_all_about.htm (accessed September 5, 2009).

94. Kier, L. B., A shape index from chemical graphs. *Quantitative Structure-Activity Relationships* **1985,** *4*, 109-116.

95. Randic, M., Characterization of molecular branching. *Journal of the American Chemical Society* **1975,** *97* (23), 6609-6615.

96. Randic, M.; Razinger, M., Molecular Topographic Indices. *Journal of Chemical Information and Computer Sciences* **1995,** *35* (1), 140-147.

97. Robinson, D. D.; Barlow, T. W.; Richards, W. G., Reduced Dimensional Representations of Molecular Structure. *Journal of Chemical Information and Computer Sciences* **1997,** *37* (5), 939-942.

98. Karelson, M.; Lobanov, V. S.; Katritzky, A. R., Quantum-Chemical Descriptors in QSAR/QSPR Studies. *Chemical Reviews* **1996,** *96* (3), 1027-1044.

99. Freedman, D.; PIsani, R.; Purves, R., *Statistics*. 4th ed.; W.W. Norton & Co.: New York, 2007; p 720.

100. Rodgers, J.; Nicewander, W., Thirteen ways to look at the correlation coefficient. *The American Statistician* **1988,** *42* (1), 59-66.

101. Qiao, R.; Catherine Brinson, L., Simulation of interphase percolation and gradients in polymer nanocomposites. *Composites Science and Technology* **2009,** *69* (3-4), 491-499.

102. Johnson, M. A.; Maggiora, G. M., Concepts and Applications of Molecular Similarity. John Wiley and Sons: New York, 1990; p 393.

103. Willett, P.; Barnard, J. M.; Downs, G. M., Chemical Similarity Searching. *Journal of Chemical Information and Computer Sciences* **1998,** *38* (6), 983-996.

104. Ginn, C.; Willett, P.; Bradshaw, J., Combination of molecular similarity measures using data fusion. 2001; pp 1-16.

105. Jain, A. K.; Murty, M. N.; Flynn, P. J., Data clustering: a review. *ACM Comput. Surv.* **1999,** *31* (3), 264-323.

106. Downs, G. M.; Barnard, J. M., *Reviews in Computational Chemistry*. Wiley-VCH: New York, 2002; Vol. 18, p 350.

107. Hartigan, J. A.; Wong, M. A., Algorithm AS 136: A K-Means Clustering Algorithm. *Journal of the Royal Statistical Society. Series C (Applied Statistics)* **1979,** *28* (1), 100-108.

108. Ward, J. H., Jr., Hierarchical Grouping to Optimize an Objective Function. *Journal of the American Statistical Association* **1963,** *58* (301), 236-244.

109. Jarvis, R. A.; Patrick, E. A., Clustering using a similarity measure based on shared near neighbors. *IEEE Transactions in Computers* **1973,** *C-22*, 1025-1034.

110. Downs, G. M.; Willett, P.; Fisanick, W., Similarity Searching and Clustering of Chemical-Structure Databases Using Molecular Property Data. *Journal of Chemical Information and Computer Sciences* **1994,** *34* (5), 1094-1102.

111. Brown, R. D.; Martin, Y. C., Use of Structure−Activity Data To Compare Structure-Based Clustering Methods and Descriptors for Use in Compound Selection. *Journal of Chemical Information and Computer Sciences* **1996,** *36* (3), 572-584.

112. Leach, A.; Gillet, V., *An Introduction to Chemoinformatics*. Revised ed.; Springer: Dordrecht, The Netherlands, 2007.

113. Guyon, I.; Elisseeff, A., An introduction to variable and feature selection. *J. Mach. Learn. Res.* **2003,** *3*, 1157-1182.

114. Friedman, J. H., Multivariate Adaptive Regression Splines. *The Annals of Statistics* **1991,** *19* (1), 1-67.

115. Swierenga, H.; de Groot, P. J.; de Weijer, A. P.; Derksen, M. W. J.; Buydens, L. M. C., Improvement of PLS model transferability by robust wavelength selection. *Chemometrics and Intelligent Laboratory Systems* **1998,** *41* (2), 237-248.

116. Wold, S.; Sjöström, M.; Eriksson, L., PLS-regression: a basic tool of chemometrics. *Chemometrics and Intelligent Laboratory Systems* **2001,** *58* (2), 109-130.

117. Abdi, H.; Williams, L. J., Principal component analysis. *Wiley Interdisciplinary Reviews: Computational Statistics* **2010,** *2* (4), 433-459.

118. Cattell, R. B., The Scree Test For The Number Of Factors. *Multivariate Behavioral Research* **1966,** *1* (2), 245-276.

119. Izenman, A., *Modern Multivariate Statistical Techniques*. 1st ed.; Springer: 2008; p 731.

120. George, L.; Hrubiak, R.; Rajan, K.; Saxena, S. K., Principal component analysis on properties of binary and ternary hydrides and a comparison of metal versus metal hydride properties. *Journal of Alloys and Compounds* **2009,** *478* (1-2), 731-735.

121. Mitchell, M., *An introduction to genetic algorithms*. MIT Press: Cambridge, Massachusetts, 1998; p 186.

122. Xu, L.; Zhang, W.-J., Comparison of different methods for variable selection. *Analytica Chimica Acta* **2001,** *446* (1-2), 475-481.

123. Rogers, D.; Hopfinger, A. J., Application of Genetic Function Approximation to Quantitative Structure-Activity Relationships and Quantitative Structure-Property Relationships. *Journal of Chemical Information and Computer Sciences* **1994,** *34* (4), 854-866.

124. Wiegand, P.; Pell, R.; Comas, E., Simultaneous variable selection and outlier detection using a robust genetic algorithm. *Chemometrics and Intelligent Laboratory Systems* **2009,** *98* (2), 108-114.

125. Geladi, P.; Kowalski, B. R., Partial least-squares regression: a tutorial. *Analytica Chimica Acta* **1986,** *185* (0), 1-17.

126. Bi, J.; Bennett, K.; Embrechts, M.; Breneman, C.; Song, M., Dimensionality reduction via sparse support vector machines. *J. Mach. Learn. Res.* **2003,** *3*, 1229-1243.

127. Draper, N. R.; Smith, H., *Applied Regression Analysis*. 3rd ed.; John Wiley & Sons: New York, 1998.

128. Wold, H., *Soft Modeling, the Basic Design and Some Extensions*. Amsterdam, North Holland, 1982.

129. Tropsha, A.; Gramatica, P.; Gombar, Vijay K., The Importance of Being Earnest: Validation is the Absolute Essential for Successful Application and Interpretation of QSPR Models. *QSAR & Combinatorial Science* **2003,** *22* (1), 69-77.

130. Golbraikh, A.; Tropsha, A., Beware of q2! *Journal of Molecular Graphics and Modelling* **2002,** *20* (4), 269-276.

131. Gramatica, P., Principles of QSAR models validation: internal and external. *QSAR & Combinatorial Science* **2007,** *26* (5), 694-701.

132. Wehrens, R.; Putter, H.; Buydens, L. M. C., The bootstrap: a tutorial. *Chemometrics and Intelligent Laboratory Systems* **2000,** *54*, 35-52.

133. Katz, A. H., *Chemometric Methods in Molecular Design (Methods and Principles in Medicinal Chemistry)* Wiley-VCH: 1996; p 359.

134. Netzeva, T.; Worth, A.; Aldenberg, T.; Benigni, R.; Cronin, M.; Gramatica, P.; Jaworska, J.; Kahn, S.; Klopman, G.; Marchant, C.; Myatt, G.; Nikolova-Jeliazkova, N.; Patlewicz, G.; Perkins, D.; Roberts, D.; Schultz, T.; Stanton, D.; van de Sandt, J.; Tong, W.; Veith, G.; Yang, C., Current Status of Methods for Defining the Applicability Domain of (Quantitative) Structure–Activity Relationships. *ATLA* **2005,** *33*, 1-19.

135. Eriksson, L.; Jaworska, J.; Worth, A. P.; Cronin, M. T. D.; McDowell, R. M.; Gramatica, P., Methods for Reliability and Uncertainty Assessment and for Applicability Evaluations of Classification- and Regression-Based QSARs. *Environmental Health Perspectives* **2003,** *111* (10), 1361-1375.

136. Allen, M. P.; Tildesley, D. J., *Computer Simulations of Liquids*. Clarendon Press: Oxford, 1987.

137. Friesner, R. A., Ab initio quantum chemistry: Methodology and applications. *Proceedings of the National Academy of Sciences of the United States of America* **2005,** *102* (19), 6648-6653.

138. Brenner, D. W., *The Art and Science of an Analytic Potential*. Wiley-VCH Verlag GmbH & Co. KGaA: 2005; p 23-40.

139. Leach, A., *Molecular Modelling, Principles and Applications*. 2nd ed.; Pearson Education Limited: Essex, England, 2001; p 744.

140. Allen, M. P.; Tildesley, D. J., *Computer Simulations of Liquids*. Oxford University Press: New York, 1987; p 385.

141. Verlet, L., Computer "Experiments" on Classical Fluids. I. Thermodynamical Properties of Lennard-Jones Molecules. *Physical Review* **1967,** *159* (1), 98.

142. Swope, W. C.; Andersen, H. C.; Berens, P. H.; Wilson, K. R., A computer simulation method for the calculation of equilibrium constants for the formation of physical clusters of molecules: Application to small water clusters. *The Journal of Chemical Physics* **1982,** *76* (1), 637-649.

143. Abell, G. C., Empirical chemical pseudopotential theory of molecular and metallic bonding. *Physical Review B* **1985,** *31* (10), 6184.

144. Tersoff, J., Empirical Interatomic Potential for Carbon, with Applications to Amorphous Carbon. *Physical Review Letters* **1988,** *61* (25), 2879.

145. Brenner, D. W., Empirical potential for hydrocarbons for use in simulating the chemical vapor deposition of diamond films. *Physical Review B* **1990,** *42* (15), 9458.

146. Stuart, S. J.; Tutein, A. B.; Harrison, J. A., A reactive potential for hydrocarbons with intermolecular interactions. *Journal of Chemical Physics* **2000,** *112* (14), 6472-6486.

147. Liu, A.; Stuart, S. J., Empirical bond-order potential for hydrocarbons: Adaptive treatment of van der Waals interactions. *Journal of Computational Chemistry* **2008,** *29* (4), 601-611.

148. Hünenberger, P. H., Thermostat Algorithms for Molecular Dynamics Simulations. In *Advanced Computer Simulation*, Springer Berlin / Heidelberg: 2005; Vol. 173, pp 130-130.

149. Berendsen, H. J. C.; Postma, J. P. M.; van Gunsteren, W. F.; DiNola, A.; Haak, J. R., Molecular dynamics with coupling to an external bath. *The Journal of Chemical Physics* **1984,** *81* (8), 3684-3690.

150. Hockney, R. W., Potential calculation and some applications. *Methods Comput. Phys.* **1970**.

151. Ogata, S.; Shibutani, Y., Ideal tensile strength and band gap of single-walled carbon nanotubes. *Physical Review B* **2003,** *68* (16), 165409.

152. Chou, T.-W.; Gao, L.; Thostenson, E. T.; Zhang, Z.; Byun, J.-H., An assessment of the science and technology of carbon nanotube-based fibers and composites. *Composites Science and Technology* **2010,** *70* (1), 1-19.

153. Breuer, O.; Sundararaj, U., Big returns from small fibers: A review of polymer/carbon nanotube composites. *Polymer Composites* **2004,** *25* (6), 630-645.

154. Thostenson, E. T.; Li, C.; Chou, T.-W., Nanocomposites in context. *Composites Science and Technology* **2005,** *65* (3-4), 491-516.

155. Hashimoto, A.; Suenaga, K.; Gloter, A.; Urita, K.; Iijima, S., Direct evidence for atomic defects in graphene layers. *Nature* **2004,** *430* (7002), 870-873.

156. Spitalsky, Z.; Tasis, D.; Papagelis, K.; Galiotis, C., Carbon nanotube-polymer composites: Chemistry, processing, mechanical and electrical properties. *Progress in Polymer Science* **2010,** *35* (3), 357-401.

157. Zhu, J.; Peng, H.; Rodriguez-Macias, F.; Margrave, J. L.; Khabashesku, V. N.; Imam, A. M.; Lozano, K.; Barrera, E. V., Reinforcing Epoxy Polymer Composites Through Covalent Integration of Functionalized Nanotubes. *Advanced Functional Materials* **2004,** *14* (7), 643-648.

158. Lin, Y.; Meziani, M. J.; Sun, P., Functionalized carbon nanotubes for polymeric nanocomposites. *Journal of Materials Chemistry* **2007,** *17* (12), 1143-1148.

159. Barber, A. H.; Cohen, S. R.; Wagner, H. D., Measurement of carbon nanotube polymer interfacial strength. In *Applied Physics Letters*, American Institute of Physics: 2003; Vol. 82, p 4140.

160. Coleman, J. N.; Cadek, M.; Blake, R.; Nicolosi, V.; Ryan, K. P.; Belton, C.; Fonseca, A.; Nagy, J. B.; Gun'ko, Y. K.; Blau, W. J., High Performance Nanotube-Reinforced Plastics: Understanding the Mechanism of Strength Increase. *Advanced Functional Materials* **2004,** *14* (8), 791-798.

161. Todeschini, R.; Consonni, V., *Handbook of Molecular Descriptors*. WILEY - VCH: 2000; Vol. 11.

162. Lipinski, C. A.; Lombardo, F.; Dominy, B. W.; Feeney, P. J., Experimental and computational approaches to estimate solubility and permeability in drug discovery and development settings. *Advanced Drug Delivery Reviews* **1997,** *23* (1-3), 3-25.

163. Rajan, K., Materials informatics. *Materials Today* **2005,** *8* (10), 38-45.

164. Jancar, J.; Douglas, J. F.; Starr, F. W.; Kumar, S. K.; Cassagnau, P.; Lesser, A. J.; Sternstein, S. S.; Buehler, M. J., Current issues in research on structure-property relationships in polymer nanocomposites. *Polymer 51* (15), 3321-3343.

165. Ossi, L.; et al., Characterization of ion-irradiation-induced defects in multi-walled carbon nanotubes. *New Journal of Physics* **2011,** *13* (7), 073004.

166. Dresselhaus, M. S.; Jorio, A.; Souza FIlho, A. G.; Saito, R., Visualizing Individual Nitrogen Dopants in Monolayer Graphene. *Science* **2011,** *333* (6045), 999-1003.

167. Suzuki, S.; Hibino, H., Characterization of doped single-wall carbon nanotubes by Raman spectroscopy. *Carbon* **2011,** *49* (7), 2264-2272.

168. Krishnamoorti, R.; Vaia, R. A., Polymer nanocomposites. *Journal of Polymer Science Part B: Polymer Physics* **2007,** *45* (24), 3252-3256.

169. Huang, C. Data fusion in scientific data mining. Ph.D. dissertation, Rensselaer Polytechnic Institute, Troy, New York, 2009.

170. Chambers, J. M.; Cleveland, W. S.; Kleiner, B.; Turkey, P. A., *Graphical Methods for Data Analysis*. Wadsworth: Belmont, Ca, 1983.

171. Ozaki, T.; Iwasa, Y.; Mitani, T., Stiffness of Single-Walled Carbon Nanotubes under Large Strain. *Physical Review Letters* **2000,** *84* (8), 1712.

172. Ni, B.; Sinnott, S. B.; Mikulski, P. T.; Harrison, J. A., Compression of Carbon Nanotubes Filled with C60, CH4, or Ne: Predictions from Molecular Dynamics Simulations. *Physical Review Letters* **2002,** *88* (20), 205505.

173. Zhou, L. G.; Shi, S. Q., Molecular dynamic simulations on tensile mechanical properties of single-walled carbon nanotubes with and without hydrogen storage. *Computational Materials Science* **2002,** *23* (1-4), 166-174.

174. Dereli, G.; Ozdogan, C., Structural stability and energetics of single-walled carbon nanotubes under uniaxial strain. *Physical Review B* **2003,** *67* (3).

175. Tunvir, K.; Nahm, S. H.; Kim, A.; Lee, H. J., Mechanical properties of carbon nanotubes with randomly distributed vacancy defects. *Journal of the Korean Physical Society* **2007,** *51* (6), 1940-1947.

176. Haskins, R. W.; Maier, R. S.; Ebeling, R. M.; Marsh, C. P.; Majure, D. L.; Bednar, A. J.; Welch, C. R.; Barker, B. C.; Wu, D. T., Tight-binding molecular dynamics study of the role of defects on carbon nanotube moduli and failure. *Journal of Chemical Physics* **2007,** *127* (7).

177. Jeng, Y. R.; Tsai, P. C.; Fang, T. H., Effects of temperature and vacancy defects on tensile deformation of single-walled carbon nanotubes. *Journal of Physics and Chemistry of Solids* **2004,** *65* (11), 1849-1856.

178. Sammalkorpi, M.; Krasheninnikov, A.; Kuronen, A.; Nordlund, K.; Kaski, K., Mechanical properties of carbon nanotubes with vacancies and related defects. *Physical Review B* **2004,** *70* (24).

179. Yakobson, B. I.; Brabec, C. J.; Bernholc, J., Nanomechanics of Carbon Tubes: Instabilities beyond Linear Response. *Physical Review Letters* **1996,** *76* (14), 2511.

180. Gupta, S.; Dharamvir, K.; Jindal, V. K., Elastic moduli of single-walled carbon nanotubes and their ropes. *Physical Review B* **2005,** *72* (16), 165428.

181. Popov, V. N.; Van Doren, V. E.; Balkanski, M., Elastic properties of single-walled carbon nanotubes. *Physical Review B* **2000,** *61* (4), 3078.

182. Dereli, G.; Sangu, B., Temperature dependence of the tensile properties of single-walled carbon nanotubes: O(N) tight-binding molecular-dynamics simulations. *Physical Review B* **2007,** *75* (18), 184104.

183. Sun, X.; Zhao, W., Prediction of stiffness and strength of single-walled carbon nanotubes by molecular-mechanics based finite element approach. *Materials Science and Engineering: A* **2005,** *390* (1-2), 366-371.

184. Chang, T.; Gao, H., Size-dependent elastic properties of a single-walled carbon nanotube via a molecular mechanics model. *Journal of the Mechanics and Physics of Solids* **2003,** *51* (6), 1059-1074.

185. Tienchong, C.; Jingyan, G.; Xingming, G., Chirality- and size-dependent elastic properties of single-walled carbon nanotubes. In *Applied Physics Letters*, American Institute of Physics: 2005; Vol. 87, p 251929.

186. Lau, K.-T.; Chipara, M.; Ling, H.-Y.; Hui, D., On the effective elastic moduli of carbon nanotubes for nanocomposite structures. *Composites Part B: Engineering* **2004,** *35* (2), 95-101.

187. Zhao, P.; Shi, G., Study of Poisson Ratios of Single-Walled Carbon Nanotubes based on an Improved Molecular Structural Mechanics Model. *CMC: Computers, Materials & Continua* **2011,** *22* (2), 147-168.

188. Mori, H.; Hirai, Y.; Ogata, S.; Akita, S.; Nakayama, Y., Chirality Dependence of Mechanical Properties of Single-Walled Carbon Nanotubes under Axial Tensile Strain. *Japanese Journal of Applied Physics* **2005,** *44* (42), 1307-1309.

189. Jiang, H.; Zhang, P.; Liu, B.; Huang, Y.; Geubelle, P. H.; Gao, H.; Hwang, K. C., The effect of nanotube radius on the constitutive model for carbon nanotubes. *Computational Materials Science* **2003,** *28* (3-4), 429-442.

190. Gao, M.; Zuo, J. M.; Twesten, R. D.; Petrov, I.; Nagahara, L. A.; Zhang, R., Structure determination of individual single-wall carbon nanotubes by nanoarea electron diffraction *Applied Physics Letters* **2003,** *82* (16), 2703-2705.

191. Deniz, H.; Derbakova, A.; Qin, L.-C., A systematic procedure for determining the chiral indices of multi-walled carbon nanotubes using electron diffraction - each and every shell. *Ultramicroscopy* **2010,** *111* (1), 66-72.

192. Odom, T. W.; Huang, J.-L.; Kim, P.; Lieber, C. M., Atomic structure and electronic properties of single-walled carbon nanotubes. *Nature* **1998,** *391* (6662), 62-64.

193. Kuang, Y. D.; He, X. Q., Young's moduli of functionalized single-wall carbon nanotubes under tensile loading. *Composites Science and Technology* **2009,** *69* (2), 169-175.

194. Namilae, S.; Chandra, N.; Shet, C., Mechanical behavior of functionalized nanotubes. *Chemical Physics Letters* **2004,** *387* (4-6), 247-252.

195. Coto, B.; Antia, I.; Blanco, M.; Martinez-de-Arenaza, I.; Meaurio, E.; Barriga, J.; Sarasua, J.-R., Molecular dynamics study of the influence of functionalization on the elastic properties of single and multiwall carbon nanotubes. *Computational Materials Science* **2010,** *50* (12), 3417-3424.

196. Garg, A.; Sinnott, S. B., Effect of chemical functionalization on the mechanical properties of carbon nanotubes. *Chemical Physics Letters* **1998,** *295* (4), 273-278.

197. Zhang, Z. Q.; et al., Mechanical properties of functionalized carbon nanotubes. *Nanotechnology* **2008,** *19* (39), 395702.

198. Wang, S., Optimum degree of functionalization for carbon nanotubes. *Current Applied Physics* **2009,** *9* (5), 1146-1150.

199. Scarpa, F.; Adhikari, S.; Wang, C. Y., Mechanical properties of non-reconstructed defective single-wall carbon nanotubes. *J. Phys. D-Appl. Phys.* **2009,** *42* (14), 6.

200. Shen, L.; Li, J., Transversely isotropic elastic properties of single-walled carbon nanotubes. *Physical Review B* **2004,** *69* (4), 045414.

201. Greaves, G. N.; Greer, A. L.; Lakes, R. S.; Rouxel, T., Poisson's ratio and modern materials. *Nat Mater* **2011,** *10* (11), 823-837.

202. Hao, Y. L.; Li, S. J.; Sun, B. B.; Sui, M. L.; Yang, R., Ductile Titanium Alloy with Low Poisson's Ratio. *Physical Review Letters* **2007,** *98* (21), 216405.

203. Schroers, J.; Johnson, W. L., Ductile Bulk Metallic Glass. *Physical Review Letters* **2004,** *93* (25), 255506.

204. Smith, C. W.; Wootton, R. J.; Evans, K. E., Interpretation of experimental data for Poisson's ratio of highly nonlinear materials *Experimental Mechanics* **1999,** *39* (4), 356-362.

205. Xiao, J. R.; Staniszewski, J.; Gillespie Jr, J. W., Fracture and progressive failure of defective graphene sheets and carbon nanotubes. *Composite Structures* **2009,** *88* (4), 602-609.

206. Walters, D., Elastic strain of freely suspended single-wall carbon nanotube ropes. *Appl. Phys. Lett.* **1999,** *74* (25), 3803.

207. Ding, W.; Calabri, L.; Kohlhaas, K.; Chen, X.; Dikin, D.; Ruoff, R., Modulus, Fracture Strength, and Brittle vs. Plastic Response of the Outer Shell of Arc-grown Multi-walled Carbon Nanotubes. *Experimental Mechanics* **2007,** *47* (1), 25-36.

208. Nardelli, M. B.; Yakobson, B. I.; Bernholc, J., Brittle and ductile behavior in carbon nanotubes. *Physical Review Letters* **1998,** *81* (21), 4656-4659.

209. Jeong, B. W.; Lim, J. K.; Sinnott, S. B., Tensile mechanical behavior of hollow and filled carbon nanotubes under tension or combined tension-torsion. *Applied Physics Letters* **2007,** *90* (2).

210. Li, R.; et al., Numerical distortion and effects of thermostat in molecular dynamics simulations of single-walled carbon nanotubes. *Chinese Physics B* **2008,** *17* (11), 4253.

211. Tully, J. C., Stochastic-trajectory simulations of gas-surface interactions: Xe on Pt(111). *Faraday Discussions of the Chemical Society* **1985,** *80*, 291-298.

212. Borders, T.; Zhang, H.; Fonseca, A.; Cho, K.; Rusinko, A., Strain-Varying Nonlinear Elastic Behavior of Poisson's Ratio in Nanotubes. *Journal of Chemical Physics* **2011,** *To be submitted*.

213. Shepherd, J. F.; Dewey, M. W.; Woodbury, A. C.; Benzley, S. E.; Staten, M. L.; Owen, S. J., Adaptive mesh coarsening for quadrilateral and hexahedral meshes. *Finite Elements in Analysis and Design* **2010,** *46* (1-2), 17-32.

214. Cignoni, P.; Corsini, M.; Ranzuglia, G., MeshLab: an Open-Source

3D Mesh Processing System. *ERCIM NEWS* **2008,** *73*, 47-48.

215. Humphrey, W.; Dalke, A.; Schulten, K., VMD: Visual molecular dynamics. *Journal of Molecular Graphics* **1996,** *14* (1), 33-38.

216. Buongiorno Nardelli, M.; Yakobson, B. I.; Bernholc, J., Mechanism of strain release in carbon nanotubes. *Physical Review B* **1998,** *57* (8), R4277-R4280.

217. Lu, Q.; Bhattacharya, B., Fracture resistance of zigzag single walled carbon nanotubes. *Nanotechnology* **2006,** *17* (5), 1323-1332.

218. Meo, M.; Rossi, M., Tensile failure prediction of single wall carbon nanotube. *Engineering Fracture Mechanics* **2006,** *73* (17), 2589-2599.

219. Benedict, L. X.; Chopra, N. G.; Cohen, M. L.; Zettl, A.; Louie, S. G.; Crespi, V. H., Microscopic determination of the interlayer binding energy in graphite. *Chemical Physics Letters* **1998,** *286* (5-6), 490-496.

220. Shibuta, Y.; Elliott, J. A., Interaction between two graphene sheets with a turbostratic orientational relationship. *Chemical Physics Letters* **2011,** *512* (4-6), 146-150.

221. Jeng, Y.-R.; Tsai, P.-C.; Fang, T.-H., Effects of temperature, strain rate, and vacancies on tensile and fatigue behaviors of silicon-based nanotubes. *Physical Review B* **2005,** *71* (8), 085411.

222. Scarpa, F., Coupled thermomechanics of single-wall carbon nanotubes. *Appl. Phys. Lett. 97* (15), 151903.

223. Scarpa, F., Coupled thermomechanics of single-wall carbon nanotubes. *Appl. Phys. Lett.* **2010,** *97* (15), 151903.

224. Wei, C.; Srivastava, D.; Cho, K., Thermal Expansion and Diffusion Coefficients of Carbon Nanotube-Polymer Composites. *Nano Letters* **2002,** *2* (6), 647-650.

225. Schadler, L.; Brinson, L.; Sawyer, W., Polymer nanocomposites: A small part of the story. *Journal of the Minerals, Metals and Materials Society* **2007,** *59* (3), 53-60.

226. Huhtala, M.; Krasheninnikov, A. V.; Aittoniemi, J.; Stuart, S. J.; Nordlund, K.; Kaski, K., Improved mechanical load transfer between shells of multiwalled carbon nanotubes. *Physical Review B* **2004,** *70* (4).

227. Cumings, J.; Zettl, A., Low-Friction Nanoscale Linear Bearing Realized from Multiwall Carbon Nanotubes. *Science* **2000,** *289* (5479), 602-604.

228. Hong, B. H.; Small, J. P.; Purewal, M. S.; Mullokandov, A.; Sfeir, M. Y.; Wang, F.; Lee, J. Y.; Heinz, T. F.; Brus, L. E.; Kim, P.; Kim, K. S., Extracting subnanometer single shells from ultralong multiwalled carbon nanotubes. *Proceedings of the National Academy of Sciences of the United States of America* **2005,** *102* (40), 14155-14158.

229. Kis, A.; Jensen, K.; Aloni, S.; Mickelson, W.; Zettl, A., Interlayer Forces and Ultralow Sliding Friction in Multiwalled Carbon Nanotubes. *Physical Review Letters* **2006,** *97* (2), 025501.

230. Yu, M.-F.; Yakobson, B. I.; Ruoff, R. S., Controlled Sliding and Pullout of Nested Shells in Individual Multiwalled Carbon Nanotubes. *The Journal of Physical Chemistry B* **2000,** *104* (37), 8764-8767.

231. Florian, B., Irradiation effects in carbon nanostructures. *Reports on Progress in Physics* **1999,** *62* (8), 1181.

232. Urita, K.; Suenaga, K.; Sugai, T.; Shinohara, H.; Iijima, S., In Situ Observation of Thermal Relaxation of Interstitial-Vacancy Pair Defects in a Graphite Gap. *Physical Review Letters* **2005,** *94* (15), 155502.

233. Ni, B.; Andrews, R.; Jacques, D.; Qian, D.; Wijesundara, M. B. J.; Choi, Y.; Hanley, L.; Sinnott, S. B., A Combined Computational and Experimental Study of

Ion-Beam Modification of Carbon Nanotube Bundles. *The Journal of Physical Chemistry B* **2001,** *105* (51), 12719-12725.

234. Seldin, E., Elastic Constants and Electron Microscope Observations of Neutron Irradiated Compression Annealed Pyrolytic and Single Crystal Graphite. *J. Appl. Phys.* **1970,** *41* (8), 3389.

235. Xia, Z.; Curtin, W. A., Pullout forces and friction in multiwall carbon nanotubes. *Physical Review B* **2004,** *69* (23).

236. Xia, Z. H.; Guduru, P. R.; Curtin, W. A., Enhancing mechanical properties of multiwall carbon nanotubes via sp(3) interwall bridging. *Physical Review Letters* **2007,** *98* (24).

237. Telling, R. H.; Ewels, C. P.; El-Barbary, A. A.; Heggie, M. I., Wigner defects bridge the graphite gap. *Nature Materials* **2003,** *2* (5), 333-337.

238. Shen, G. A.; Namilae, S.; Chandra, N., Load transfer issues in the tensile and compressive behavior of multiwall carbon nanotubes. *Materials Science and Engineering: A* **2006,** *429* (1-2), 66-73.

239. Song, H.; Zha, X., Molecular dynamics study of effects of sp3 interwall bridging and initial vacancy-related defects on mechanical properties of double-walled carbon nanotube. *Physica B: Condensed Matter* **2008,** *403* (19-20), 3798-3802.

240. Kanasaki, J.; Inami, E.; Tanimura, K.; Ohnishi, H.; Nasu, K., Formation of sp3-Bonded Carbon Nanostructures by Femtosecond Laser Excitation of Graphite. *Physical Review Letters* **2009,** *102* (8), 087402.

241. Muniz, A. R.; Singh, T.; Aydil, E. S.; Maroudas, D., Analysis of diamond nanocrystal formation from multiwalled carbon nanotubes. *Physical Review B* **2009,** *80* (14), 144105.

242. Park, S.; Srivastava, D.; Cho, K., Generalized Chemical Reactivity of Curved Surfaces: Carbon Nanotubes. *Nano Letters* **2003,** *3* (9), 1273-1277.

243. Parvaneh, V.; Shariati, M., Effect of defects and loading on prediction of Young's modulus of SWCNTs. *Acta Mechanica* **2011,** *216* (1), 281-289.